Line-Intensity Mapping: 2017 Status Report

Ely D. Kovetz, Marco P. Viero, Adam Lidz, Laura Newburgh, Mubdi Rahman, E. Switzer, Marc Kamionkowski, James Aguirre, Marcelo Alvarez, James J. Bock, et al.

Line-Intensity Mapping: 2017 Status Report

E. D. Kovetz[1,*], M. P. Viero[2], A. Lidz[3], L. Newburgh[4], M. Rahman[1], E. Switzer[5], M. Kamionkowski[1], J. Aguirre[3], M. Alvarez[6], J. Bock[7], J. R. Bond[6], G. Bower[8], C. M. Bradford[9], P. C. Breysse[6], P. Bull[9], T. C. Chang[9], Y. T. Cheng[7], D. Chung[2], K. Cleary[7], A. Cooray[10], A. Crites[7], R. Croft[11], O. Doré[7,9], M. Eastwood[7], A. Ferrara[12], J. Fonseca[13], D. Jacobs[14], G. Keating[15], G. Lagache[16], G. Lakhlani[6], A. Liu[17,18], K. Moodley[19], N. Murray[6], A. Penin[19], G. Popping[20], A. Pullen[21], D. Reichers[22], S. Saito[23], B. Saliwanchik[19], M. Santos[13,24], R. Somerville[25,26], G. Stacey[22], G. Stein[6], F. Villaescusa-Navarro[26], E. Visbal[26], A. Weltman[27], L. Wolz[28], M. Zemcov[29]

[1]Department of Physics and Astronomy, Johns Hopkins University, 3400 N. Charles St., Baltimore, MD 21218, USA
[2]Kavli Institute for Particle Astrophysics and Cosmology, Stanford University, 382 Via Pueblo Mall, Stanford, CA 94305
[3]Department of Physics and Astronomy, University of Pennsylvania, 209 South 33rd Street, Philadelphia, PA 19104, USA
[4]Department of Physics, Yale University, New Haven, CT 06520
[5]NASA Goddard Space Flight Center, Greenbelt, MD, USA
[6]Canadian Institute for Theoretical Astrophysics, University of Toronto, 60 St. George st., Toronto, ON, M5S 3H8, Canada
[7]Division of Physics, Math and Astronomy, California Institute of Technology, 1200 E. California Blvd. Pasadena, CA 91125
[8]Academia Sinica Institute of Astronomy and Astrophysics, 645 N. A'ohoku Place, Hilo, HI 96720, USA
[9]Jet Propulsion Laboratory, California Institute of Technology, 4800 Oak Grove Drive, Pasadena, CA 91109, USA
[10]Kavli Institute for Particle Astrophysics and Cosmology, Physics Department, Stanford University, Stanford, CA 94305, USA
[11]McWilliams Center for Cosmology, Department of Physics, Carnegie Mellon University, Pittsburgh, PA 15213, USA
[12]Normale Superiore, Piazza dei Cavalieri 7, 56126 Pisa, Italy
[13]Department of Physics and Astronomy, University of the Western Cape, Cape Town 7535, South Africa
[14]School of Earth and Space Exploration, Arizona State University, 781 E Terrace Mall, Tempe, AZ 85287
[15]Harvard-Smithsonian Center for Astrophysics, 60 Garden Street, Cambridge, MA 02138, USA
[16]Aix Marseille Univ, CNRS, LAM, Laboratoire d'Astrophysique de Marseille, Marseille, France
[17]Department of Astronomy and Radio Astronomy Laboratory, University of California, Berkeley, CA 94720, USA
[18]Department of Physics and McGill Space Institute, McGill University, Montreal, QC H3A 2T8, Canada
[19]Astrophysics and Cosmology Research Unit, University of KwaZulu-Natal, Durban, 4041, South Africa
[20]European Southern Observatory, Karl-Schwarzschild-Strasse 2, 85748, Garching, Germany
[21]Center for Cosmology and Particle Physics, Department of Physics, New York University, New York, NY, 10003, USA
[22]Department of Astronomy, Cornell University, Ithaca, NY 14853, USA
[23]Max-Planck-Institut fuer Astrophysik, Karl-Schwarzschild-Str. 1, 85748, Garching, Germany
[24]SKA South Africa, 3rd Floor, The Park, Park Road, Pinelands, 7405, South Africa
[25]Department of Physics and Astronomy, Rutgers University, USA
[26]Center for Computational Astrophysics, Flatiron Institute, 162 5th Ave, 10010, New York,NY, USA
[27]Department of Mathematics and Applied Mathematics, University of Cape Town, Rondebosch, 7700, South Africa
[28]School of Physics, University of Melbourne, Parkville, VIC 3010, Australia
[29]School of Physics and Astronomy, Rochester Institute of Technology, Rochester, NY 14623, USA

[*]email: ekovetz1@jhu.edu

Abstract

Following the first two annual intensity mapping workshops at Stanford in March 2016 and Johns Hopkins in June 2017, we report on the recent advances in theory, instrumentation and observation that were presented in these meetings and some of the opportunities and challenges that were identified looking forward. With preliminary detections of CO, [CII], Lyα and low-redshift 21cm, and a host of experiments set to go online

in the next few years, the field is rapidly progressing on all fronts, with great anticipation for a flood of new exciting results. This current snapshot provides an efficient reference for experts in related fields and a useful resource for nonspecialists. We begin by introducing the concept of line-intensity mapping and then discuss the broad array of science goals that will be enabled, ranging from the history of star formation, reionization and galaxy evolution to measuring baryon acoustic oscillations at high redshift and constraining theories of dark matter, modified gravity and dark energy. After reviewing the first detections reported to date, we survey the experimental landscape, presenting the parameters and capabilities of relevant instruments such as COMAP, mmIMe, AIM-CO, CCAT-p, TIME, CONCERTO, CHIME, HIRAX, HERA, STARFIRE, MeerKAT/SKA and SPHEREx. Finally, we describe recent theoretical advances: different approaches to modeling line luminosity functions, several techniques to separate the desired signal from foregrounds, statistical methods to analyze the data, and frameworks to generate realistic intensity map simulations.

List of Endorsers

The following people have endorsed this document as a 2017 Status Report for the Intensity Mapping field:

James Aguirre[1], Matthieu Bethermin[2], James Bock[3], Geoffrey C. Bower[4], Charles M. Bradford[3], Patrick C. Breysse[5], Philip Bull[6], Tzu-Ching Chang[6], Yun-Ting Cheng[3], Dongwoo Chung[10], Sarah Church[10], Kieran Cleary[3], Asantha Cooray[11], Rupert A. C. Croft[12], Clive Dickinson[13], Joshua S. Dillon[14], Olivier Doré[3,6], Michael W. Eastwood[3], Andrea Ferrara[15], Pedro G. Ferreira[16], Anastasia Fialkov[17], José Fonseca[18], Steven R. Furlanetto[19], Brandon Hensley[6], Daniel Jacobs[20], Marc Kamionkowski[21], Garrett K. Keating[22], Ely D. Kovetz[21], Elisabeth Krause[10], Guilaine Lagache[23], Daniel Lenz[3,6], Adam Lidz[1], Adrian Liu[24,25], Abraham Loeb[17,26], Tobias Marriage[21], Daniel P. Marrone[27], Kiyoshi Masui[28], Norman Murray[5], Laura Newburgh[29], Gergo Popping[30], Alkistis Pourtsidou[31], Anthony R. Pullen[32], Mubdi Rahman[21], J. Richard Bond[5], Dominik A. Riechers[33], Brant Robertson[34], Shun Saito[35], Mario G. Santos[18], Marta B. Silva[36], Rachel S. Somerville[37,38], Gordon J. Stacey[33], George Stein[5], Guochao Sun[3], Eric Switzer[39], Joaquin D. Vieira[40], Matteo Viel[41], Marco P. Viero[10], Francisco Villaescusa-Navarro[38], Eli Visbal[38], Amanda Weltman[42]

[1]Department of Physics and Astronomy, University of Pennsylvania, Philadelphia, PA 19104, USA
[2]Laboratoire d'astrophysique de Marseille, Joliot-Curie 13388 Marseille cedex 13, France
[3]Division of Physics, Math and Astronomy, California Institute of Technology, 1200 E. California Blvd. Pasadena, CA 91125
[4]Academia Sinica Institute of Astronomy and Astrophysics, 645 N. A'ohoku Place, Hilo, HI 96720, USA
[5]Canadian Institute for Theoretical Astrophysics, University of Toronto, 60 St. George st., Toronto, ON, M5S 3H8, Canada
[6]Jet Propulsion Laboratory, California Institute of Technology, 4800 Oak Grove Drive, Pasadena, CA 91109, USA
[7]That Institution, Another University, Country zipcode
[8]Those Departments, The University, State, Country zipcode
[9]Department, University, State, Country zipcode
[10]Kavli Institute for Particle Astrophysics and Cosmology and Physics Department, Stanford University, Stanford, CA 94305, USA
[11]Department of Physics and Astronomy, University of California, Irvine CA 92697
[12]McWilliams Center for Cosmology, Department of Physics, Carnegie Mellon University, 5000 Forbes Avenue, Pittsburgh, PA 15213, USA
[13]Jodrell Bank Centre for Astrophysics, School of Physics and Astronomy, The University of Manchester, Oxford Road, Manchester, M13 9PL, U.K.
[14]NSF AAPF Fellow, Department of Astronomy, University of California, Berkeley, 501 Campbell Hall, Berkeley, CA 94720-3411
[15]Scuola Normale Superiore, Piazza dei Cavalieri 7, 56126 Pisa, Italy
[16]Astrophysics, University of Oxford ,Keble Road ,Oxford OX1 3RH, UK
[17]Institute for Theoretical Computation, Harvard University, Cambridge, MA 02138, USA
[18]Department of Physics and Astronomy, University of the Western Cape, Cape Town 7535, South Africa
[19]Department of Physics and Astronomy, University of California Los Angeles, Los Angeles, CA 90095
[20]School of Earth and Space Exploration, Arizona State University, 781 E Terrace Mall, Tempe, AZ 85287
[21]Department of Physics and Astronomy, Johns Hopkins University, 3400 N. Charles St., Baltimore, MD 21218, USA
[22]Harvard-Smithsonian Center for Astrophysics, 60 Garden Street, Cambridge, MA 02138, USA
[23]Aix Marseille Univ, CNRS, LAM, Laboratoire d'Astrophysique de Marseille, Marseille, France
[24]Department of Astronomy and Radio Astronomy Laboratory, University of California, Berkeley, CA 94720, USA
[25]Department of Physics and McGill Space Institute, McGill University, Montreal, QC H3A 2T8, Canada
[26]Astronomy department, Harvard University, 60 Garden street, Cambridge, MA 02138, USA
[27]Steward Observatory, University of Arizona, 933 N. Cherry Ave., Tucson, AZ 85716 USA
[28]Department of Physics and Astronomy, University of British Columbia, 6224 Agricultural Road, Vancouver, BC ,V6T 1Z1, Canada
[29]Department of Physics, Yale University, New Haven, CT 06520
[30]European Southern Observatory, Karl-Schwarzschild-Strasse 2, 85748, Garching, Germany
[31]School of Physics and Astronomy, Queen Mary University of London, Mile End Road, London, E1 4NS, United Kingdom
[32]Center for Cosmology and Particle Physics, Department of Physics, New York University, New York, NY, 10003, USA
[33]Department of Astronomy, Cornell University, 220 Space Sciences Building, Ithaca, NY 14853, USA
[34]Department of Astronomy and Astrophysics, University of California, Santa Cruz, 1156 High Street, Santa Cruz, CA 95064
[35]Max-Planck-Institut fuer Astrophysik, Karl-Schwarzschild-Str. 1, 85748 Garching bei Muenchen, Germany
[36]Kapteyn Astronomical Institute, University of Groningen, Landleven 12, 9747 AG, Groningen, The Netherlands
[37]Department of Physics and Astronomy, Rutgers University, USA
[38]Center for Computational Astrophysics, Flatiron Institute, 162 5th Ave, 10010, New York,NY, USA
[39]NASA Goddard Space Flight Center, Greenbelt, MD, USA
[40]Department of Astronomy, The University of Illinois at Urbana-Champaign, 1002 W. Green Street, Urbana, IL 61801, USA
[41]SISSA, via Bonomea, 265 , I-34136 Trieste , Italy
[42]Department of Mathematics and Applied Mathematics, University of Cape Town, Rondebosch, 7700, South Africa

Preface

This Status Report presents the product of a growing global community of scientists who are involved in different aspects of line-intensity mapping research, an emerging field which promises new insights into the evolution of the Universe at low redshifts and into the Epoch of Reionization and Cosmic Dawn at higher redshifts. The line-intensity mapping field is still in a nascent phase, with only a handful of detected signals using a small list of instruments/datasets and a limited body of theoretical work to support it. This is set to dramatically change before the end of the current decade, as multiple experiments are coming online and considerable effort is devoted to plan observations, develop methods to analyze their data, and to study the implications for astrophysics and cosmology. Currently dozens of papers refer to "intensity mapping". While there are reviews of the study of the epoch of reionization with 21-cm fluctuations, there is no single document that provides an introduction to the broader field of intensity mapping, which includes growing attention to other atomic/molecular emission lines, a newer focus on cosmology at lower redshifts, and emerging prospects to study star formation and galaxy evolution up to high redshifts. This article is intended to provide this introduction, present the current state of affairs, and lay out its opportunities and challenges looking forward.

Starting in early 2016, the line-intensity mapping community began a series of annual workshops to help coalesce and advance the field. The pioneering meeting was a workshop titled "Opportunities and Challenges in Intensity Mapping" which took place at Stanford University (SLAC) March 21-23, 2016 and was attended by over 40 scientists. The second workshop, "IM@Hopkins", was held at Johns Hopkins University, June 12-14, 2017, with over 50 participants. In between, during and after these two workshops, efforts were dedicated to developing a document presenting a status report of the line-intensity mapping field. Through the workshops, presentations, personal writing assignments and feedback on drafts, over 45 scientists (from over 25 institutions) have contributed to this 2017 Status Report, while a small writing group was responsible for editing, combining and integrating the individual contributions. The next community workshop will take place in February 2018, at the Aspen Center of Physics.

Executive Summary

The aims of cosmology are to characterize the Universe on the largest observable distance scales and to understand its origin and evolution. Efforts to address these questions are intimately connected with parallel aims in extragalactic astronomy to characterize and understand the origin and evolution of galaxies and their interplay with the intergalactic medium. Progress in these questions are advanced today primarily by cosmic microwave background (CMB) experiments and by galaxy surveys. However, to anticipate the 2020 decadal survey planning process, it is important to identify and highlight new opportunities that may be fruitful in the advancement of cosmology and extragalactic astronomy.

Line-intensity mapping is an emerging technique with potential for dramatic scientific payoff. Unlike galaxy surveys, which determine the large-scale distribution of mass by locating huge numbers of galaxies, intensity mapping measures the integrated emission of spectral lines from galaxies and the intergalactic medium (IGM) with (smaller) low-aperture instruments. Information about the line-of-sight distribution is obtained through the frequency dependence. In this way, the cosmic luminosity density from a variety of spectral lines can be mapped over potentially a huge three-dimensional volume of the Universe and also at redshifts not easily accessed with traditional galaxy surveys. Line-intensity mapping can be uniquely applied to study large-scale structure, the epoch of reionization (EoR), and star/galaxy formation and has generated a tremendous flurry of activity over the past five years, in both theoretical research and the planning of dedicated experiments.

While most of the line-intensity-mapping effort has been on 21-cm emission from the neutral IGM, with several significant experimental efforts now afoot, there has more recently been rapid growth in the study of intensity mapping of line emission from galaxies, including the 21-cm line as well as those associated with rotational carbon-monoxide (CO) transitions, the [CII] fine-structure line, and the Lyα line, among others. Several groups are now pursuing ground-based measurements of CO and [CII] fluctuations, and NASA has recently selected SPHEREx for a MIDEX phase A study, a mission which has the potential for line-intensity mapping measurements of the Ha, Hb, OIII and Lya emission lines. The purpose of this status report is to describe the recent advances and prospects in line-intensity mapping. Given the significant prior attention on 21-cm, this report focuses primarily, though not exclusively, on intensity mapping with these other lines.

At large distance scales, line-intensity mapping probes large scale structure much like a galaxy survey, and thus addresses the growth of density perturbations, the primordial power spectrum, and from these follow tests of inflation and dark energy and possibly constraints to neutrino masses. Since every photon is measured, including those from unresolvable faint sources, huge volumes can be probed at high redshift, allowing unique tests of the standard cosmological model and its possible extensions. The intensity-mapping power spectrum can also be used to probe the luminosity functions of emitting galaxies, including luminosities too faint to be accessed through traditional measurements. Such measurements, as well as cross-correlations between different lines, offer the prospect to study the *universal* evolution of star/galaxy formation at high redshift, rather than the evolution of star formation in the high-redshift galaxies bright enough to be imaged individually. In particular, components such as diffuse emission, dwarf galaxies, Lyα scattering and the IGM will be very difficult to see in a point-source survey, but may contribute significantly to the overall luminosity probed by line-intensity mapping. Combining [CII]/CO/Lyα with 21 cm can provide a wealth of new information on the EoR, such as evolution of bubble size, ionization state, and metal production. Given the statistical nature of the HI data, this information is not practically feasible with catalog-based surveys.

The intensity-mapping community has recently achieved several breakthrough detections. 21-cm emission was first detected at $z \approx 0.8$ using GBT data in cross-correlation with the DEEP2 galaxy survey, and followed up in a deeper survey in cross-correlation with WiggleZ. Data from the Sunyaev-Zel'dovich Array have provided a first detection of the CO intensity auto-power. [CII] emission has been tentatively detected in cross-correlation between Planck and SDSS quasars. Lyα emission has been detected in cross-correlation

between BOSS cleaned spectra and the BOSS quasars. These detections have provided new views of neutral gas, molecular gas, and line transport and excitation. The recent BOSS measurement, to provide one example, implies a much higher overall Lyα luminosity than can be explained by the quasars themselves.

Intensity mapping instruments are now targeting a variety of interesting redshift ranges for the purposes of understanding the epoch of reionization, star formation, galaxy assembly, large scale structure, and Dark Energy. Multiple experiments anticipate having sensitivity to detect signatures of EoR, including HI experiments that target a power spectrum detection (HERA) and imaging (SKA-LOW), and experiments aiming for a detection in other emission lines (such as [CII] with TIME, CCAT-prime and CONCERTO). CO and [CII] lines have long been recognized as tracers of star formation, although much remains to be understood about the history of star formation and galaxy assembly. Intensity mapping experiments focusing on measurements of these lines plan to better understand these processes at high redshift around the peak of star formation, measuring star-formation properties in aggregate to improve constraints which are currently based on small sample sizes. The current generation of experiments range from tentative detections of CO (COPSS I, II) to pathfinders seeking a detection in CO (COMAP, AIM-CO) and [CII] (STARFIRE), and those targeting multiple lines (e.g. SPHEREx). Finally, neutral hydrogen traces the distribution of galaxies at lower redshift, and can be used for intensity mapping in radio frequencies at low spatial resolution (CHIME and HIRAX, optimized for a measurement of Dark Energy) or at higher resolution (SKA-MID).

A range of analysis challenges must be overcome to best extract science from upcoming line-intensity mapping surveys. Challenges include the presence of strong continuum foreground contamination, confusion from interloping emission lines and the non-Gaussian nature of the signal. Finally, for many emission lines of interest, a vast dynamic range in spatial scale is relevant, from the parsec scale of individual molecular clouds out to cosmological lengths of several giga-parsecs. The intensity-mapping community has started to attack these challenges head-on. Work is underway to model and simulate intensity-mapping signals reliably and to determine optimal analysis strategies, maximizing the scientific return from the upcoming surveys.

Several statistical approaches can be used to confront the challenges to intensity mapping. The cross power spectrum between the redshifted 21-cm signal during the epoch of reionization and line-intensity maps in other emission lines can help confirm initial detections, even in the presence of strong foreground contamination, and is sensitive to quantities such as the typical size of ionized regions at different stages of reionization. In the post-reionization era, the 21-cm line-intensity mapping signal can be cross-correlated with optical galaxy surveys, providing a powerful probe of galaxy evolution. Analysts have established regimes in which line-intensity mapping is more powerful than traditional catalog-based surveys, and proposed novel methods to explore and realize its tremendous potential: The one-point probability distribution of voxel intensities can exploit non-Gaussian information from upcoming surveys; The "multi-tracer" method can be applied profitably to multiple line-intensity mapping surveys to extract key quantities without the limitations of sample variance; A hybrid simulation approach combining high resolution hydrodynamic simulations to capture small scale physics, with the mass-peak-patch method to identify dark matter halos across cosmological volumes, will allow rapid, yet accurate mock survey realizations, important for anticipating future observations, interpreting upcoming data and testing analysis pipelines; Finally, several promising approaches for mitigating foreground interloper contamination have been developed, including blind bright-voxel and targeted masking techniques, as well as an anisotropic power-spectrum fitting methodology.

To close, there are great prospects for intensity-mapping surveys to uniquely address a large range of science goals, expecting early results in the near future. An array of small ground-based experiments, that capitalize upon existing hardware and infrastructure with small budgets, are rapidly making headway. They are guided by the experience of larger and more mature 21-cm projects that share some of the same science goals and techniques. There are good prospects for satellite missions with extraordinary capabilities. These experimental developments are motivating theorists to identify new science goals and opportunities and to address modeling and analysis issues, thus further advancing the promise of multi-line intensity mapping.

Contents

1

Introduction

1.1 What is Line-Intensity Mapping?

Line-intensity mapping represents an exciting and rapidly emerging new frontier in physical cosmology. It uses the integrated emission from spectral lines in galaxies and/or the diffuse intergalactic medium to track the growth and evolution of cosmic structure. The essential idea is to measure the spatial fluctuations in the line emission from many individually unresolved galaxies, rather than targeting galaxies one by one. The emission fluctuations trace the underlying large scale structure of the Universe, with the frequency dependence providing information about the distribution of emission along the line of sight. Unlike traditional galaxy surveys, which target only discrete objects whose emission lies above some flux limit, defined within a narrow aperture, intensity mapping is sensitive to *all sources of emission in the line*. It is therefore advantageous in studying faint and/or extended emission sources, and has prospects to further the *universal* study of galaxy formation/evolution (as opposed to the study of only the galaxies brightest enough to be imaged directly), in addition to probing the cosmological model in unexplored regimes. Since high angular resolution is not required, line-intensity mapping is also more economical than traditional galaxy surveys.

Fig. 1 provides a powerful demonstration of the potential gain. It compares the Very Large Array (VLA), an advanced radio telescope observatory consisting of 27 dishes, with a single-dish carbon-monoxide (CO) intensity mapping instrument (COMAP), in terms of their ability to observe a $2.5\,\mathrm{deg}^2$ sky patch. COMAP plans to spend $\sim$1500 hours observing a field of this size, whereas the VLA would take $\sim$4500 hours to cover the same area. While the VLA would detect only $\sim 1\%$ of the total number of CO-emitting galaxies, COMAP will produce a map of the intensity fluctuations sensitive to emission throughout the field.

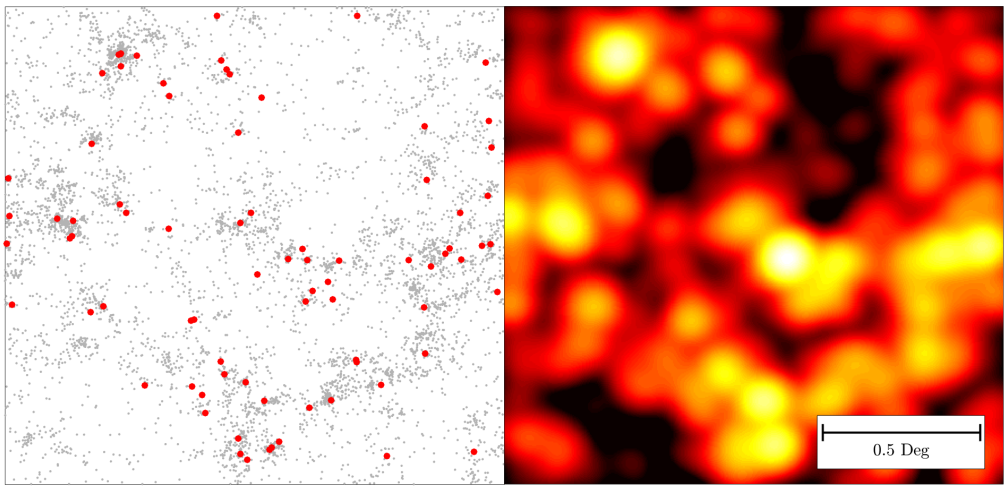

Figure 1. *A simulated* $2.5\,\mathrm{deg}^2$ *field with galaxy positions (Left) and the corresponding CO intensity map (Right). Luminosities were drawn from a Schechter function model (Breysse et al. 2016). Sources bright enough to detect with 1hr of VLA time are marked in red (see Li et al. 2016). (Figure: Patrick Breysse)*

1.2 Targets for Line-Intensity Mapping

A wide range of spectral lines have been considered for intensity mapping studies [1]. While most work has focussed on the 21-cm line, there is growing interest in the [CII] fine-structure line [2–4], the Lyα line [5–8], and rotational CO lines [9–14]. Much of the initial motivation was to probe the epoch of reionization [15] (EoR) at redshift $z \sim 10$, but increasingly the focus has extended to large-scale structure at lower redshifts. The experimental front has been evolving rapidly with several preliminary detections and a host of new experimental projects, which include an array of suborbital instruments, and at least two major satellite mission concepts [16, 17]. Fig. 2 shows the accessible scales and redshifts of some of these upcoming line-intensity mapping experiments.

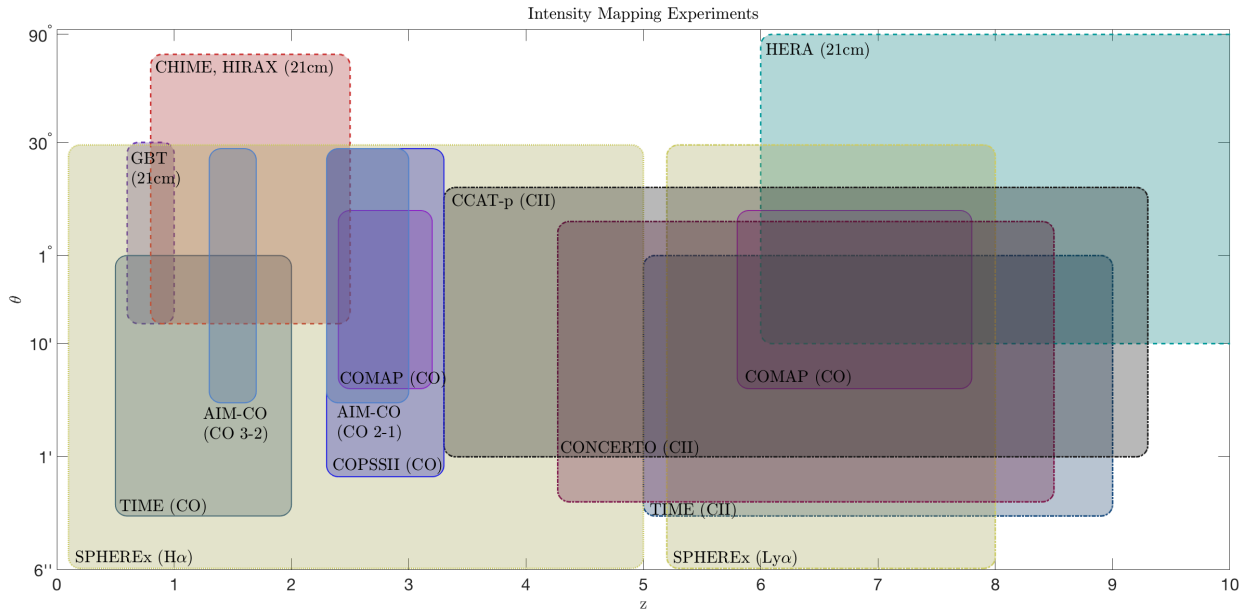

Figure 2. *A representative list of current and proposed intensity mapping experiments. The horizontal axis shows the redshift range of each experiment and the vertical axis indicates the range between the maximum resolution of the instrument and the total sky coverage. These include COPSSII, AIM-CO and COMAP which will target CO at medium redshifts, CONCERTO, CCAT-p and TIME which target [CII] at EoR redshifts, GBT, CHIME, HIRAX and HERA which target 21cm and SPHEREx which can measure Hα and Lyα over a wide range of redshifts at high-resolution. (Courtesy of Ely Kovetz and Patrick Breysse)*

One or more of the lines above is observable from redshifts of order unity to redshifts potentially as high as 20 or more. Under the prevailing ΛCDM cosmological model, this will make it possible to track the growth of the first structures, the reionization of the Universe and the emergence of dark energy (see Fig. 3). The accessible cosmic volume is so large that it may be possible to identify even small deviations from ΛCDM. Meanwhile, measurements of line-emission over large volumes of space at high redshift may provide a unique window into astrophysical properties such as the star-formation rate and the density of molecular clouds.

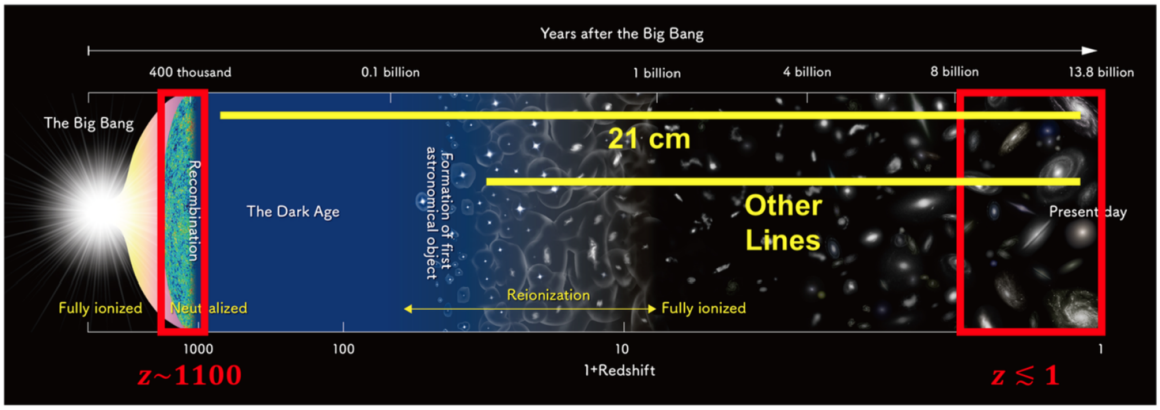

Figure 3. *Schematic view of the history of the universe. Red frames show the periods observed by the CMB (left) and by large galaxy surveys (right). The gap in between includes some of the most important periods in cosmic history, including the birth of the first galaxies during the dark ages, the epoch of reionization, and the growth of galaxies into the forms we see today. Yellow lines show the time periods accessible to intensity mapping surveys targeting the 21-cm line (top) as well as other lines (bottom), including CO, [CII], Lyα, and many others. (Original image credit: NAOJ)*

1.3 Basic Formalism

Before setting out to report on recent advances in the field and preview various efforts going forward, it is useful to present some of the basic formalism. We focus on the power spectrum of fluctuations in a line-intensity map of emission from galaxies at some redshift z. As the line-emitting galaxies are a discrete, biased tracer of the underlying dark matter fluctuations, the intensity mapping power spectrum will consist of clustering and shot noise components (shown in Fig. 4)

$$P_k(z) = \langle I(z)\rangle^2 b^2(z) P_m(k,z) + P_{\rm shot}(z) \tag{1.1}$$

where $b(z)$ is the redshift-dependent bias and the average intensity $\langle I(z)\rangle$ and shot noise power spectrum $P_{\rm shot}(z)$ are determined by the first and second moments of the line luminosity function $\Phi(L,z) \equiv dn(z)/dL$

$$\langle I(z)\rangle \propto \int_0^\infty L\Phi(L,z)dL, \qquad P_{\rm shot}(z) \propto \int_0^\infty L^2\Phi(L,z)dL. \tag{1.2}$$

Examining the different quantities in Eq. (1.1), one can get an idea of the different aspects of intensity mapping research. It is clear that the power spectrum above can ultimately be used to test the standard cosmological model in different epochs on various scales, through the dependence on the spectrum of dark matter fluctuations, as well as to study the astrophysical processes that take place in galaxies at different redshifts, as these determine the luminosity function of the target emission line.

1.4 The Scope of this Report

The rest of this document presents a snapshot of the line-intensity mapping field, based on contributions from dozens of scientists. While currently some of the most advanced stages of research involve mapping of

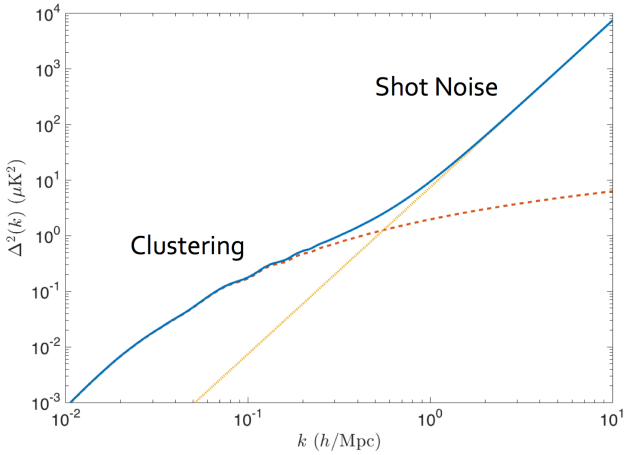

Figure 4. *The clustering and shot noise contributions to the line-intensity mapping power spectrum (same model as Fig. 1).*

the 21-cm line, with several major projects currently getting underway, we pay special attention to the more newly emerging areas of intensity mapping with other atomic and molecular lines[1]. In the first chapter, we describe the main science targets of line-intensity mapping research, which include the study of large-scale structure (cosmological parameters, inflation, dark energy), the star-formation history, and the study of galaxy evolution[2]. The next chapter describes the handful of preliminary detections to date. The multi-thronged experimental frontier, which consists of several collaborations targeting various lines with several ground-based instruments and at least two major satellite mission concepts, is reviewed in a separate chapter. On the theory side, several challenges need to be faced in order to fully exploit this technique and realize its ultimate potential as an astrophysical and cosmological probe. As we elaborate in dedicated sections below, one such challenge is how to model the intensity mapping signal; another is devising techniques to disentangle the signal from foregrounds (including line-interlopers in particular); and a third is how to best interpret the measured signal and extract efficient statistical constraints from it on quantities of interest ranging from the expansion rate of the Universe to the evolution of the star formation rate density. As can be seen, a great deal of progress has already been made in this newly emerging field, and the potential for new discoveries is quite promising.

[1] Our discussion of 21-cm studies of the epoch of reionization is brief, given several prior reviews [18–20] on the subject. We also refer readers to Refs. [16, 21] for more detailed discussions than provided here of intensity mapping with the Lyα line.

[2] Line-intensity mapping measurements may also have important implications for a variety of other areas of astrophysics—including asteroids, the interstellar medium, stars, and nearby galaxies (for more detail on these applications, see [21]).

2

Science Goals

Line-intensity mapping has the potential to provide important information in a variety of areas of astrophysics. The initial focus of intensity-mapping efforts was on the epoch of reionization [18, 19], primarily with 21-cm fluctuations. It was soon realized, though, that 21-cm intensity mapping can, with fewer experimental challenges, map large-scale structure at lower redshifts. It has then more recently been realized that relatively modest efforts can begin to probe the epoch of reionization and map large-scale structure at intermeditate redshifts with CO rotational lines, the [CII] line, and Lyα, and perhaps other lines. Recent theoretical work and initial experimental efforts have demonstrated that line intensity mapping has much to offer for the study of star formation, galaxy formation/evolution, and the intergalactic medium at high redshift. The field is rapidly growing and evolving, and new ideas for science with intensity mapping (e.g., new avenues to seek radiatively decaying dark matter [22] are now emerging at an accelerated pace). The science case for a space mission to do Lyα intensity mapping addresses a number of questions in Galactic, stellar, and planetary astronomy [21] that we do not address here. It is also important to note—as the case of fast-radio-burst studies with CHIME [23] demonstrates—that observational capabilities developed for intensity mapping may ultimately be useful in other ways that we cannot anticipate now.

2.1 Cosmology

2.1.1 Large-scale structure

Precision observational cosmology is becoming an increasingly crowded field, with a host of large-scale structure techniques now reaching a sufficient level of maturity to seriously compete with (and complement) the precision of CMB experiments. Notable examples include baryon acoustic oscillation (BAO) surveys, which have obtained $\sim 1\%$ precision on distance measurements out to $z \sim 1$ (with galaxies [24, 25]) and $z \sim 2.4$ (with the Lyα forest) [26]; weak gravitational lensing surveys, now covering areas as large as $5,000$ deg^2 to appreciable depths [27–30]; and redshift-space distortions from spectroscopic galaxy surveys, which have achieved better than 10%-level constraints on the growth rate of large-scale structure out to $z \sim 1$ (see the compilation in [31]). Taken together, these observables have pinned down the parameters of the standard flat ΛCDM model at around the 1% level or better [32], as well as uncovering several possible anomalies that, if confirmed, may point to new physics [33–38].

The question is whether intensity mapping, as a relative newcomer, has much to offer beyond what is already being provided by more mature methods like spectroscopic and photometric galaxy surveys. To answer this, it is instructive to look at the range of distance scales and redshifts that have been probed by existing methods, and that will be probed in the near future by planned surveys such as DESI [39], Euclid [40], and LSST [41]. An illustration is shown in Fig. 5, which focuses on linear scales (those with $k \lesssim 0.2$ Mpc^{-1}) out to $z \approx 6$; i.e. the post-reionization era.

Existing surveys (orange region in Fig. 5) have covered only a small corner of the space of accessible linear modes. They have mostly been restricted to redshifts of unity or less, with some limited coverage out to $z \approx 2.4$ from the Lyα forest. Arguably, no existing survey has reached scales larger than the matter-radiation

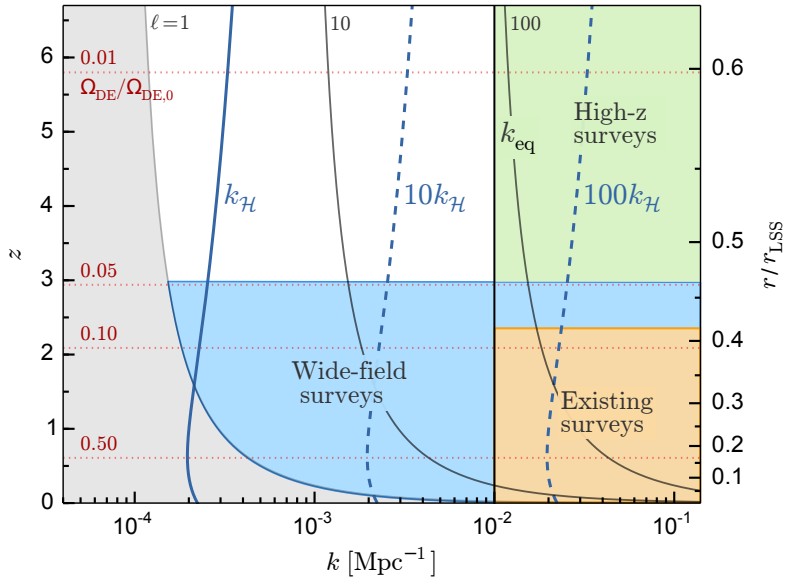

Figure 5. *Distance scales that are nominally reachable by current and future large-scale structure surveys, as a function of redshift (left vertical axis) and comoving distance to last scattering (right vertical axis). The red dotted lines show how the dark energy density is expected to change with redshift (assuming $w \simeq -1$), while the blue solid/dashed lines correspond to multiples of the Hubble scale, $k_{\mathcal{H}} \sim \mathcal{H}$, as a function of redshift. The black curved lines show the Limber-approximated Fourier wavenumbers corresponding to several spherical harmonic wavenumbers, ℓ, as a function of redshift. The shaded gray region shows modes with wavelengths larger than half the sky, and the thick black line shows the matter-radiation equality scale, $k_{\rm eq}$, where the matter power spectrum turns over. (Courtesy of Phil Bull)*

equality scale $k_{\rm eq} \approx 10^{-2}$ Mpc^{-1}, which marks the turnover in the matter power spectrum (the closest so far is BOSS [42]).

Forthcoming wide-field galaxy surveys (blue region) will be able to extend our reach to much larger scales, beyond the matter-radiation equality scale, and perhaps even out to the Hubble scale ($k \sim H_0$). This regime is particularly interesting for performing tests of general relativity and detecting signatures of primordial non-Gaussianity, as discussed below. Intensity mapping has a definite role to play here, as while the planned galaxy surveys will be able to reach the low-k regime in principle, they are not optimized for the task, and will likely struggle to mitigate a variety of large-scale systematic effects. Intensity mapping surveys tend to be cheaper and enjoy much faster survey speeds than optical galaxy surveys, as so it is plausible to design specialized surveys to study the very largest scales. An example of such a survey is SPHEREx, a space-based mission that will be surveying the entire sky with low resolution spectroscopic observations adequate for intensity mapping [16]. While not strictly optimized for the task, 21cm intensity-mapping experiments with large fields of view (e.g. SKA1-MID, CHIME and BINGO) should also be better suited to recovering large angular scales, especially at higher redshifts.

Intensity mapping is also invaluable for reaching higher redshifts (green region). Beyond $z \sim 3$, optical and near-IR galaxy surveys become much more difficult due to a combination of the large distances involved and the redshifting of the emission of the galaxies. The only currently planned galaxy surveys in the $z \gtrsim 3$ regime will cover comparatively small areas (e.g., HETDEX [43]). Intensity mapping is better suited for studying large-scale structure at high redshift, as the dilution of the signal—the aggregate emission from many galaxies, instead of just one—is less severe with distance/redshift.

Most current and near-future surveys focus on the $k \gtrsim k_{\rm eq}$, $z \lesssim 2$ regime because it corresponds to the period of dark energy domination, and contains a large number of linear Fourier modes (the total number of Fourier modes in a 3D survey naively scales like $k^3_{\rm max}$). There are a number of good reasons to extend our observations to larger scales and higher redshift though, especially if the goal is to perform precision tests of fundamental physics.

Below we consider the prospects of different line-intensity mapping measurements in placing constraints on ΛCDM through power spectrum measurements. As described in the Introduction, the amplitude of the intensity mapping power spectrum is given, at first order, by the power in dark matter density fluctuations times the square of the product of the bias and intensity of the line. Therefore, when comparing atomic and molecular emission lines it is not enough to compare their brightness; one has to also include the bias. In the top panels and bottom left of Figure 6 one can see how a selection of the most intense lines compare to each other in different regions of the electromagnetic spectrum [44]. These comparisons are highly dependent on the assumed model and the assumed gastrophysics and are only intended to suggest which lines might be targeted with intensity mapping experiments. The bottom right panel of Figure 6 gives the ratio between the power spectrum of a given line at a fixed comoving scale and its shot-noise power. In the future, one hopes that intensity mapping experiments become ever more sensitive to the point where shot noise becomes the dominant noise term. In that limit one can see that the radio to submilimeter lines are the ones that can perform better. It is also in that limit one should look for emission-line information encoded in the shot noise.

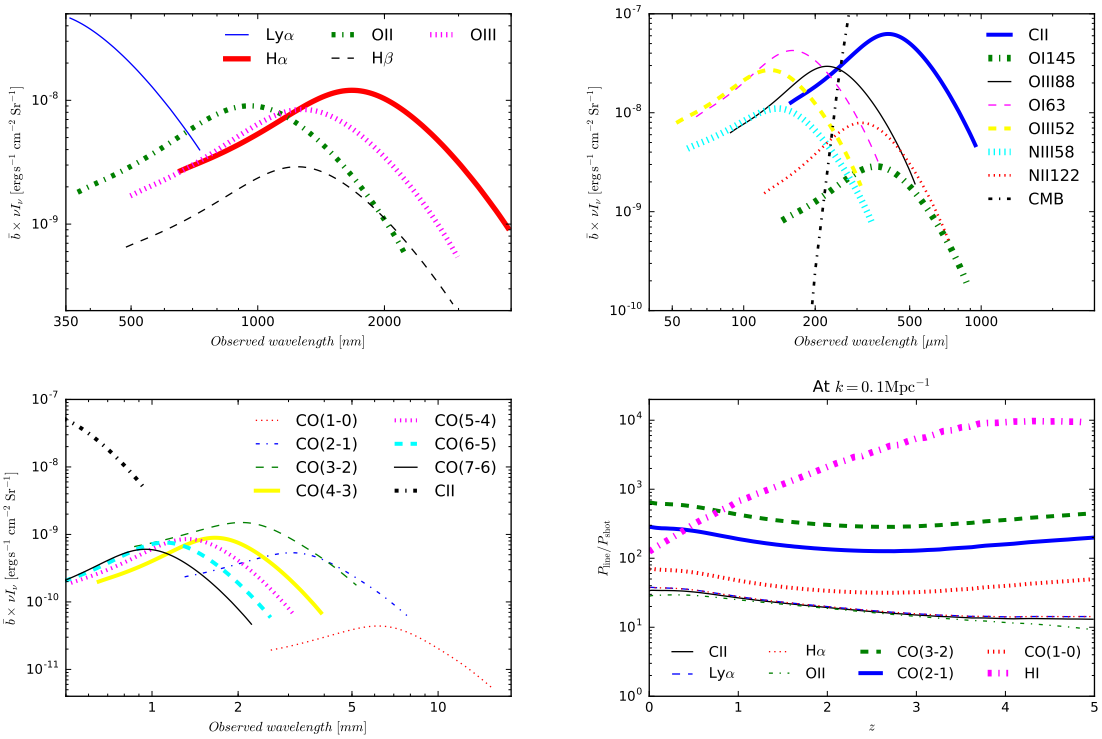

Figure 6. Comparison among atomic and molecular emission lines. Top left: *Optical and Near Infra-red emission lines.* Top right: *Far Infra-red emission lines.* Bottom left: *Far Infra-red to milimeter emission lines.* Bottom right: *Comparison between power spectrum of a given line at* $k = 0.1$ *Mpc*$^{-1}$ *and its shot-noise assuming an instrumental noiseless experiment. (Courtesy of José Fonseca)*

2.1.2 Probing the ΛCDM Cosmological Model

It is worth asking whether any current, planned or future intensity mapping instrument can provide robust measurements of the power spectrum at redshifts beyond the reach of current galaxy surveys, irrespective of the models one uses to estimate the cosmological average intensity of an emission line (see the Modeling Section for more details on how this can be done). An extensive study of this has been done in [44], from which we present a short summary in Table 2-1, indicating the lines used and the assumptions for the instrument specifications and observational strategies. While some lines still have low signal-to-noise ratios (SNRs), others have a great potential to measure not only the power spectrum, but the baryon acoustic oscillations (BAO) with great resolution.

Table 2-1. *Survey details in estimating $P(k)$ for the different lines in consideration.*

	Line	Area [deg^2]	z	δz	$\delta\Omega$ [10^{-9} Sr]	Δz	P_N [erg^{2}s^{-2}cm^{-4}Sr^{-2}Mpc^3]	k range [Mpc^{-1}]	SNR
HETDEX	Lyα	300	2.1	0.005	0.213	0.4	7.24×10^{-16}	0.009-0.3	489
SPHEREx	Hα	90	1.9	0.07	0.903	0.4	2.59×10^{-12}	0.009-0.3	105
	OII	90	1.2	0.05	0.903	0.4	1.34×10^{-11}	0.02-0.1	11
TIME-like	[CII]	100	2.2	0.002	13.5	0.4	4.59×10^{-13}	0.01-0.3	294
		2 (50h)					3.67×10^{-13}	0.05-0.3	42
	CO(3-2)	250	2.0	0.01	85	0.4	3.31×10^{-16}	0.01-0.3	471
		2 (50h)					1.06×10^{-16}	0.05-0.3	45

For instance, the forthcoming Hobby-Eberly Telescope Dark Energy Experiment (HETDEX [43]) can be a promising probe of the BAO signal, using Lyα intensity mapping. HETDEX was originally planned to analyze the large-scale clustering of Lyα emitters (LAE) detected with high S/N over 400 deg^2 (300 deg^2 for the spring and 100 deg^2 for the fall field) at $1.9 < z < 3.5$ (corresponding to $350 - 550$ nm wavelengths or the $545 - 856$ THz frequency range). However, the unbiased nature of HETDEX, which uses Integral Field Units, will also provide a Lyα intensity map, and its cross-correlation with the detected LAEs can be a powerful probe of the BAO signal [45].

One important goal of modern cosmology is a measurement of neutrino masses. Knowing their masses may also lead us to determine their hierarchy, allowing us to rule out a whole class of theoretical models aiming at explaining their masses. Neutrinos leave characteristic signatures on cosmological observables mostly due to the fact that they have very large thermal velocities, that make their dynamics very different to those of cold dark matter or baryons. In order to weigh neutrinos with cosmological observables, data from both large scales, e.g. CMB, and small scales, e.g. the Lyα-forest, is needed. This is precisely the regime where 21-cm intensity mapping holds promise since very large cosmological volumes can be probed down to relatively small scales. Besides, since intensity mapping can probe a very wide redshift range, the limitations on their bounds, arising from the degeneracies between neutrinos and other cosmological parameters, can be somewhat relaxed. Villaescusa-Navarro et al. [46] performed a detailed study through hydrodynamic simulations of the constraints that a combination of data from SKA1-MID, SKA1-LOW, Planck and a Euclid-like spectroscopic galaxy survey can place on neutrino masses. They find that the neutrino masses can be constrained (see Fig. 7) with a very competitive error of 34 meV (1σ).

As mentioned above, there exist degeneracies between cosmological parameters and astrophysical parameters at the epoch of reionization [47]. For example, Figure 8 shows forecasted parameter constraints from a HERA power spectrum measurement [48], where one sees a degeneracy between $T_{\rm vir}^{\rm min}$, the minimum virial

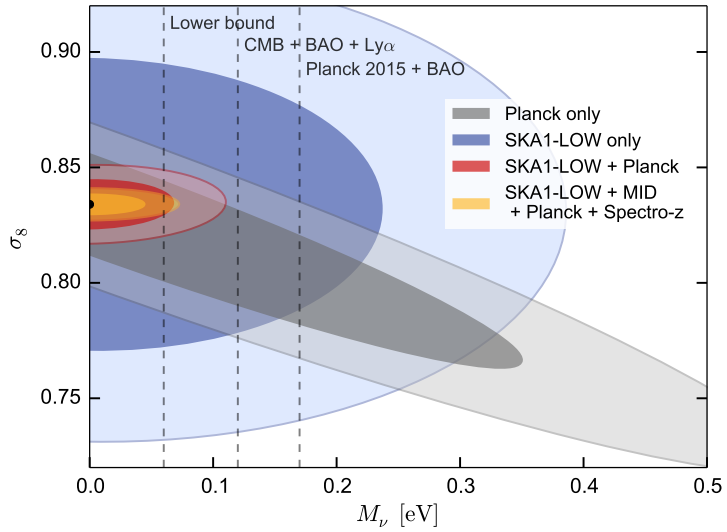

Figure 7. *1- and 2σ constraints on the sum of the neutrino masses, and its degeneracies with σ_8, from Planck (grey), SKA1-LOW (blue), SKA1-LOW + Planck (red) and SKA1-LOW + SKA1-MID + Planck + Euclid (yellow). The lower limit from neutrino oscillations, together with the bounds from CMB+BAO+Lyα, and Planck 2015 95% limits are shown as vertical dashed lines from left to right respectively. (Courtesy of Francisco Villaescusa-Navarro)*

temperature of ionizing halos, and σ_8. This arises because a higher σ_8 accelerates structure formation, and thus moves reionization to an earlier epoch. One can then compensate for this by raising $T_{\rm vir}^{\rm min}$, which limits the ionizing influence of galaxies to only the most massive galaxies, thus delaying reionization. From this, we see that even with the *Planck*-level errors on cosmological parameters assumed in Figure 8, uncertainties in cosmological parameters cannot be neglected even if the goal is on constrain astrophysics.

While the necessity of including cosmological parameters in the analyses may seem like a burden, it is also an opportunity, for it means that high-redshift 21 cm experiments can in principle place competitive constraints on cosmological parameters. Conceptually, this is unsurprising, given their vast (∼hundreds of Gpc^3) survey volumes. The challenge, however, is in the extraction of this cosmological information from amidst the messy astrophysics of reionization. There are several approaches to this:

- The most direct approach is simply to treat the astrophysical and cosmological parameters on an equal footing, varying both in simulations of the 21 cm power spectrum [47, 48]. This then allows a simultaneous fit of all parameters to the observed power spectrum. The disadvantage of this is that reionization simulations are computationally expensive, and therefore this approach has only been explored for semi-analytic simulations (and even then the problem is only barely tractable [48]).
- An alternative approach has been to assume that the power spectrum of the ionization field and the cross-power spectrum between the ionization and density fields are both proportional to the matter power spectrum. The proportionality constants are then parameterized by a functional form motivated by fits to radiative transfer simulations. The free parameters in the functional form are treated as nuisance parameters in the data analysis and marginalized out [49, 50]. For this approach to be robust, however, early observations must confirm the parametrized forms. Additionally, typical treatments of

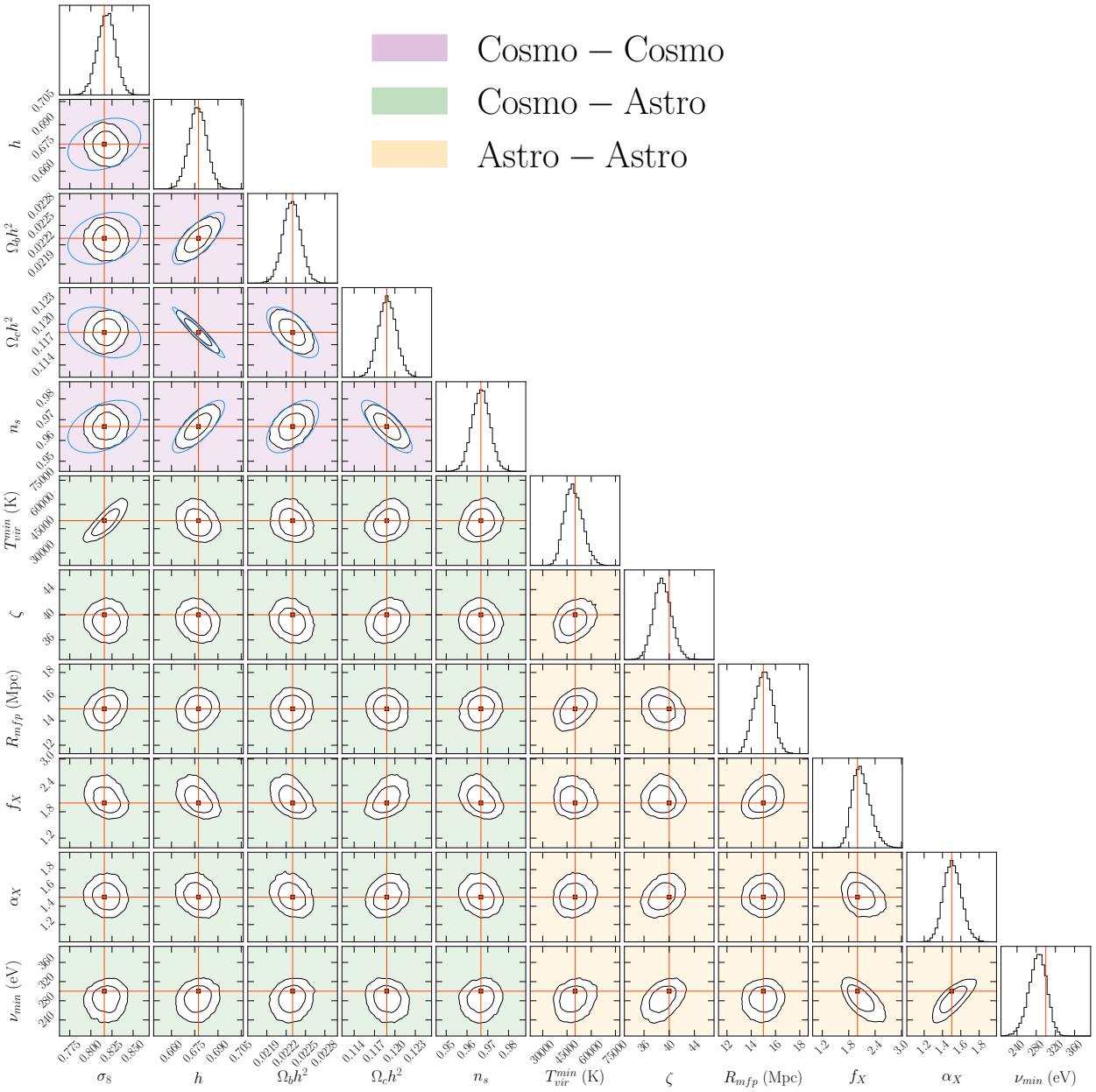

Figure 8. *Forecasted* 68% *and* 95% *confidence regions for HERA, using a reionization model parameterized by* σ_8, h, $\Omega_c h^2$, n_s, *the minimum virial temperature of ionizing halos* $T_{\rm vir}^{\rm min}$, *the ionizing efficiency of UV photons* ζ, *the mean free path of ionizing photons* $R_{\rm mfp}$, *the X-ray flux amplitude* f_X, *the X-ray spectral index* α_X, *and the X-ray cut-off frequency* $\nu_{\rm min}$. *Red squares indicate the fiducial values of this forecast, while the blue contours show the* 95% *confidence regions from* Planck *alone. Reproduced from [48]. (Courtesy of Adrian Liu)*

this approach have assumed that the nuisance parameters are not themselves dependent on cosmological parameters.

- A final approach is to move away from the model dependence of the previous approaches, and to instead use redshift space distortions. The core idea is that redshift space distortions are sourced by the underlying density field, rather than ionization fluctuations. Building on this idea, Barkana and Loeb [51] showed that to linear order, a separation of the 21 cm power spectrum into powers of μ (where μ is the cosine of the angle of the Fourier mode with respect to the line of sight) yields a μ^4 component that depends only on the density fluctuations. By extracting this component from the data, one evades astrophysical parameters and directly constrains cosmological ones. However, in doing so, one discards information content (since the portions of the signal that are intertwined with astrophysical parameters *do* contain cosmological information, albeit information that is difficult to access). Forecasts therefore predict less stringent parameter constraints with this method [49]. Moreover, one must be cognizant of the possibility that nonlinear fluctuations could spoil the separation of astrophysics and cosmology, with simulations suggesting that the separation works only early in reionization ($\lesssim 40\%$ ionized; [52]).

In practice, a robust estimation of cosmological parameters from high redshift 21 cm surveys may involve a combination of all these approaches.

Lastly, we note that instead of directly constraining cosmological parameters, a possible alternative is to use high redshift 21 cm surveys to concentrate on measuring astrophysical parameters, which can then be used to forward model any reionization nuisance parameters in other cosmological probes. For example, CMB studies need to fit for the optical depth τ, which arises due to the Thomson scattering of CMB photons by electrons in the IGM. Since these electrons are the result of the reionization process, a successful 21 cm measurement can—through modeling—be converted into a prediction for τ [53]. Though such a measurement would be model-dependent (recall that the 21 cm brightness temperature probes a specific mixture of ionization, temperature, velocity, and density fluctuations, rather than each of these individually), it would nonetheless be valuable, since a τ prediction would break A_s-τ degeneracies in the CMB.

2.1.3 Going beyond ΛCDM

Intensity mapping is ideally suited to provide constraints on the possible time variation of the equation of state $w(z)$ of dark energy which is one of the major focuses of observational cosmology. While dark energy dominates the cosmic energy density at the lowest redshifts, this is not necessarily the best regime in which to look for departures from a cosmological constant, $w = -1$. Most current surveys focus on a broad redshift range around $z \sim 1$, but significant deviations from a cosmological constant are more likely to occur at higher redshift, $z \gtrsim 2$, in a large class of models. Results from [54]—a Monte Carlo exploration of many millions of physically-viable Horndeski single-scalar field models—are shown in Fig. 9. These models have five arbitrary time-dependent coupling functions that were parametrized in several different ways, with coefficients chosen from broad prior distributions. The models were then evolved to find $w(z)$, and unphysical models (e.g. with ghost instabilities) discarded. The result is a prior probability distribution over the space of possible Horndeski $w(z)$ functions. As shown in Fig. 9, both the simplest Horndeski subclass (minimally-coupled quintessence models), and the most general, exhibit a typical 'tracking' behavior, where $w \simeq -1$ at low redshift, but deviates significantly ($w \to 0$) at $z \gtrsim 2$. While there can be several different causes of this behavior, the most common is due to non-minimal couplings, which force the scalar field to track the evolution of the dominant component of the cosmic energy density. This seems to be quite generic, at least for scalar field theories. As per Fig. 9, the transition from matter domination ($z \gtrsim 2-3$) therefore seems to

be a particularly promising place in which to search for deviations from a cosmological constant, making it an interesting target for intensity mapping surveys (see, e.g., [55]).

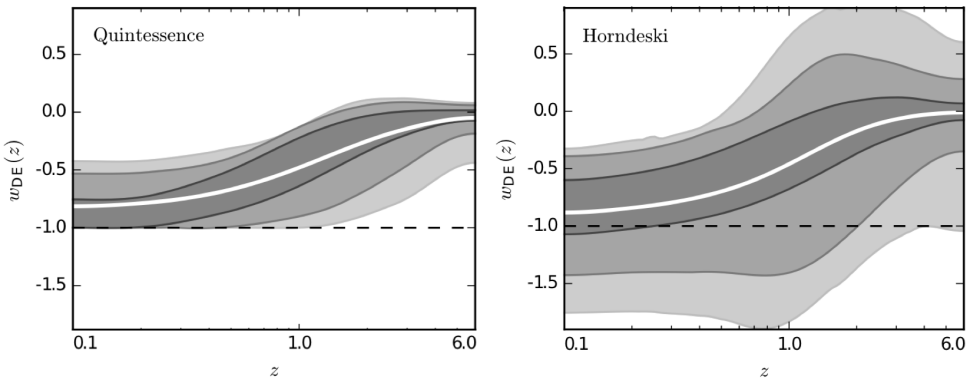

Figure 9. *Prior distributions of $w(z)$ for the Horndeski class of scalar field models, adapted from the Monte Carlo study of [54]. The left panel shows the results for minimally-coupled (quintessence) subclass, while the right is for the general class. The contours show 68%, 95%, and 99.7% intervals, while the white line shows the median. There is a clear tendency in these models to deviate from $w = -1$ at $z \gtrsim 1$. (Courtesy of Phil Bull)*

Beyond constraining modified gravity theories through their equation of state, intensity mapping experiments offer the promise of constraining screening mechanisms, [56, 57] through their environment dependent behavior. Astrophysical tests of gravity theories, including chameleon [57] and Vainshtein [58] screening depend on the distinct signatures of each theory and the environment under study. Thus nuanced experiments can tease out their effects, in varied ways, including a comparison of the mass distribution inferred by different probes. Intensity mapping experiments, in concert with high resolution optical imaging and spectroscopy will allow us to study the different behavior of different components of galaxies and thus potentially constrain or rule out these theories. For a comprehensive discussion of such tests, see [59] and references therein.

The 21cm signal from pre-stellar times is a sensitive probe of new physics, and dark matter in particular, much in the same way of the CMB [60–62]. For example, dark matter annihilation at early times could provide an early and uniform source of heat [63]. This model is distinguishable from standard models by its spatial distribution and timing [64]. The effect is generally one of de-emphasizing large fluctuations and increasing the pace of heating. The opposite is also possible, a non-zero cross-section between cold dark matter and baryons could drive the gas temperature below or above that expected by Hubble expansion, depending on the dissipation of kinetic energy into heat as a result of friction between the baryon and dark matter fluids, significantly increasing the emission/absorption signal [65]. In both of these cases intensity mapping at $z > 20$ becomes an exploration of basic physics.

Another strong motivation to access ultra-large scales with intensity mapping measurements is the possibility to detect hints of primordial non-Gaussianity, which occurs in certain types of multi-field inflation (see, e.g., the discussion in [66]). If non-Gaussian correlations were imprinted in the curvature perturbations left over after inflation, then one would expect to see a scale-dependent bias in the two-point function of a biased tracer of the underlying density field [67]. This effect is mostly limited to very large scales (the bias correction is $\propto k^{-2}$), and so as with relativistic corrections, a multi-tracer approach will be useful here too [68–70] (see the Techniques Section for more details).

2.1.4 The Physics of the Epoch of Reionization

Galaxy surveys by the Hubble Space Telescope have dramatically improved our understanding of the Epoch of Reionization (EoR) [71], but our knowledge of the detailed connection between the galaxy population and the evolving state of the intergalactic medium can be revolutionized through line-intensity mapping signals. This is especially true if one uses measurements of several different lines originating from this epoch in tandem, to obtain complementary information about the physical processes that are taking place [10]. To appreciate the potential of line-intensity mapping in providing a unique picture of EoR, consider the illustration in Fig. 2.1.4. The 21-cm line maps the neutral gas from outside of the ionized bubbles, while CO and [CII] lines trace the star-forming galaxies that create the ionizing photons, most of which are too faint to detect. Lyα probes the galaxies as well, along with the halos around them. Together, these lines allow the study of the wide range of spatial scales and physical processes which contribute to reionization. Cross-correlations between these lines will add additional information about their relationships, and correlations with fainter lines will probe astrophysical conditions in ever more detail.

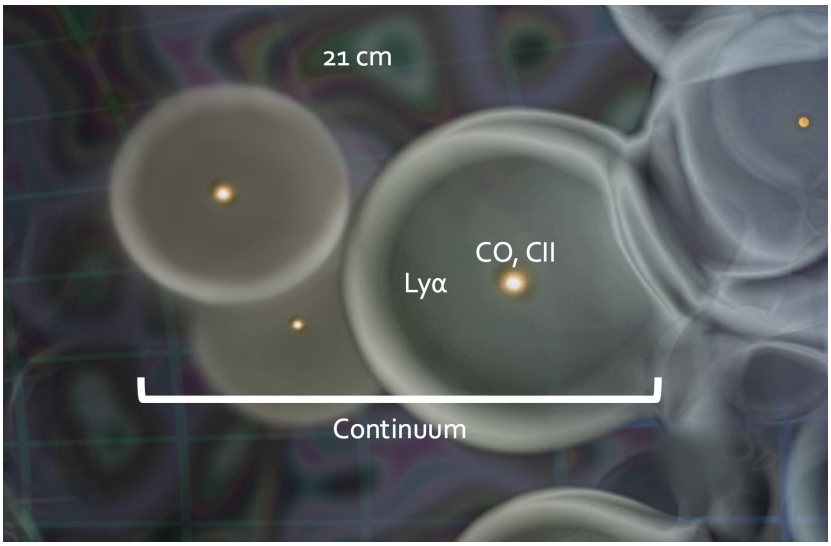

Figure 10. *This is an illustration of the signals from CO and [CII] from within galaxies, Lyα from around galaxies, and 21-cm from neutral IGM. Fainter lines can be seen in cross-correlation, while the continuum is measured as the cosmic infrared background. (Background Image Credit: Scientific American - pending approval) (Courtesy of Patrick Breysse)*

The prospects to probe the astrophysics of reionization with intensity mapping experiments have been considered in more detail for the 21 cm line. For instance, instruments such as the Hydrogen Epoch of Reionization Array (HERA; [72]) are forecasted to provide $\sim 10\%$ to 20%-level constraints on parameters such as the minimum virial temperature of ionizing halos, the ionizing efficiency of these halos, the UV and X-ray emissivities of ionizing sources, and the mean free path of ionizing photons in ionized regions [73–75]. Such forecasts assume that the survey volume is subdivided into several redshift bins (say, bins of thickness $\Delta z = 0.5$), and that a series of power spectrum measurements are made, one in every bin. Note that unlike with low-redshift 21-cm intensity mapping surveys, experiments targeting reionization are sky-noise dominated (owing to the brighter foreground sky at the lower observation frequencies). Thus power spectrum measurements generally lose signal to noise in the highest redshift (lowest-frequency) bins fairly quickly (depending on the particular survey and the foreground removal techniques used). However,

these noisier measurements are still crucial for breaking degeneracies between reionization parameters [73]. We also note that degeneracies between cosmological parameters and astrophysical parameters need to be taken into account when extracting astrophysical information from IM measurements, even with *Planck*-level uncertainties on the former [47].

2.1.5 Cross-correlation of Intensity Mapping with Other Probes

Large-area 21-cm intensity mapping surveys [76–81] that trace low to medium redshift line emissions allow for the possibility of interesting cross-correlations with other probes. One possibility is to consider cross-correlation with CMB surveys. The southern hemisphere location of HIRAX [78] (see Experiments Section), for example, makes it ideal to cross-correlate the measured 21cm brightness fluctuations with various CMB probes of the large-scale structure that will be measured by AdvACT [82] and SPT3G [83]. Direct correlation with CMB surveys is challenging because of the loss of long-wavelength line-of-sight modes in the 21cm brightness field after foreground removal (see Techniques Section). However, higher order correlations of the 21cm brightness field [84] or tidal field reconstruction [85] can provide an observable signal. Higher order cross-correlations with the reconstructed CMB lensing field [84] will allow us to constrain the high-redshift matter power spectrum and the change in the HI density and bias with cosmic time, independently of the optical galaxy bias that enters in the optical galaxies-21cm intensity mapping cross-correlation [86].

An advantage of IM over conventional spectroscopic galaxy surveys lies in the ability to cover extremely large cosmological volumes in a relatively short time. Galaxy surveys must threshold far above the noise level to ensure that candidate sources are not simply noise fluctuations. This throws away a large fraction of the signal, and results in slow survey speeds, especially when spectra must be obtained. Thresholding is not necessary with intensity mapping, where the whole (noisy) signal can be kept in the analysis. The reduced resolution requirements of IM also allow for survey instruments with a wider instantaneous field of view. This, along with the high spectroscopic resolution of radio receivers, allows 21 cm IM experiments to achieve extremely high survey speeds, translating into considerably wider survey areas at a given depth.

Increasing survey volumes is a straightforward way of improving precision on the BAO, as galaxy surveys tend to be limited by sample variance rather than other factors. Purpose-designed IM surveys are easily capable of surpassing the effective volume of almost any galaxy survey, but suffer from an array of additional systematic effects that make the sample variance limit harder to achieve. Mitigation of these issues, particularly foreground contamination and instrumental calibration uncertainty, has been discussed elsewhere, but remains a serious unknown in performance comparisons of IM and galaxy survey techniques.

One way around this is to consider synergistic analyses that combine intensity mapping data with overlapping galaxy surveys. Cross-correlation was already used to good effect to filter-out foreground contamination in the GBT $\times$ WiggleZ 21 cm signal detection [86]. Reconstruction of the real-space density and velocity fields using a combination of 21 cm IM and low-density galaxy samples has also been investigated as a way of correcting for foreground removal effects and sharpening the recovered BAO feature ([87, 88]). Another possible target was suggested in [89], which demonstrated how cross-correlations with galaxy catalog subsamples can characterize gas in galaxies as a function of optical properties. Using tomography techniques, it may also be possible to use the high-resolution spectroscopic redshift information from low angular resolution IM surveys to improve photometric redshift estimates from galaxy surveys [90]. Most planned low-redshift 21 cm IM surveys are large enough that there will generally be significant overlap with at least one large galaxy survey, although some level of coordination in survey design will be necessary to optimize returns from combined analyses with next generation galaxy surveys such as LSST.

2.2 Galaxy Assembly and Star-Formation/IGM Interplay

Intensity mapping opens a new method to probe the physics of phenomena at high redshift that would otherwise be unreachable by classical methods. Current measurements of the star-formation history, for example, indicate that the star formation rate density (SFRD) increased as the Universe evolved until reaching a peak around $z \sim 2-3$, and has been declining ever since [91]. However, our knowledge of star formation in the distant universe comes from the relatively small population of high-redshift galaxies bright enough to be imaged directly (see, e.g. [92]). The contribution from these highly obscured galaxies (which are detected in the rest-UV) is highly uncertain.

This situation therefore has the potential to greatly improve using intensity mapping, which grants access to the statistical properties of a large population of faint sources which cannot be individually detected. Through intensity mapping, one can trade object localization for an unbiased, highly sensitive measure of high-redshift molecular gas that provides a direct comparison to optical and near-infrared star-formation histories. Carbon-monoxide intensity mapping, for example, provides a particularly compelling avenue toward understanding high-redshift star formation. Most of our current knowledge of star formation in high-redshift galaxies from UV/optical/IR observations comes from stellar light and emission lines from the hot ionized gas in the ISM. Star formation, however, takes place in the cold molecular gas which is traced by line emissions such as CO.

Targeted observations have probed cold gas in galaxies out to redshifts $z \simeq 7$ [93], but only in rare extremely bright objects that are not characteristic of the high-redshift star-forming population [94]. Blind surveys have integrated on regions that are too narrow to provide the statistics required to constrain the high-redshift CO luminosity function [95]. As a result, models for the CO luminosity density at high redshift vary by orders of magnitude [96]. By collecting the light from thousands, if not millions, of unresolved galaxies—not just the few that are bright enough to be imaged directly—intensity mapping offers the prospect to pin down the cosmic CO luminosity density, and thus the star-forming-gas reservoir, at high redshifts.

To get an idea of the prospects of line-intensity mapping to access astrophysical information at high redshifts, we consider the use of CO intensity mapping at $2 < z < 3$. As elaborated in different Sections of the report below, current (i.e. COPSS; [97]) and future CO intensity mapping experiments (i.e., COMAP; [98]) will provide direct constraints on the CO luminosity function at these redshifts. These can then be used to infer constraints on key astrophysical quantities, such as the SFRD across cosmic times. In [96], it was demonstrated that the cosmic star-formation history can be effectively measured with one-point statistics of CO maps, using a $P(D)$ analysis to infer the luminosity function of CO-emitting sources from the measured voxel intensity distribution (see Section 5 for more details). This constraint hinges on our ability to model the relation between the CO luminosity and the SFRD. This can be done through a series of empirical relations, namely the relation between the CO luminosity and the far infrared luminosity (FIR) of a galaxy, and subsequently the relation between FIR luminosity and the star-formation rate (more in Section 5). In an ideal setting, with no foregrounds, noise or modeling uncertainty, an experiment such as full COMAP (see Section on Experiments) will be able to constrain the SFRD to $\sim 1\%$ accuracy at redshift $z \lesssim 3$. Fig. 11 demonstrates the potential of this technique when line foregrounds, instrumental noise and modeling uncertainties are included. Comparisons between intensity maps and galaxies using targeted observations in small patches of sky with advanced instruments such as ALMA, could substantially reduce the latter.

An additional line which has been proposed as an interesting high-redshift probe is the He II 1640 Å recombination line [100]. This line is thought to be a signature of metal-free Population III (Pop III) stars formed from pristine gas left over from the Big Bang. This is because massive Pop III stars produce many more He II ionizing (i.e. > 54.4 eV) photos than metal enriched stellar populations [101]. One of the main challenges in observing Pop III stars is that they are generally expected to form in very small galaxies which will be extremely difficult to detect directly even with powerful telescopes such as JWST. Intensity

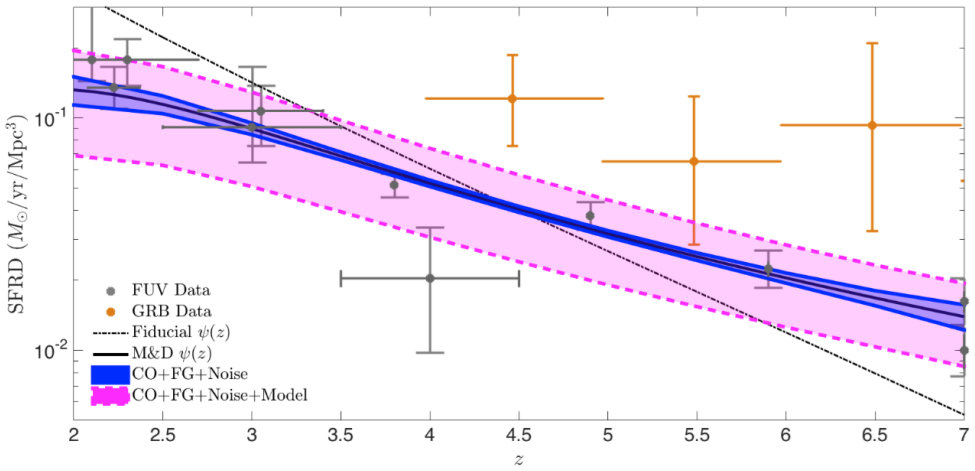

Figure 11. *Comparison between predicted constraints on star-formation rate density from CO intensity mapping and from existing FUV (grey points) [91] and GRB (orange points) data [99]. Solid black curve $\psi(z)$ shows fit to FUV data [91]. Blue curves show $\pm 1\sigma$ SFRD uncertainty forecast with CO intensity mapping, taking into account foregrounds and noise. Dashed magenta lines include a 10% model uncertainty in the adopted CO-FIR and FIR-SFR relations. From Breysse et al. [96]. (Courtesy of Ely Kovetz)*

mapping is capable of measuring the cumulative signal from all of these very faint sources and is therefore one of the most promising probes of Pop III stars. In [100], the He II intensity mapping signal was estimated as a function of redshift. It was shown that the Pop III signal may dominate over the contribution from quasars and Wolf-Rayet stars, and could potentially be measured at $z \approx 10$ with high signal-to-noise by a space-based instrument that could be built in the relatively near future. Another desirable feature of the He II 1640 Å line is that (much like Lyα) it requires no metal enrichment. In principle its intensity maps could be observable at very high-redshift before large quantities of metals have been produced. Thus, it may be a promising line to cross correlate with 21-cm emission during the EoR.

Beyond single-line cross-correlations, molecular line physics enables cross-correlation between lines of isotopologues, for instance ^{12}CO and ^{13}CO, providing probes into the density of cosmic molecular gas, on top of the inherent ratio between the two isotopologues as a function of redshift [102]. The spectral proximity of the two emission lines (rest $\Delta\nu = 5$ GHz) allows current and planned experiments to measure both lines simultaneously, minimizing noise that may arise from systematics between different experiments. While the ^{13}CO is subdominant to the ^{12}CO at any given frequency, the cross-correlation between the two lines can expose this information, which is a function solely of the molecular physics and demographics. Breysse and Rahman [102] demonstrate that constraints of this cross-correlation from currently planned experiments will provide information on the molecular gas distribution, as well as the isotope ratio of ^{12}CO and ^{13}CO; the former directly related to the mechanism of star formation, the latter to star-formation history. This probe can potentially provide direct insight into the physics of star formation at a redshift previously inaccessible.

Finally, intensity mapping surveys are well-suited to measuring the integrated emission from faint sources of emission. A substantial fraction of the baryons in the Universe reside in diffuse, faintly-glowing phases of the IGM, and have thus proven difficult to detect and characterize [103, 104]. A recent Lyα intensity mapping analysis was able to measure some properties of the faint IGM [105]. Similar techniques can be used to further constrain the density, evolution, and clustering behavior of the IGM, and will complement other probes such as the kinetic Sunyaev-Zeldovich effect [106].

3

First Detections

There have been several detections of line-intensity fluctuations with existing instruments and novel observational approaches and analyses. These already provide unique constraints to the reservoir of cold molecular gas at high redshift. We describe these detections in order of decreasing wavelength.

3.1 Detection of 21cm in Cross Correlation

The first detection of the redshifted 21-cm emission in the intensity mapping regime was demonstrated by Chang et al. [107]. The authors conducted a 21 cm survey spanning the redshift range of $0.53 < z < 1.12$, corresponding to a comoving distance of $1400 - 2600$ Mpc/h, by utilizing the 800 MHz receiver at the Green Bank Telescope (GBT). The survey fields overlap with two of the DEEP2 optical galaxy redshift survey fields [108], each $120' \times 30'$ in angular size out to $z = 1.4$, and contain $10,000$ DEEP2 galaxies in total. The FWHM of the GBT beam of $15'$ corresponds to 9 Mpc/h (comoving) at $z = 0.8$, and the high intrinsic spectral resolution is binned to 430 kHz, or 2 Mpc/h.

The dominant sources present in the data are the radio frequency interference (RFI) and continuum foreground emission from astrophysical sources, notably the Galactic and extragalactic synchrotron radiation. The RFI is polarized and excised using cross-correlation of the two linearly polarized radio signals. The astrophysical continuum sources present a fluctuation in brightness temperature of ~ 125 mK, about 1000 times brighter than the sought-after 21 cm signals. However, they are spectrally smooth and distinct from the 21 cm fluctuations which have redshift and thus frequency structures, and can be identified as the dominant spectral eigenmodes using the singular-value decomposition technique and subtracted from the data.

After the above analysis, the authors measure the residual intensity field and reported an upper limit to the 21 cm brightness temperature fluctuation of $464 \pm 277\,\mu$K, on a pixel scale of $(2\mathrm{Mpc}/h)^3$, at a mean redshift of 0.8. The authors further performed cross-correlation analysis of the 21 cm intensity field with the underlying cosmic density field as traced by the DEEP2 galaxies [109]. They reported a positive cross-correlation on a scale of ~ 10 Mpc/h, with an amplitude of $157 \pm 42\,\mu$K at zero lag Fig.12. The amplitude constrains a combination of HI abundance, bias parameters and stochasticity, and the authors infer a value for HI abundance, $\Omega_{\mathrm{HI}} = (5.5 \pm 1.5) \times 10^{-4}(1/rb)$ at $z \sim 0.8$, where r is the stochasty between the 21 cm and optical galaxy tracers, and b the bias parameter of HI. The respective intensity fields of the radio, 21 cm and optical galaxies are shown in Fig.12.

The cross-correlation detection is significant as it verifies that the 21cm intensity field correlates with and thus traces the distribution of optical galaxies, which are known tracers of the underlying matter distribution. This serves as a proof of concept for the line-intensity mapping technique, and signifies line-intensity mapping as a viable tool for large-scale structure studies. Subsequent, deeper observations with the GBT have measured the 21 cm signal in cross-correlation [86] with WiggleZ [110] and used the auto- and cross-correlation to bound the 21 cm signal [111]. [112] describes the methods used in analyzing the GBT maps.

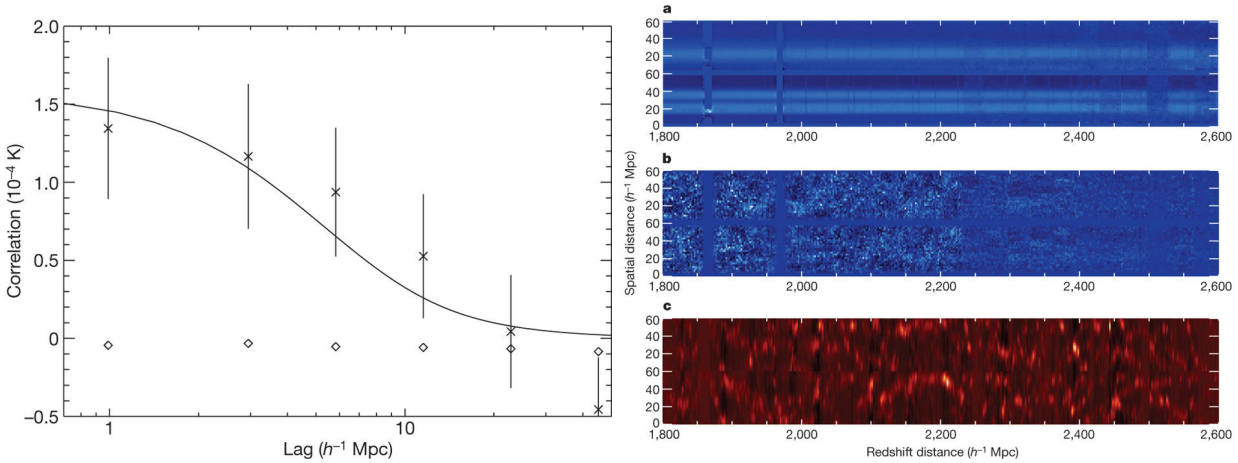

Figure 12. *Left: The cross-correlation between the* 21 *cm brightness temperature and the DEEP2 galaxy density field. Crosses are the measured cross-correlation amplitudes, and error bars are the* 1σ *bootstrap errors generated using randomized optical data. The diamonds are the mean null-test values over* 1000 *randomizations of the optical source position. The solid line indicates a power law DEEP2 galaxy correlation model [109], convolved with the GBT beam pattern and velocity distortions, with an amplitude from the best-fit value of the cross-correlation. Right: Spectra of the DEEP2 field. Panels a, b, c show the radio flux after RFI excision, a proxy for the 21-cm intensity field after foreground subtraction, and the density field as traced by the DEEP2 galaxies, respectively. The fields are arranged with redshift horizontal and spatial vertical. (Courtesy of Tzu-Ching Chang)*

3.2 Detection of CO Fluctuations

Intensity mapping experiments are well-suited for data sets with large survey volumes, requiring only modest point-source sensitivity to detect an aggregate signal. As such, the Sunyaev-Zel'dovich Array (SZA) – a $3.5\,\mathrm{m} \times 8$-element subset of the Combined Array for Research in Millimeter-wave Astronomy (CARMA) – was an optimal choice of instrument for such an experiment. This is due in part to the frequency coverage ($27 - 35\,\mathrm{GHz}$, covering CO(1-0) from $z = 2.3 - 3.3$), relatively large field of view ($140\,\mathrm{arcmin}^2$) and compact configuration of the SZA.

Starting in 2011, the SZA was used in an intensity mapping experiment focused on measuring the abundance and evolution of molecular gas in the era leading up to the peak of cosmic star formation. This project – known as the CO Power Spectrum Survey (COPSS) – made use of both archival data and new observations with the SZA. There were two primary goals for COPSS: placing the first-ever limits of the CO power spectrum at high redshift, and exploration of the astrophysical and systematic contaminants that might impede future efforts. With a total survey volume of more than 10 million cubic megaparsecs, it is one of the largest blind surveys to date targetting molecular gas emission at high redshift, more than an order of magnitude larger than similar efforts with ALMA, VLA, and PdBI.

At the conclusion of the project, COPSS yielded a tentative ($\sim 3\sigma$) detection of bulk CO emission, constraining the CO power spectrum to $P_{\mathrm{CO}} = 3.0 \pm 1.3 \times 10^3 \mu\mathrm{K}^2\ h^{-3}\,\mathrm{Mpc}^{-3}$ at $z \sim 3$. As shown in Fig. 13, these constraints excluded several theoretical models, and placed significant constraints on both the CO luminosity function and the cosmic molecular gas density at high redshift.

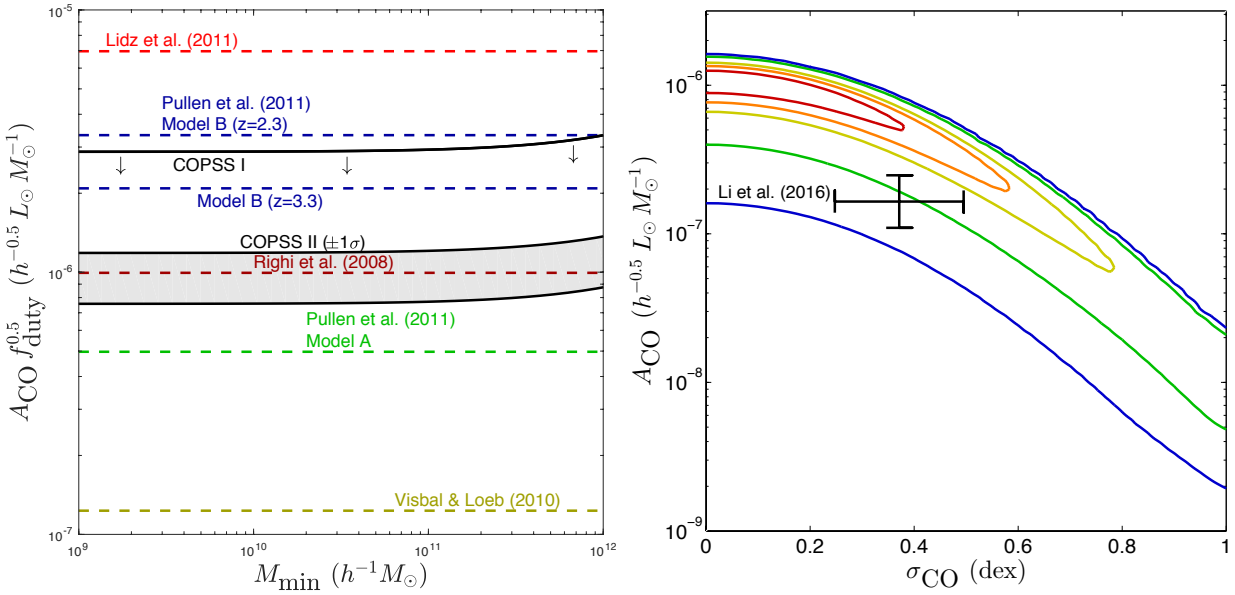

Figure 13. *Left: Constraints on A_{CO} versus minimum halo mass for CO emission (M_{min}, as derived from the COPSS experiment [97, 113]. These constraints are shown against the theoretical expectations from a number of models. Right: Constraints on A_{CO} versus the scatter in the halo mass to CO luminosity relationship (σ_{CO}), with the 95.4% confidence limits shown in blue. Also shown are theoretical estimates from Li et al. (2016). (Courtesy of Karto Keating)*

3.3 Tentative Detection of [CII] at Medium Redshifts

The CII line emission typically comprises 0.1–1% of the far-infrared luminosity in low-redshift galaxies, making it an ideal candidate for detection using cross-correlations. At redshifts $2 < z < 3.2$, the [CII] emission line appears in the 545 GHz Planck band; thus its intensity can be measured by cross-correlating the Planck map with $z \sim 2.5$ quasars. In Pullen et al. [114], the authors cross-correlate the 545 GHz Planck map with an overdensity map constructed from the SDSS BOSS DR12 quasar catalog (Pâris et al., in prep.). The 545 GHz map is dominated by dust emission from the Galaxy [115] and cosmic infrared background (CIB) emission from young stars [116]. The dust emission cancels out in the cross-correlation, though it contributes to the errors. The CIB emission correlates with the quasars, so the authors use cross-correlations with the 353 and 857 GHz maps from Planck, as well as cross-correlations between the Planck maps and CMASS galaxies from $z = 0.57$ [117–119] to perform a MCMC fit over all the cross-power spectra to estimate parameters in a CIB halo model [120]. This procedure breaks the degeneracy between the [CII] and CIB emission in the 545 GHz map to isolate the [CII] signal.

In Fig. 14 the constraint on the intensity of [CII] emission from Pullen et al. [114], $I_{CII} = 5.7^{+4.8}_{-4.2} \times 10^4$ Jy/sr (95% c.l.) is plotted, along with predictions from various models [4, 44, 121–123]. Comparing the likelihoods of the CIB & [CII] model and the CIB only model, the Bayesian Information Criteria, 96.5 and 96.0 respectively, are similar, implying that both interpretations are plausible and more data is needed to confirm the [CII] detection. The results favor the models where [CII] ions emit due to collisional excitations from electrons [121, 122] over the scaling relations constructed from luminosity function measurements, though none of the models are ruled out. Also shown in the figure are forecasts where the BOSS quasar

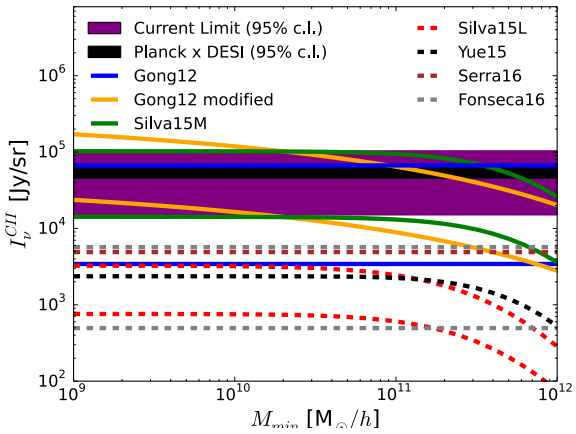

Figure 14. *Measurement of the [CII] intensity with 95% confidence limits. Also shown are the range of predictions for several [CII] intensity models, including collisional excitation models (solid lines) and scaling relations (dashed lines), as functions of minimum halo mass $M_{\rm min}$. The measurement favors the collisional excitation models which appear at the high end of the range of models, although no models are ruled out by 3σ. (Courtesy of Anthony Pullen)*

maps are replaced with quasars from the Dark Energy Spectroscopic Instrument (DESI) [124], finding that a similar method could yield a signal-to-noise ratio of 10 for the [CII] emission.

3.4 Cross-Correlation between Lyα Emission and Quasars

Flux from the Lyα line occurs in many environments, and is produced by many sources, including young stars, quasars and the ultraviolet background (see e.g., Pullen et al. [6]). Because of the high cross section for scattering of neutral hydrogen, much of this Lyα emission is expected to be extended, and intensity mapping techniques are therefore useful. As with other optical emission, intensity mapping with Lyα is affected by contamination from other lines, but also potentially instrumental and other systematic effects. Cross correlation with objects with known redshift such as galaxies, known Lyα emitters, quasars, the Lyα forest, metal and other absorption lines all offer in principle a route to measure an intensity mapping signal without contamination. One would like to take integral field spectra of as much of the sky as possible (e.g., HETDEX Hill et al. [43]). At present, the largest single dataset available is the Luminous Red Galaxy (LRG) sample from SDSS/BOSS (total fiber area of 0.4 sq. deg. for DR12). Croft et al. [125] made a first attempt at Lyα intensity mapping. The authors used BOSS spectra by subtracting the best fit LRG model and cross-correlating the residual flux with SDSS quasars.

During the Croft et al. [125] analysis it became evident that even when using cross-correlation techniques achieving robust measurements from line-intensity mapping data is complex. The low surface brightness of targeted IM flux means that light can leak into nearby spectral columns on a fiber-fed spectrograph CCD. The authors eliminated pairs of fibers separated by 5 columns or less because of this. The work of Croft et al. [125] should be seen as a trial of this kind of observational analysis, and a tentative first detection (see below). Insights for the future include the desirability of selecting cross-correlation centers from entirely different datasets from the intensity map, and also of tracking light scattering in the instrument.

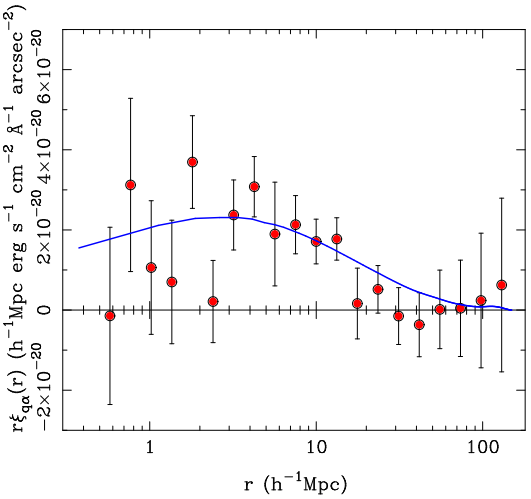

Figure 15. *The quasar-Lyα emission cross-correlation function from Croft et al. [125]. The points represent results from SDSS BOSS over the redshift range $z = 2 - 3.5$, with jackknife error bars. The smooth curve is a best fit linear CDM correlation function. (Courtesy of Rupert Croft)*

After eliminating all contaminants found, the Croft et al. [125] result was at face value an 8σ detection of Lyα emission with large-scale clustering ($1 - 15\ h^{-1}$Mpc) consistent with the CDM shape (see Figure 15). The amplitude (proportional to the mean Lyα surface brightness) was extremely high however, equivalent to thirty times the Lyα emission from previously known Lyα emitters (but consistent with extinction corrected SFR). The signal to noise in the cross-correlation is nonexistent beyond $15\ h^{-1}$Mpc, meaning that the measurement only comes from the $\sim 3\%$ of the volume closest to quasars. It is energetically possible that quasar HeII reionization or jet heating is responsible for the signal rather than star formation. In this case, most of volume of space (far from quasars) would have much lower Lyα surface brightness. This picture can be tested by cross-correlating with a more space-filling tracer (such as the Lyα forest). At time of writing a trial measurement of the Lyα forest-Lyα emission cross-correlation has not led to a detection. It therefore seems that likely that the Croft et al. [125] signal is local to quasars, or else due to unknown contamination. Current data is almost at the level required to detect a Lyα emission- Lyα forest cross-correlation signal from *known* Lyα emitters. Many firm detections therefore seem certain from upcoming larger datasets such as HETDEX Hill et al. [43], PAU [126], and J-PAS [127].

4

Experimental Landscape

As described in Section 1, low resolution maps of various emission lines have the potential to efficiently measure bulk properties of the Universe across the past 14 billion years of cosmic history. In this section, we describe current and upcoming instruments dedicated to intensity mapping of various lines in different redshift ranges for the purposes of probing the epoch of reionization, star formation, and large scale structure and dark energy. A table of these experiments and their salient parameters is given in Table 4-1.

Experiment	Line	Frequency	Redshift range	Location
HERA	HI	$50-250\,\mathrm{MHz}$	$5-27$	South Africa
SKA-LOW	HI	$50-350\,\mathrm{MHz}$	$3-7$	Australia
CCAT-prime	[CII]	$185-440\,\mathrm{GHz}$	$3.3-9.3$	Chile
TIME	[CII]	$200-300\,\mathrm{GHz}$	$5.3-8.5$	North America
CONCERTO	[CII]	$200-360\,\mathrm{GHz}$	$4.3-8.5$	Chile
COPSS	CO	$27-35\,\mathrm{GHz}$	$2.3-3.3$	North America
mmIME	CO, [CII]	$300, 100, 30\,\mathrm{GHz}$	$1-5$	various
AIM-CO	CO	$86-102\,\mathrm{GHz}$	$1.2-1.7$, $2.4-3.0$	China
COMAP	CO	$26-34\,\mathrm{GHz}$	$2.4-3.4$, $5.8-7.8$	North America
STARFIRE	[CII], NII	$714-1250\,\mathrm{GHz}$	$0.5-1.5$	Sub-orbit (balloon)
SPHEREx	Hα (Hβ, [OII], [OIII]), Lyα	$60-400\,\mathrm{THz}$	$0.1-5$, $5.2-8$	Space
CHIME	HI	$400-800\,\mathrm{MHz}$	$0.8-2.5$	North America
HIRAX	HI	$400-800\,\mathrm{MHz}$	$0.8-2.5$	South Africa
SKA-MID	HI	$350\,\mathrm{MHz}-14\,\mathrm{GHz}$	$0-3$	South Africa
BINGO	HI	$939-1238\,\mathrm{MHz}$	$0.13-0.48$	South America

Table 4-1. *Parameters for various intensity mapping instruments described below.*

4.1 Epoch of Reionization Science at z=5–27

A description of the science goals related to the Epoch of Reionization (EoR) was presented in Section 2, here we describe the current experiments dedicated to measuring this signal. Measurements from the CMB constrain the EOR to have occurred around $z_{re} \sim 9$, and so 21 cm experiments seeking to make a measurement with HI mapping build instrumentation at radio frequencies: $\sim 140\,\mathrm{MHz}$, while experiments targeting the dusty star-forming component with [CII] will target frequencies near 200 GHz.

OVRO-LWA

The Owens Valley Long Wavelength Array (OVRO-LWA) is a low-frequency interferometer located at the Owens Valley Radio Observatory (OVRO) near Big Pine, California. The array currently consists of 288 dual-polarization broadband dipole antennas operating between 27 MHz and 85 MHz. 251 antennas are located within a 200 m diameter core for surface brightness sensitivity, 32 antennas extend to longer baselines (up

to 1.5 km), and the remaining 5 antennas are equipped with noise-switched front end electronics for total power radiometry. The full array will eventually extend to 352 antennas and baselines of 2.5 km. The 5 total power antennas are used by the Large Aperture Experiment to Detect the Dark Age (LEDA) project to measure the sky-averaged signature of HI absorption from the Cosmic Dawn [128]. The LEDA project also provides a 512-input correlator with 58 MHz instantaneous bandwidth [129]. As well as the LEDA total power experiment, the OVRO-LWA will target the spatial power spectrum of 21-cm fluctuations from the Cosmic Dawn era.

The OVRO-LWA surveys the sky north of -30° at 10 arcmin resolution ($k_\perp < 0.3\,h\,\mathrm{Mpc}^{-1}$ at $z = 20$) with 24 kHz channelization ($k_\parallel < 10\,h\,\mathrm{Mpc}^{-1}$ at $z = 20$). The OVRO-LWA will place upper limits on the spatial power spectrum of 21-cm fluctuations between $30 > z > 16$. These fluctuations are primarily sourced by inhomogeneous star formation and heating of the early universe [130]. At 80 MHz, the foreground brightness temperature can be an order of magnitude larger than at 200 MHz. As a first step on the path to characterization of 21-cm fluctuations, the OVRO-LWA has been used to produce 8 foreground maps evenly spaced between 36.528 MHz and 73.152 MHz [131]. The OVRO-LWA also responds to LIGO and Swift triggers, monitors nearby stars for stellar flares and magnetospheric radio emission from exoplanets, as well as monitoring the radio emissions of the Sun and Jovian system.

HERA and its predecessors

The Hydrogen Epoch of Reionization Array (HERA; `http://reionization.org` [132]) is a dedicated radio interferometer optimized to deliver high signal-to-noise measurements of redshifted 21 cm HI emission to detect and characterize the EoR and Cosmic Dawn. Operating over the the frequency range $50 < \nu < 250$ MHz ($27 < z < 5$), HERA covers the period of the formation of the first stars and black holes ~ 0.1Gyr after the Big Bang ($z \sim 30$) past the full reionization of the intergalactic medium (IGM) ~ 1 Gyr later ($z \sim 6$). HERA will enable high precision measurement of the reionization history [53]; constraints on the physics of reionization [133]; cosmological constraints using combined 21 cm power spectrum and global signal measurements [47]; a robust statistical characterization of the reionization and X-ray heating power spectra [134]; and has the sensitivity to enable first images of large scale HI structure [135] and perform cross-correlation analyses with galaxy surveys [136, 137].

HERA is a second-generation instrument which combines efforts and lessons learned from the Murchison Widefield Array (MWA) and the Donald C. Backer Precision Array for Probing the Epoch of Reionization (PAPER), as well as the MIT EoR experiment (MITEoR) and the Experiment to Detect the Global EoR Step (EDGES). The HERA array, currently under construction with completion in late 2019, will be ~ 350 14-meter diameter non-tracking dishes. High surface brightness sensitivity and redundant calibration is achieved with a close-packed hexagonal array 300 m across [138], with imaging outriggers out to ~ 1 km . Its substantial collecting area provides an order of magnitude more sensitivity than first generation instruments. Careful electromagnetic simulation and measurement of the antenna, feed and electronics aim to control systematic effects due to spectral non-smoothness [139–142].

HERA is fully funded from the NSF Mid-Scale Instrumentation Program and the Betty and Gordon Moore Foundation, and is currently commissioning the first 37 antennas.

Figure 16. *Left: Rendering of the 320-element core of the full HERA-350 array. Right: Picture of 19 HERA 14 m, zenith-pointing dishes (with PAPER elements in the background) currently deployed in South Africa. (Courtesy of James Aguirre)*

SKA-LOW

The Square Kilometre Array (SKA) is a large, international, general-purpose radio telescope facility, split between two sites in the Karoo desert in the Western Cape region of South Africa, and the Murchison region in Western Australia. Three pathfinder telescopes (ASKAP, KAT7, and MeerKAT) have already been constructed on these sites, with initial construction of Phase 1 of the array (SKA1) slated to begin around 2018, and an early science phase expected in 2020. This will be followed by full operations starting around 2023, and an eventual upgrade to SKA2 (with 10× the projected sensitivity of SKA1) to begin operations around 2030.

The Phase 1 design incorporates two sub-arrays. The first, SKA1-LOW, is a low frequency array consisting of ~ 500 stations of 256 dipole antennas each, covering the band from $50 - 350$ MHz, and will be constructed on the Australian site. The primary science goal of LOW is to study the EoR using intensity maps of the 21cm line, in particular by the direct imaging of ionization bubbles (seen in negative against the neutral hydrogen emission) over angular scales of arcminute to degrees [143]. This adds imaging capabilities that are not possible with earlier-generation EoR experiments aiming for a statistical detection of the 21cm power spectrum at the relevant redshifts. The sheer number of receivers, coupled with an advanced beamforming capability, will make SKA1-LOW an extremely sensitive and flexible intensity mapping experiment.

CCAT-prime

CCAT-prime (CCAT-p) will be a 6 meter aperture telescope located at 5600 meter site on Cerro Chajnantor in the Atacama Desert in northern Chile. The CCAT-p design strives to optimize surface brightness sensitivity and mapping speed through the telluric windows at wavelengths from 200 μm to 3.3 mm. The instantaneous field of view (FoV) is maximized through the use of a crossed-Dragone optical arrangement where an off-axis concave primary delivers the beam to an off-axis and concave secondary which forms a flat focal plane with a FoV of $\sim 2°$, $4°$, and $8°$ diameter at 350 μm, 1.1 mm, and 3.3 mm wavelength respectively. The unobscured optical path with minimized telescope panel spacing minimizes both emissivity and the effects of low-level optical side-lobes. The total wave-front error requirement is $< 11\,\mu m$ rms ($7\,\mu m$ goal) so that CCAT-p operates very efficiently in the short submillimeter bands. CCAT-p will be located at 5600 meter elevation on Cerro Chajnantor—about 500 m above the nearby ALMA array and APEX telescopes in

northern Chile where the water vapor is sufficiently low to enable routine operation in the 350 μm window, frequent operations in the 200 μm telluric window, and improved performance in the longer wavelengths.

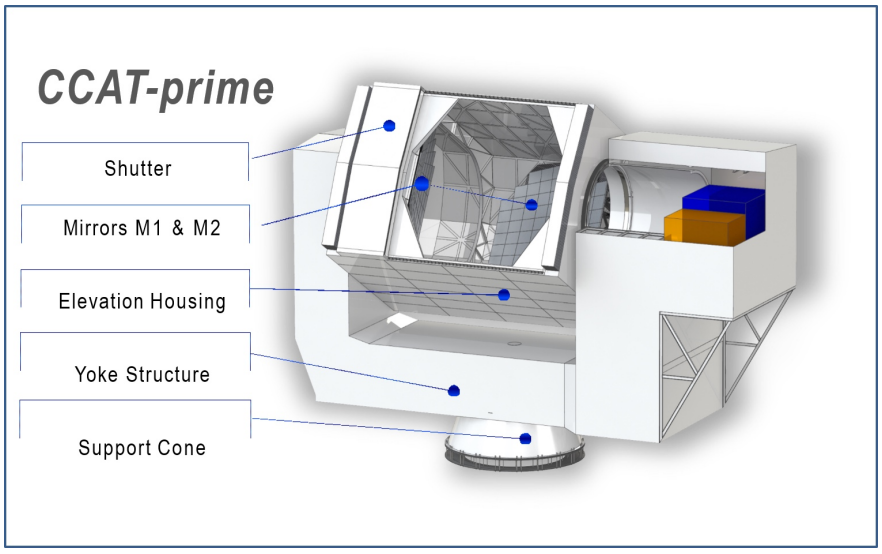

Figure 17. *The CCAT-prime design from Vertex Antennentechnik, GmbH. (Courtesy of Gordon Stacey)*

CCAT-p offers an excellent platform from which to pursue LIM science, particularly in the [CII] 158 μm line at redshifts from roughly $5 < z < 9$. At these redshifts [CII] IM traces out the process of reionization and, quite fortunately, the signal is transmitted through the very clean 190 to 315 GHz portion of the mm-wave telluric transmission spectrum. The expected aggregate clustering signal size-scale is of the order $1 - 2$ arcmin, which is a very good match to the CCAT-p diffraction limited beam ($\sim$ 64 to 40 arcsec at 190 to 300 GHz). The intensity mapping signal needs to be mapped at spectral resolving powers $\sim$ 500 km/s over approximately 16 square degree region to noise levels below 8×10^{-14} W/m^2/sr (cf. Gong et al. [2]). These sort of noise levels over such a broad field require large numbers of mm-wave bolometer pixels which can be employed within spectrometers that either spatially, or spectrally multiplex. For CCAT-p a spatially multiplexing spectrometer is planned based on a wide-field Fabry-Perot Interferometer. This system should be able to deliver the requisite sensitivity with an imaging array of $\sim$ 4000 pixels in about 4000 hours of integration time. These array formats are well within the capabilities of today's TES bolometer technology.

CCAT-p is being constructed under the original CCAT framework, and is a partnership of Cornell University, the Universities of Bonn and Cologne, and CATC, a consortium of Canadian academic institutions. CCAT-p is funded for construction and will begin detailed design in July 2017. First light is anticipated in June 2021.

TIME

The TIME (Tomographic Ionized-carbon Mapping Experiment [3]) is a novel high-throughput millimeter-wave imaging spectrometer array designed to make pioneering measurements of the redshifted 157.7 μm line of singly ionized carbon from the EoR at $5.3 < z < 8.5$. [CII] is the most energetic emission line in galaxies at wavelengths longer than 40 μm and is a bolometric tracer of total star-formation. TIME will also produce high significance measurements of the molecular gas density through the epoch of peak start formation via detections of CO clustering fluctuations in multiple rotations transitions from redshifts $0.5 < z < 2$. Finally

TIME will measure the kinetic Sunyaev-Zeldovich effect in galaxy clusters, using spectral subtraction of atmospheric noise to improve mapping speed by a factor of ~ 5 over previous surveys.

TIME uses a linear array of 32 two-dimensional waveguide spectrometers with a spectral resolving power of ~ 100, a lower resolution version of the spectrometer technology first developed for the Z-SPEC instrument. The spectrometers are arranged in two stacks of 16, covering the frequency range of $183-326$ GHz, and view the sky in two polarizations off a beam splitter to maximize sensitivity. Arrays of sensitive TES bolometers, read out by time-domain SQUID amplifiers, detect light from the spectrometers. TIME couples to the telescope using relay optics that form an image of the primary mirror inside the cryostat, and a 4K cold stop to reduce stray light. As shown in Fig. 18, much of the cryogenic hardware for the instrument has already been assembled. First versions of the spectrometers, feeds and detectors have all been prototyped, and 300 nights of winter observing time on the APA 12-m telescope is secured for TIME observations. TIME will carry out its first CII survey starting in late 2018.

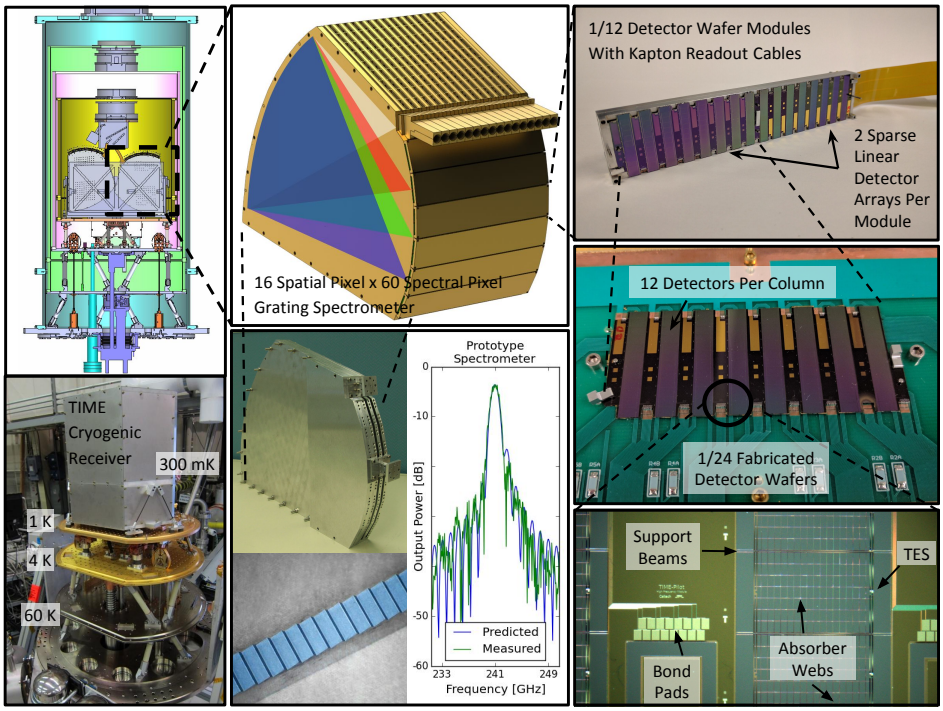

Figure 18. *TIME instrument overview. The instrument is housed in an existing closed-cycle 4K-1K-300mK cryostat (bottom left) with a large cryogenic volume for the spectrometer stacks and optics (top left). 32 waveguide grating spectrometers (top center) are assembled into two stacks of 16; they couple the same 1-D linear field on the sky via an array of feedhorns and single-polarization waveguide feeds illuminated through a polarizing grid. Each grating spectrometer is similar to that used in Z-SPEC, but at lower resolving power. The dispersed light is detected with twelve 2-D arrays of TES bolometers which span the spectrometer stacks (right) with a total of 1920 detectors. The TES detectors (lower right) are similar to those built at JPL but with mesh absorbers. A linear array of 11 150 GHz broadband channels view the same sky as the spectrometers via a dichroic filter, and will be used in surveys of the kSZ effect. Prototype TIME gratings in a "mini-stack", a shortened version of one of the TIME spectrometer stacks, have been produced (bottom center). Each grating has 190 facets and provides resolving power in excess of 150 over the full $183-326$ GHz range. Their spectral profiles have been measured using a coherent source and diode detector (bottom center). (Courtesy of Abby Crites and Jamie Bock)*

TIME targets a first detection of the [CII] signal (in both the clustering and Poisson regimes), spanning the spatial scales corresponding to $0.1 < k\,[\mathrm{h/Mpc}] < 1$. TIME uses a linear survey strategy to maximize sensitivity on large scales, with a survey area of $0.3' \times 1\,\mathrm{deg}$, or a comoving volume of $2 \times 10^5\,(\mathrm{Mpc/h})^3$. TIME uses spectral information to remove atmospheric fluctuations on large scales, a method previously demonstrated by observations with Z-SPEC. While forecasts for the [CII] power spectrum vary between models, as shown in Fig. 19, TIME is able to detect [CII] clustering fluctuations in a 1000 hour survey on the APA 12-m telescope at $S/N \geq 10$ at $z = 6 - 7$. The [CII] luminosity functions associated with these models are consistent with recent ALMA measurements of [CII] in galaxies at $z = 6 - 7$. A first detection of [CII] clustering fluctuations would constrain the total star formation rate during the epoch of reionization, while detection of Poisson power would constrain the integrated [CII] luminosity function, and set up the case for a new generation of [CII] mapping measurements with higher sensitivity.

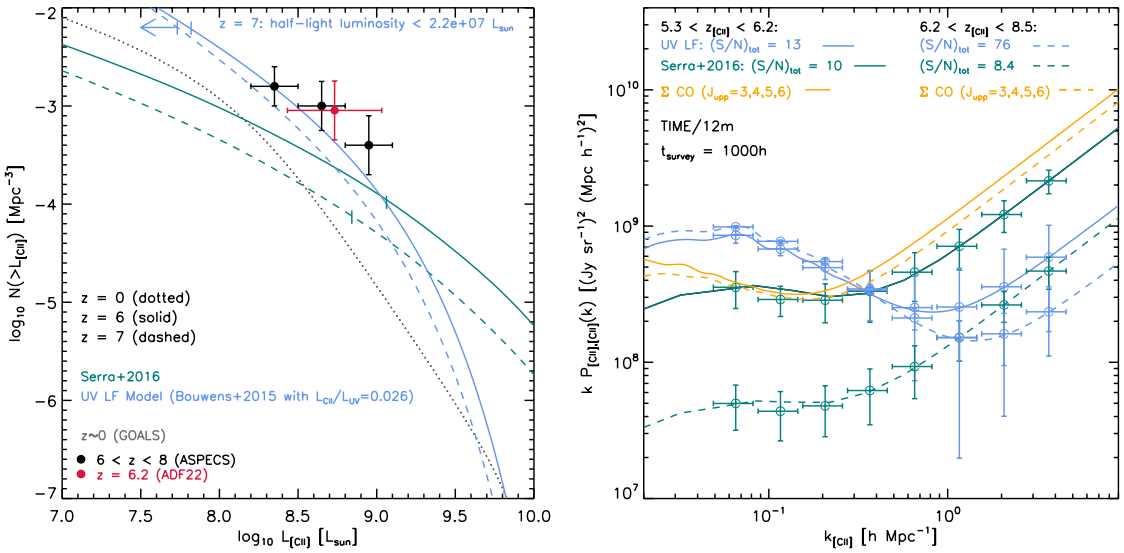

Figure 19. *Left: [CII] luminosity function models for EoR, plotted as cumulative number counts per* Mpc^3*. The Serra et al. [123] model is shown in teal for* $z = 6$ *(solid) and* $z = 7$ *(dashed). Blue curves show the UV LF model based on the high-z UV luminosity function measured by HST and recent [CII] systems detected by ALMA. Vertical ticks indicate the depth in* $L_{[\mathrm{CII}]}$ *that recovers half of the total [CII] intensity (much fainter for the UV LFs; at* $z = 7$ *UV LF, the half-[CII] light depth is unconstrained). Data with error bars (not including cosmic variance) are shown for results from ALMA deep field experiments ASPECS (Aravena et al. [144]) and ADF22 (Hayatsu et al. [145]). (While Aravena et al. [144] have corrected their data for incompleteness and false detections, the [CII] detections have yet to be spectroscopically confirmed.) For reference, the* $z \sim 0$ *[CII] number counts are shown in dotted dark gray, as measured for local luminous infrared galaxies (Hemmati et al. [146]). Right: 3-D power spectra (in* $kP(k)$ *units) of EoR [CII] per the UV LF and Serra et al. [123] models at left. Two redshift ranges are shown. Orange curves show the signal from low-redshift CO fluctuations, when cast into the [CII] comoving frame. (Courtesy of Jamie Bock)*

TIME will also make high signal to noise detections of CO rotational line emission at lower redshifts. These can be used to estimate the density of molecular gas that fuels star formation, as shown in Fig. 20. The CO detections are shown assuming spectral cross-correlations between rotational levels, which are more robust against sources of systematic errors compared with auto-correlations. The CO emitting galaxies must be removed from the [CII] signal, and two methods have been developed to surmount this problem, either using

the strong anisotropy of the CO power spectrum in co-moving [CII] coordinates or masking the CO galaxies spectrally and spatially using an external catalogue, noting that modestly over-masking galaxies does not substantially degrade the [CII] signal (see more description of these techniques in Section 5).

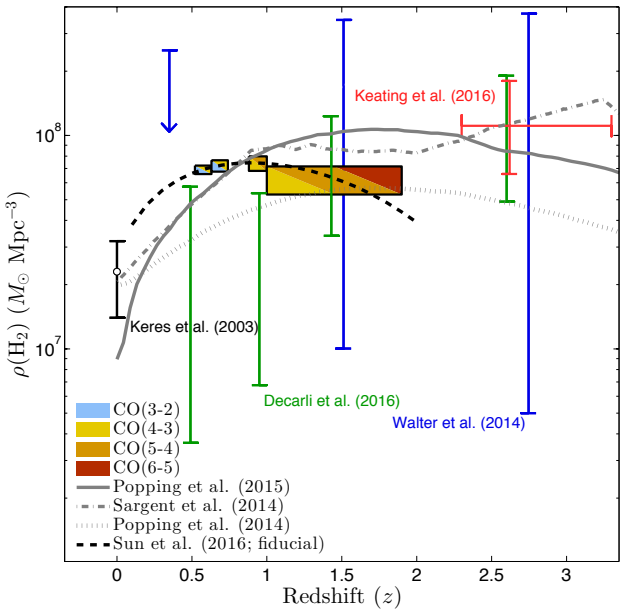

Figure 20. *Current theoretical predictions of the evolution of H2 density from several groups are shown, as well as the state of current measurements. The constraints from TIME are shown as boxes, colored by the pair of CO transitions that will be cross-correlated within the data to uniquely identify power at each redshift. The TIME measurement is subject to systematic uncertainty in the conversion of CO to H2, though this uncertainty applies almost identically to all of the measurements shown. Outside of a small gap around $z \sim 0.75$, TIME will chart the evolution in H2 density across 5 Gyr of cosmic time, starting from the period of peak star formation activity when depletion of molecular gas may have led to the subsequent rapid decline in the cosmic star formation rate density. (Courtesy of Jamie Bock)*

CONCERTO

CONCERTO proposes to measure [CII] at redshifts $4.5 < z < 8.5$ and CO intensity fluctuations arising from $0.3 < z < 2$ galaxies. The CONCERTO instrument will use Kinetic Inductance Detectors (KID; [147, 148]) following the successful development of the NIKA2 camera [149]. CONCERTO is planned to be deployed to the APEX telescope, which is a 12-m antenna located at a 5105 m altitude on the Llano de Chajnantor in Northern Chile. The instrument is based on a dilution cryostat, not requiring liquid helium or nitrogen, and able to assure continuous operation, i.e. no recycling or other dead time. The field of view is exceeding 100 arcmin^2. Spectra are obtained using a Martin-Puplett Fourier-transform spectrometer with variable resolution (settable from 1 GHz to 5 GHz) located at room temperature in front of the cryostat. Such a fast (compared to the atmospheric noise) spectrometer can now be used to get the spectra thanks to the very small time constants (< 0.1 msec) of KIDS. Each of the ~ 3000 pixels will acquire fast interferograms and will be able to extract a spectrum in $0.2 - 2$ second integration time. Typically, faster acquisitions relate to spectral resolution $R = \nu/\delta\nu \sim 100$, slower ones apply to $R \sim 300$. CONCERTO will produce, roughly once per second, a data cube containing the spectral image. The projections for the sensitivity and signal-to-noise ratios are shown in Fig. 21.

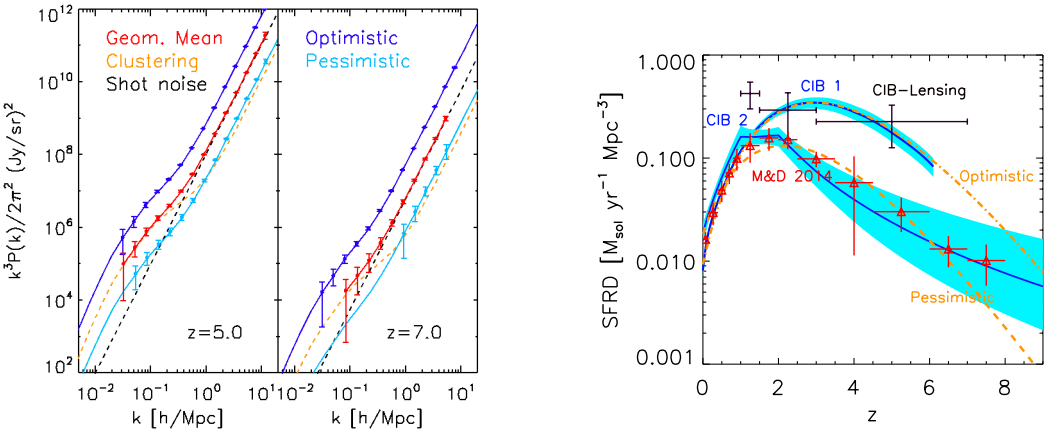

Figure 21. *Left: Predicted [CII] power spectrum (for three scenarios: optimistic, pessimistic and the geometrical mean) at redshifts $z = 5$ and $z = 7$. For the geometrical mean, both the clustering and shot-noise terms are shown. Error bars have been computed using the spectrometer and survey characteristics of the CONCERTO experiment. Only points with $S/N > 1$ are shown. Right: Figure illustrating how different the SFRDs derived from galaxies (red points, which come exclusively from UV-selected galaxies Madau and Dickinson [91]) and CIB anisotropies are. Different models of CIB anisotropies, that fit equally well the measured power spectra, give very different SFRD (cf CIB1 and CIB2 models: dark blue curves and 1σ in light blue). Also shown are the measurements derived from the cross-correlation between the lensing map of the CMB and the CIB (black points, Ade et al. [150]). SFRD derived from the two [CII] models that are considered in the right panel (optimistic and pessimistic cases) are shown in orange. At $z > 5$, SFRD from the dusty star-formation is an "incognitus mundus". (Courtesy of Guilaine Lagache)*

To remove the CO contamination to the [CII] signal, CONCERTO will use the same methods mentioned for TIME and described in more detail in Section 5. But its wide frequency range will also permit to mitigate the CO contamination using the cross-correlation of multiple CO lines detected at each redshift [151]: between two and four CO lines are simultaneously observed at the same redshift for all $z > 0.35$. This method is being successfully tested using realistic sky simulations (with [CII] and CO line emissions added to the SIDES simulations of Bethermin et al. [152], as shown in Fig. 22).

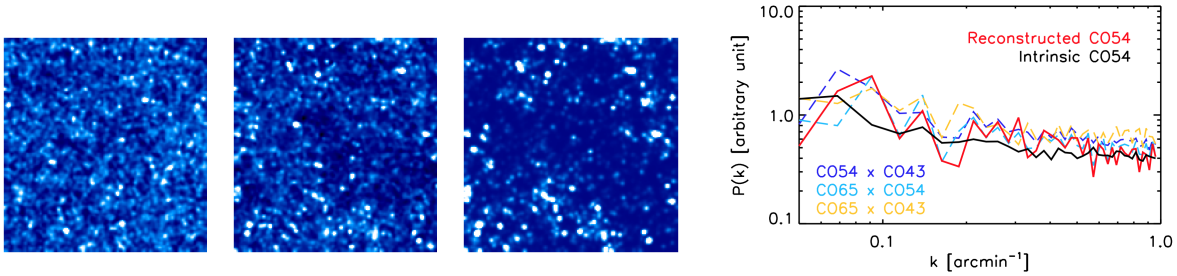

Figure 22. *First three images: our 1.4×1.4 deg^2 simulated sky maps at $z = 5.5 \pm 0.1$. From left to right: total signal, CO+[CII] only, [CII] only. The display range has been adapted for each image (the standard deviation of the [CII] map being 30 times lower than that of the total signal map). Right figure: first comparison of the intrinsic and reconstructed CO(5-4) power spectrum at $z = [1.1 - 1.2]$ (a foreground for [CII] at $z = 6$). It has been estimated using cross-correlations of CONCERTO maps at the frequencies of the CO(4-3), CO(5-4) and CO(6-5) lines. (Courtesy of Guilaine Lagache)*

4.2 Galaxy Assembly and Star Formation at z=2–10

There are two primary lines targeted by intensity mapping experiments to explore star formation science: CO and [CII]. Experiments targeting the rotational transitions of carbon monoxide are divided into two primary classes: interferometric and single-dish with focal plane arrays. Interferometric experiments provide better control of systematics and make measurements directly in the Fourier regime. Fields of view, however, tend to be small putting these experiments primarily in the shot-noise regime. Single-dish focal plane array experiments, on the other hand, can map large areas efficiently, pushing sensitivity into the clustering regime where cross-correlation with other large-area intensity mapping experiments can be performed. Systematic errors, in particular bandpass ripples, may prove challenging to remove or calibrate. It is important to note that some of the instruments described in the previous subsection, such as TIME and CONCERTO, are also very much relevant to the study of star formation science.

COPSS and mmIME

COPSS I and II – The COPSS I and II surveys are two interferometric experiments carried out using the Sunyaev-Zeldovich Array (SZA; [97, 113]). The SZA is an array of 8 3.5-m diameter antennas located in Southern California with receivers at 1 cm wavelength (27 – 35 GHz). The 1 cm receivers are sensitive to the J=1-0 transition from $2.3 < z < 3.3$ over k-modes from 0.5 to 10.0 $\mathrm{h\,Mpc^{-1}}$. The array is primarily configured in a compact configuration with minimum baselines of 4.5 m. COPSS I consisted of an analysis of archival data from 44 fields, each observed for approximately 20 hours. COPSS II consisted of new observations of 22 fields for a total of nearly 3000 hours on the sky. Fields include GOODS-N and other deep fields with extensive optical spectroscopy, which are suitable for cross-correlation. Both experiments demonstrated the ability to detect and remove foregrounds through Fourier filtering as well as handle systematic errors.

As described in the Chapter on First Detections, COPSS II detected a power $3.1^{+1.2}_{-1.3} \times 10^3\,\mu\mathrm{K}^2\,(\mathrm{h^{-1}\,Mpc})^3$, which is non-zero at 99.2% confidence, setting significant limits on the CO luminosity function and H_2 mass density.

Millimeter Intensity Mapping Experiment (mmIME) – Motivated in part by the success of COPSS, and in advance of new instruments dedicated to intensity mapping experiments, a new intensity mapping-focused experiment was started in 2016, utilizing existing radio instruments. This new experiment, referred to as mmIME, will focus on the multiplicity of bright transitions found in the cold gas of high redshift galaxies at millimeter wavelengths. The goal of these new observations is three-fold: confirm the tentative detection from COPSS, expand the redshift range beyond $z \sim 3$, and explore other spectral lines (i.e.; higher-order rotational transitions of CO, [CII]).

mmIME will seek to utilize both archival data and new observations, leveraging the combined power of the VLA, the Atacama Compact Array (ACA), and SMA at 1 cm, 3 mm, and 1 mm respectively. mmIME will take advantage of the fact that all three instruments have similar primary beam sizes and sensitivity to similar spatial modes to cross-correlate measurements between these three instruments, separating the different line/redshift components at a given frequency to allow for the exploration of multiple line species over a broad redshift range ($z \sim 1{-}5$).

As of mid-2017, pilot studies utilizing VLA, ALMA, and SMA are underway, and projections from this pilot survey are given in Figure 23 and show an improvement in the existing constraints on the CO power spectrum by approximately an order of magnitude, surveying an area approximately $10\square^\circ$ in size and covering approximately an octave in frequency between 1 cm and 1 mm.

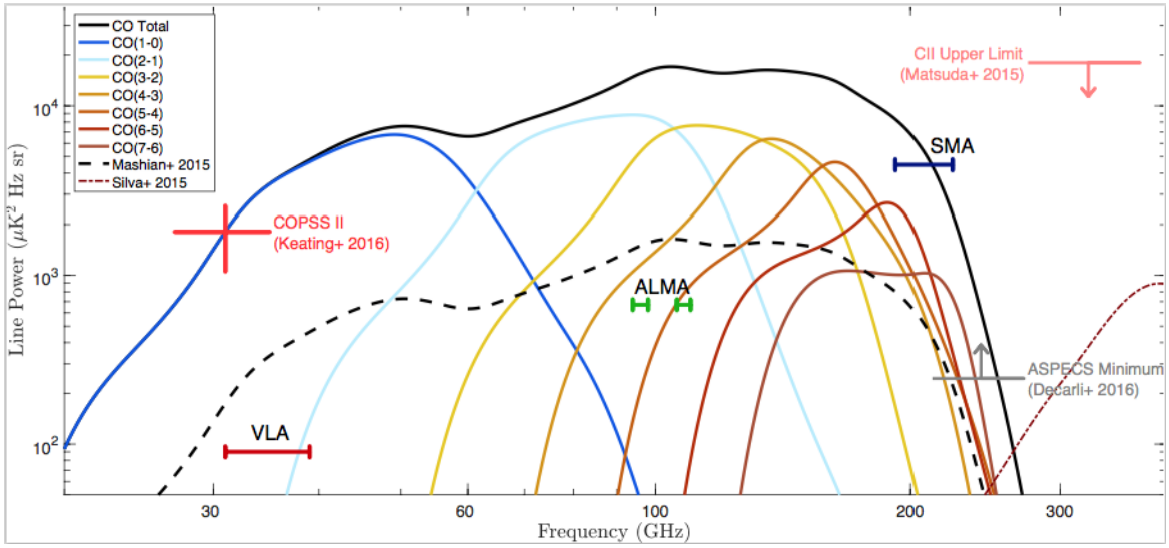

Figure 23. *Theoretical expectations for the line power of various transitions, versus the estimated sensitivity of the pilot survey of mmIME. The fiducial model takes estimates from Mashian et al. [12], scaled to match the power measured in COPSS. Also shown are the upper and lower limits set by blind 1mm surveys with ALMA [153]. Additionally shown are estimates on the line power from [CII] from Silva et al. [122], although recent results from ASPECS suggests at there may be more than 10 times more power than what is estimated. The full mmIME survey is expected to have improved sensitivity by factor of* ~ 3*, with significantly greater spectral coverage between 30 GHz and 300 GHz. (Courtesy of Karto Keating)*

AIM-CO

ASIAA Intensity Mapping for CO (AIM-CO) is an interferometric experiment using the Yuan-Tseh Lee Array (YTLA; Bower et al. [154]). Located on Mauna Loa, the YTLA is an array of 13 1.2-m dishes on a hexagonal close-packed array with a minimum spacing between antennas of 1.4 m. Each dish has a 3 mm receiver sensitive from 86–102 GHz. A dual polarization 7-element correlator was delivered in 2017 with an instananeous bandwidth of 4 GHz with 4096 spectral channels. The interferometric nature of the experiment was chosen in order to provide maximum control of telescope and foreground systematics and produce reliable detection of the expected signal. AIM-CO is sensitive to the J=3-2 transition from $2.4 < z < 3.0$ and $J = 2 - 1$ from $1.2 < z < 1.5$ over k-modes from 0.5 to 3 hMpc^{-1}

Following commissioning in 2017, a two-year observational campaign is planned. The observing campaign will match survey fields observed as part of with the COPSS SZA observations experiment [97, 113] to enable cross-correlations at (both radio and optical wavelengths). Cross-correlations are critical for validation of the auto-correlation signal, disambiguation of different transients, and extraction of host galaxy-dependent effects. The AIM-CO experiment will be a factor of 10 more sensitive than COPSS II, providing an opportunity to confirm the COPSS II detection and probe evolution of the CO power with redshift.

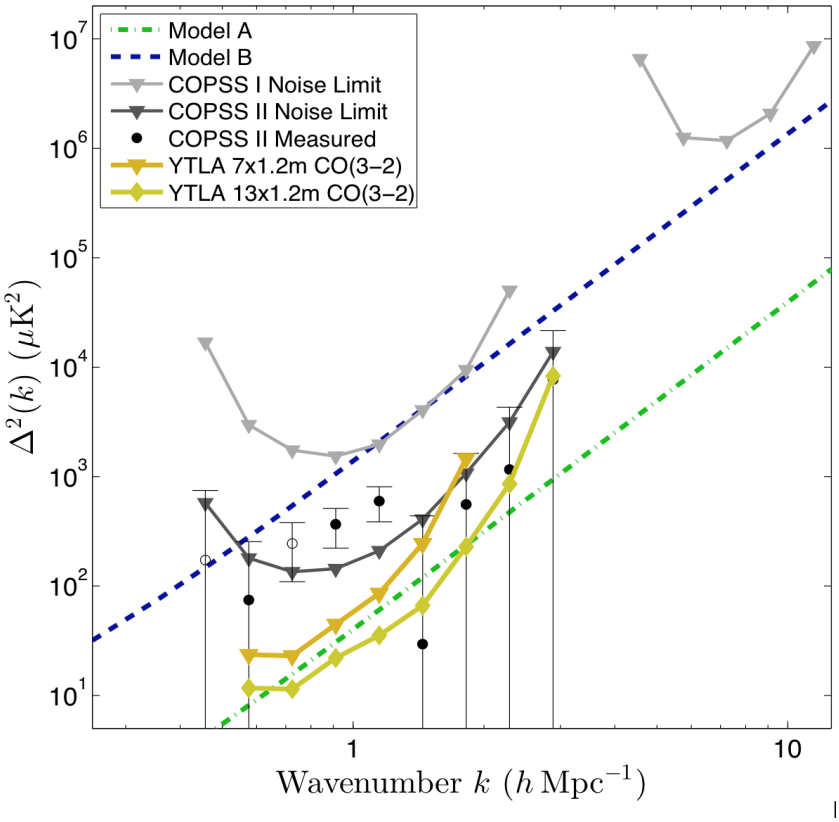

Figure 24. *AIM-CO sensitivity compared against COPSS I and II measurements and theoretical models from Pullen et al. [11]. (Courtesy of Geoff Bower)*

COMAP

The CO Mapping Array Pathfinder (COMAP; [155]) is part of a program aiming to trace the distribution of star-forming galaxies at the Epoch of Reionization (EoR). Constraining the CO power spectrum from the EoR will ultimately require measurements at multiple frequencies and focal-plane arrays with hundreds of elements. As a first step towards this goal, Phase I of COMAP comprises a 10.4-m telescope, located at the Owens Valley Radio Observatory (OVRO), equipped with a 19-pixel spectrometer array that will map a total of 10 square degrees of sky in the frequency range 26–34 GHz, with spectral resolution R 800. This band will be sensitive to CO(1-0) in the redshift slice $z = 2.4 - 3.4$ and to CO(2-1) in the redshift slice $z = 5.8 - 7.8$. A CASPER-based digital backend will process 8 GHz from each of the 19 pixels.

The aim of this pathfinder experiment is to i) demonstrate the feasibility and future potential of wide-field CO intensity mapping, and ii) provide a test-bed for the technology development and observational strategies. Phase I of COMAP will focus on constraining the CO power spectrum from the Epoch of Galaxy Assembly, at $z = 2.4 - 3.4$.

The receiver and digital backend are currently under construction, with a two-year observing campaign due to begin in 2018. The COMAP collaboration includes Caltech, JPL, Stanford University, University of Maryland, University of Miami, University of Manchester, University of Oslo and ETH, Zurich. Phase I of

the project is fully funded by NSF (AAG and MRI awards), the Keck Institute for Space Studies as well as contributions from institutional partners.

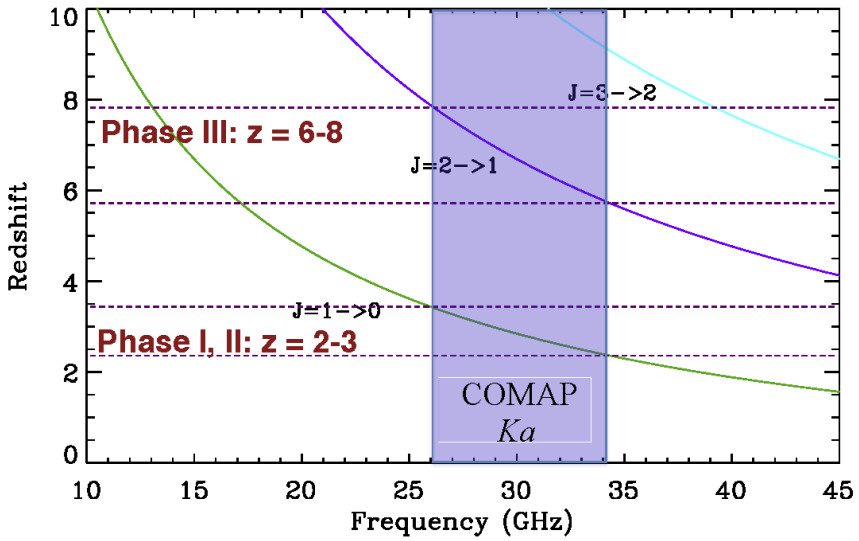

Figure 25. *The COMAP experiment [155]. (Courtesy of Kieran Cleary)*

STARFIRE

The Spectroscopic Terahertz Airborne Receiver for Far-InfraRed Exploration (STARFIRE) is an integral-field spectrometer using kinetic inductance detectors, operating from 240 - 420 μm and coupled to a 2.5 meter low-emissivity carbon-fiber balloon-borne telescope. Using dispersive spectroscopy and the stratospheric platform, STARFIRE can achieve better performance than SOFIA or Herschel-SPIRE FTS. STARFIRE is designed to study the ISM of galaxies from $0.5 < z < 1.5$, primarily in the [CII] (158 μm) line, and also in cross-correlation with NII (122 μm). This offers a view of the star-forming medium with minimal impact from dust extinction through the period of peak cosmic star formation and into the current epoch where the star formation begins to decline. STARFIRE will be capable of making a high significance of the [CII] power spectrum in at least 4 redshift bins and measuring the [CII] $\times$NII power spectrum at $z \sim 1$. The intensity mapped power spectra will be sensitive to the one- and two-halo clustering, as well as the shot noise, and will relate the mean [CII] intensity as a function of redshift (a proxy for star-formation rate density) to the large scale structure [156]. In addition, STARFIRE will measure $\sim$ 50 individual redshifts, but will also be able to stack on optical galaxies below the SPIRE confusion limit to measure the [CII] luminosity of more typical galaxies. Detector development for STARFIRE is currently funded by NASA [157].

Far-IR Spectrometers

Far-infrared spectroscopy is uniquely well-suited to study the inner workings of galaxies throughout cosmic history. The suite of rest-frame mid- and far-IR fine-structure transitions of elements such as carbon, oxygen,

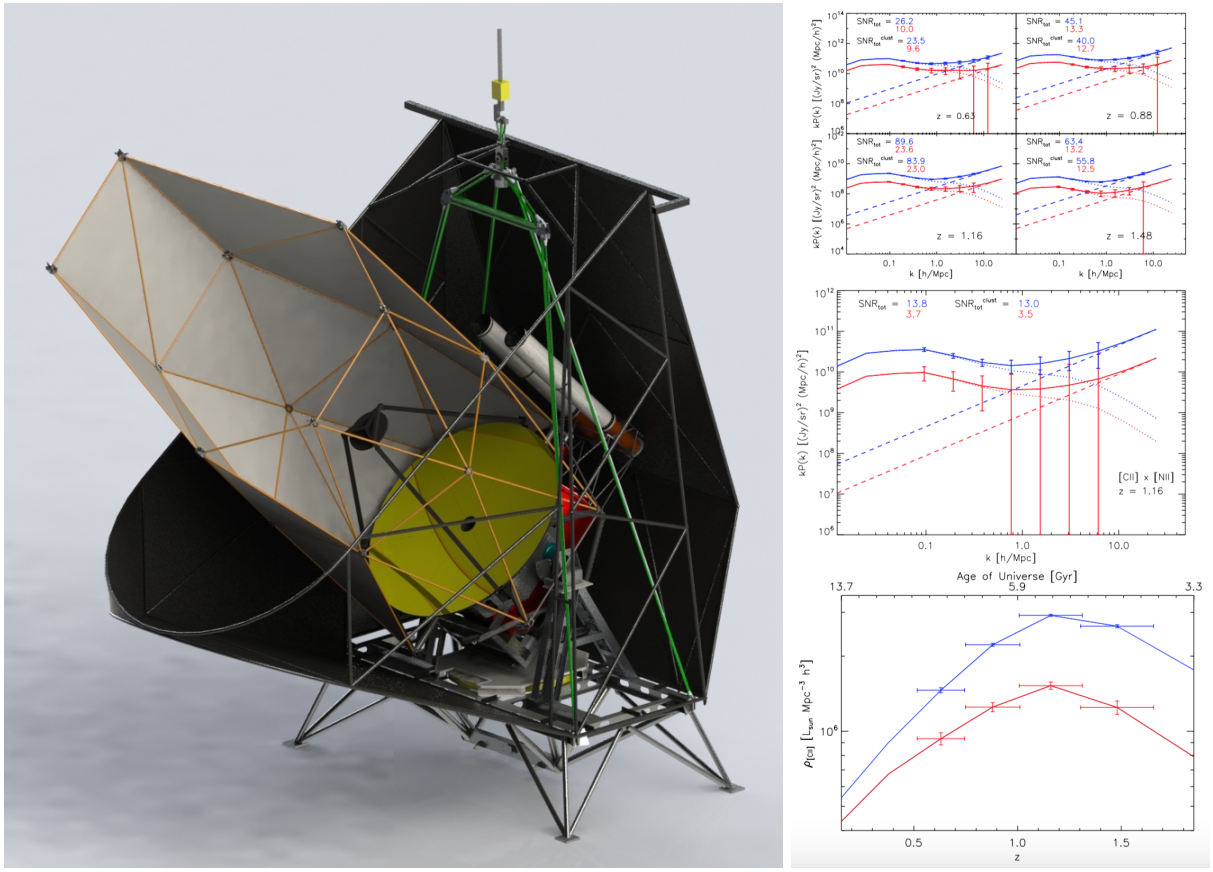

Figure 26. *Left:* STARFIRE *telescope and gondola in a cutaway view.* STARFIRE *will re-use the design for the gondola, cryostat, readout electronics, and star camera design from BLAST-TNG. Right: Top panel: Predicted total autocorrelation power spectra for the [CII] line at four redshifts. Solid curves are the total power, dotted lines show the sum of the 1- and 2-halo clustering terms, and dashed lines show the "shot noise" or Poisson term due to the discrete nature of galaxies. Error bars are for a survey of 100 hours in 0.1 deg*^{2}*. Power spectrum amplitudes were predicted using the same method described in Uzgil et al. [156], except for an updated IR luminosity function [158]. Also used, in addition to the Spinoglio et al. [159] [CII]-IR relation (red curve) used in Uzgil et al. [156], which under-predicts [CII] luminosities in high-redshift sources appropriate for this study, is a constant [CII]-IR relation of* $L_{[\mathrm{CII}]}/L_{\mathrm{FIR}} = 3 \times 10^{-3}$ *(blue curve). The two cases likely to bound the actual [CII] power spectrum are considered, and the actual sensitivity (expressed in terms of the signal-to-noise ratio, SNR) is expected to lie between the red and blue power spectra. Middle: Predicted [CII]-[*NII*]122μm cross-power spectrum at* $z = 1.16$*. Color-coding and linestyles are the same as in the top panel. A detection is possible even in the pessimistic case. Bottom: [CII] luminosity density as a function of redshift. Red and blue curves refer to the same respective [CII]-IR relations used in previous panels. The error bars in z represent the redshift coverage for each* STARFIRE *band. A high-significance measurement of the evolution of [CII] luminosity is possible with* STARFIRE*. (Courtesy of James Aguirre)*

nitrogen, neon and iron in their various ionization states tracks total star formation activity, encodes the stellar and interstellar properties, and provides a census of heavy element contents, all without uncertainties due to dust obscuration. Importantly, 3-D intensity mapping targeting the brightest of these lines naturally overcomes source confusion to provide built-in look-back-time encoding, a key aspect for isolating the faint signals form the early universe from the much brighter 'foregrounds'. To date, sensitive far-IR capability has

remained unrealized due to the technical challenges: it requires a cryogenic telescope above the atmosphere, combined with sensitive detector array technology that must be built by the astrophysics / cosmology community. However, large-format far-IR detectors have progressed greatly recently, and NASA, ESA, and JAXA are studying options for cryogenic far-IR space missions featuring wideband spectroscopy which could begin in the next decade.

The exquisite surface brightness sensitivity of these facilities will make them excellent platforms for line intensity mapping in the far-IR (here taken to be 30 microns to 600 microns). Initial 3-D power spectrum uncertainty estimates [123, 151, 156] based on expected instrument sensitivities for space-borne far-IR spectrometers (e.g. [160, 161]) indicate promise. Clustering in the bright lines (both auto- and cross spectra) is readily detectable even at the epoch of reionzation with the ambitious space concepts. These clustering signals constrain the total luminosity function integral in these lines, as well as their luminosity-averaged ratios, charting the total star formation history and probing the evolution of aggregate galaxy properties through cosmic time.

SPHEREx

The Spectro-Photometer for the History of the Universe, Epoch of Reionization, and Ices Explorer (SPHEREx) is a NASA MIDEX-class mission currently undergoing Phase A study. SPHEREx is designed to conduct the first full sky spectrometric surveys in the near-infrared and will operate with $R \sim 42$ between 0.75 and 4.18 microns and $R \sim 135$ between 4.18 microns and 5 microns. It will perform 4 all-sky surveys over the course of a 2-year mission. SPHEREx will chart the origin and history of galaxy formation through a deep survey centered near the ecliptic poles, allowing tomographic intensity mapping of large-scale structure at a complete set of near IR wavelengths. The deep spectro-imaging survey produces the ideal data set for full tomographic mapping of large-scale structure with $dz \sim 0.2$ resolution in the intensity mapping regime and higher when resolving individual sources. It will probe the inflationary history of the universe, the evolution of galaxies since the epoch of reionization, the origin of water in planetary systems, as well as creating a high-legacy spectral catalog over the entire sky [16]. At low redshifts SPHEREx will detect multiple lines with SNR > 10, the dominant lines being H_α for redshifts $0.1 < z < 5$, Hβ for redshifts $0.5 < z < 2$, and [OIII] for redshifts $0.5 < z < 3$. At high redshifts $5.2 < z < 8$, SPHEREx accesses the Ly_α line, providing a crucial probe of the formation and evolution of EOR galaxies [5, 6]. Measurement of Hα clustering measures cosmic star-formation rate as traced by bolometric line emission, integrated over all galaxy luminosities and including emission from any diffuse intra-halo component. Foreground line confusion from lower redshift [OIII] and Hβ lines can be robustly removed by cross-correlating spectral lines in multiple bands. For example, $z = 3$ Hα line fluctuations are detected in a band centered at $2.62\,\mu$m, while at the same redshift [OIII] fluctuations are present in a band centered at $2.00\,\mu$m. These secondary lines are useful, however: cross-correlating two independent line measurement traces the galaxies at z = 3 without masking, and naturally rejects any line contaminants or systematics that may be present in one of the two bands. In addition to the tomographic measurements and two main science cases, the SPHEREx all-sky archive will be a resource for numerous exciting and diverse astronomy investigations.

CDIM

The Cosmic Dawn Intensity Mapper (CDIM) is a NASA Probe-class Mission Study designed to be a survey instrument optimized for reionization studies, answering critical questions on how and when galaxies and quasars first formed, the history of metal build-up, and the history and topology of reionization, among other

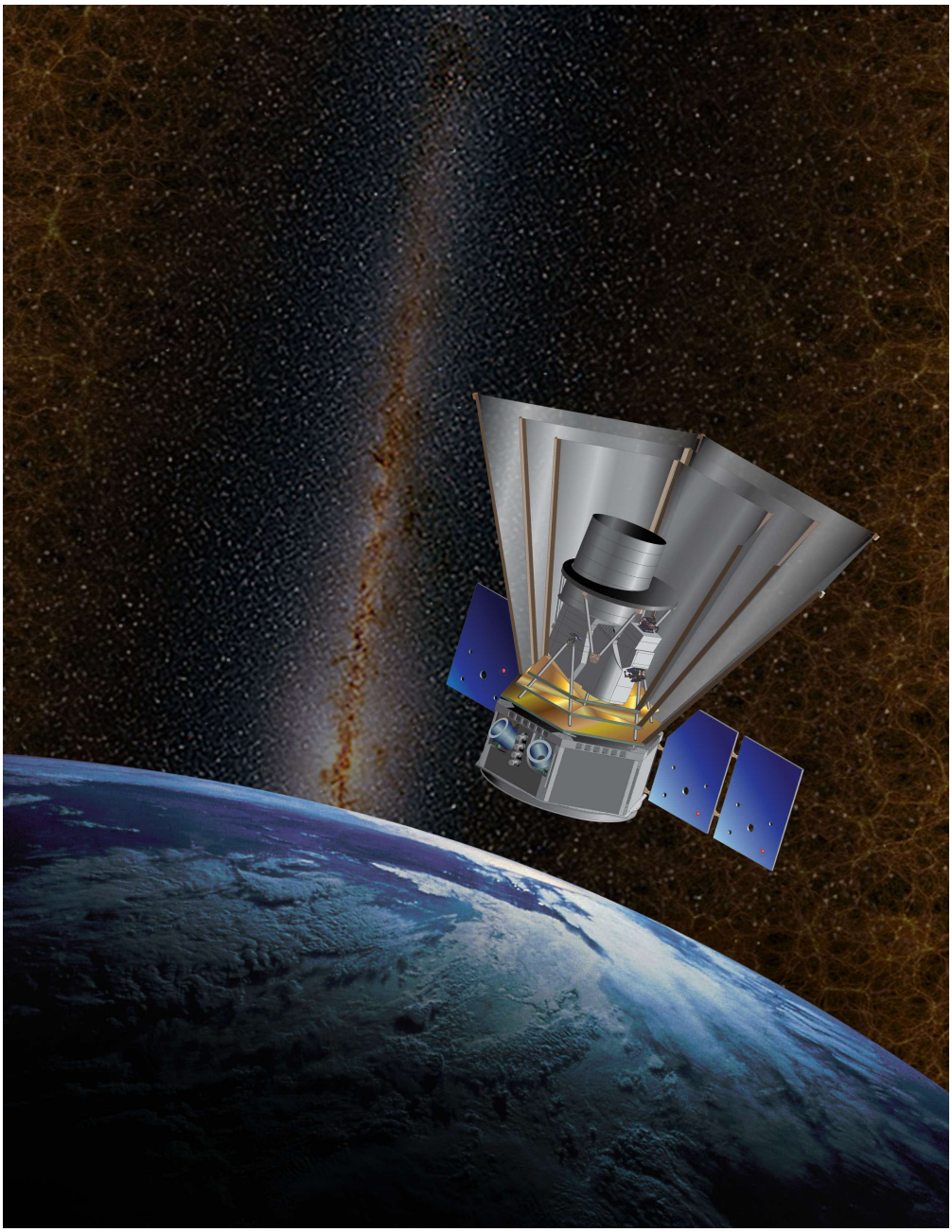

Figure 27. *SPHEREx is a NASA Medium Explorer mission designed to 1) constrain the physics of inflation by studying its imprints on the three-dimensional large-scale distribution of matter, 2) trace the history of galactic light production through a deep multi-band measurement of large-scale clustering, and 3) investigate the abundance and composition of water and biogenic ices in the early phases of star and planetary disk formation. SPHEREx will measure near-infrared spectra from* $0.75 - 5.0$ *microns over the entire sky. It implements a simple instrument design with a single observing mode to map the entire sky four times during its nominal 25-month mission. The resulting rich legacy archive of spectra will bear on numerous scientific investigations. (Courtesy of Olivier Doré)*

questions. CDIM will be a 1.0m-1.3 m-class infrared telescope capable of three-dimensional spectro-imaging observations over the wavelength range of 0.75–7.5 μm, at a spectral resolving power $\Delta\lambda/\lambda \sim 500$. CDIM will provide spectroscopic imaging over 10 $\square^\circ$ instantaneous FoV, at 1 arcsecond/pixel. The depths, in equivalent broad-bands by combining narrow-band images, are comparable to depths reached by WFIRST (Figure 28). This will be achieved with linear variable filters (LVFs) sitting on top of a focal plane of 36 2048^2 detectors. The two-tiered wedding-cake survey, taking over three years, will consist of a shallow tier spanning close to 300 $\square^\circ$ and a deep tier of about 25 $\square^\circ$. CDIM will complement JWST with cosmological survey fields, as JWST will be limited to a handful of deep fields with a total area of several hundred $\square'$, and provide spectroscopic data beyond 2 < m for the WFIRST surveys, allowing spectroscopic detection of Hα at z> 2 and galaxies at z > 6.

CDIM survey data will allow to (i) determine spectroscopic redshifts of WFIRST-detected Lyman-break galaxies out to $z \sim 10$; (ii) establish the environmental dependence of star-formation during reionization through clustering and other environmental measurements; (iii) establish the metal abundance of first-light galaxies during reionization over two decades of stellar mass by spectrally separating NII from Hα and detecting both Hβ and OIII; iv) measure 3D intensity fluctuations during reionization in both Lyα and Hα; and (v) combine intensity fluctuations with 21-cm data to establish the topology of reionization bubbles.

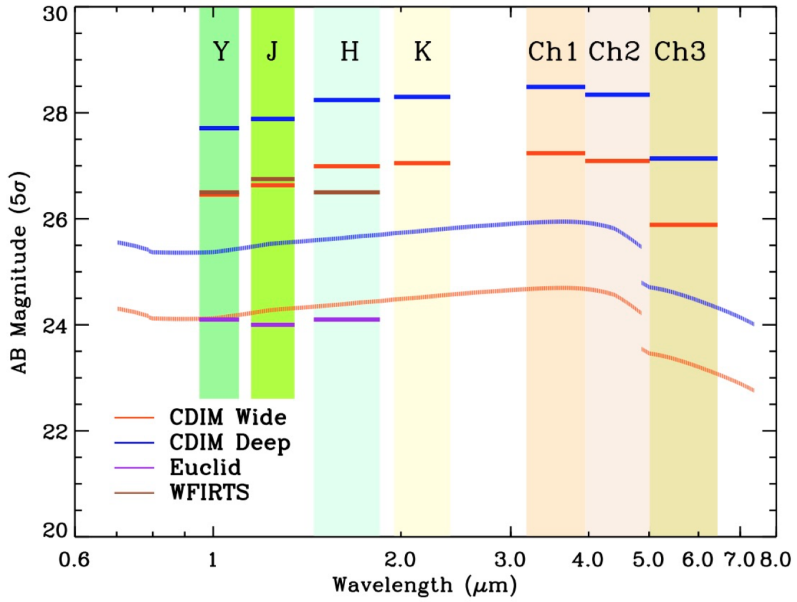

Figure 28. *Depth vs wavelength. CDIM covers 0.75 to 7.5 μm at R=500 (leading to 1360 narrow-band images); 5σ depth (AB mag) is shown in thin lines for the full R=500 spectrum. The 5σ depths in broad bands (by combining appropriate narrow-band images) in z, Y, J, H, K, Ch1, Ch2, and Ch3 are shown as red and blue bars for both wide (300 $\square^\circ$) and deep (25 $\square^\circ$) surveys, respectively. The wide survey depths are roughly matched to WFIRST-HLS (brown bars in YJH) while the deep survey depth is matched to WFIRST medium-deep survey expected over an area of 25 $\square^\circ$ (depths not shown). Euclid depths are shown in purple bars. CDIM is best-suitable for wide-field R=500 spectro-imaging over areas > 20$\square^\circ$. (Courtesy of Tzu-Ching Chang)*

PIXIE

PIXIE, proposed as a NASA Medium-class Explorer mission, is designed to measure the CMB polarization and absolute spectrum on large angular scales. It uses an FTS absolute spectro-polarimeter architecture similar to FIRAS, but with sensitivity $\sim 1000\times$ greater. This sensitivity is made possible largely through 100 mK cooling, which brings detectors to background-limited sensitivity. It will map the sky at 1.65° FWHM (effective Gaussian) across frequencies from ≈ 45 GHz to ~ 2 THz in 15 GHz bands.

While it was not designed with intensity mapping in mind, PIXIE and similar architectures provide a unique constraint on the line emission monopole [123, 162, 163] and anisotropy [114, 164] on the largest scales on the sky. PIXIE's 15 GHz-wide, adjacent bands are well-matched to [CII] and higher-J CO intensity mapping after reionization (PIXIE is not well-matched to CO $J = 1 - 0$ observations because it would require twice the linear size, difficult to accommodate in the MIDEX cost cap). In addition, its narrow, adjacent bands with precise inter-band calibration aid in modelling and removing the galactic and extragalactic foreground emission [114, 164]. A spectrometer also contains more redshift information, which may be used to calibrate photometric redshifts in surveys such as LSST [90].

LIME/CIBER

The near-IR extragalactic background contains a host of lines which appear in the visible and near-IR originating from high-redshift structure responsible for reionizing the Universe [165, 166]. LIME proposes to measure the power spectrum of these sources at various redshifts, focusing on the continuum emission between emission lines from 1–2 μm. The proposal for LIME is based on successful measurements of extragalactic background light (EBL) from the Cosmic Infrared Background Experiment (CIBER), designed to characterize the $1-2\,\mu$m EBL [167], and over the course of four sounding rocket flights [168] has successfully measured the amplitude of the near-IR background fluctuations on arcminute scales in two broad bands [169].

CIBER detects an electromagnetic spectrum that is nearly Rayleigh-Jeans with an indication of a turn over at $\lambda = 1.1\,\mu$m, a spectrum that is significantly bluer than the integrated light from galaxies. These fluctuations have been interpreted as arising from intra-halo light (IHL) from old, low mass stars residing in dwarf galaxies or dissociated from their parent galaxies during merging events over the history of the Universe. This population has implications for large scale structure formation, implying the existence of a previously undetected population that may account for a non-negligible fraction of the missing baryons in the Universe.

The need for further measurements of the fluctuating component of the near-IR EBL motivates CIBER-2, a second rocket-borne instrument designed to conduct comprehensive measurements of EBL anisotropy on arcsecond to degree angular scales in six broad bands covering $0.5-2.5\,\mu$m [170]. With an intensity mapping figure of merit an order of magnitude larger than its predecessor's, CIBER-2 is designed to measure the near-IR EBL anisotropy with the sensitivity, spectral range, and spectral resolution required to disentangle the contributions to the near-IR EBL from reionization, IHL, and local galaxies and foregrounds. The instrument is currently being fabricated and integrated, and first flight is expected in 2018.

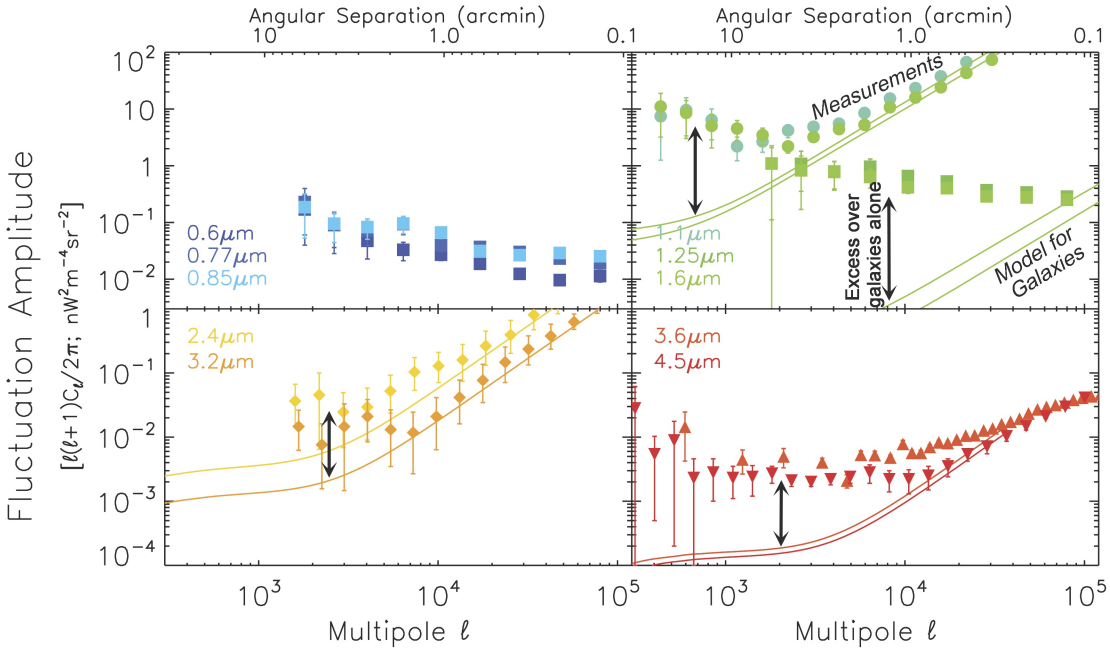

Figure 29. *Fluctuation power measurements compared to expectations from galaxies in the universe. The current set of optical/IR measurements are shown by the data points, and corresponding models for the power spectrum of galaxies at the equivalent source masking depths [171] are shown as curves. These data all show deviation from the galaxy-only model at large angles corresponding to scales of a few arcminutes and larger.* The source of this excess emission is currently unknown. *The electromagnetic spectrum of the excess fluctuation is Rayleigh-Jeans to about* 1.2 *μm at which point it falls sharply into the optical [169, 172]. The measurements include: HST (squares - [172, 173]); Spitzer (downward facing triangles - [174], upward facing triangles [175]); Matsumoto2011 (diamonds - [176]); and CIBER (circles - [169]). Formal correlation between CIBER and Spitzer data set is close to unity, which is strong evidence that the emission seen at all wavelengths is astrophysical in origin and arises from a common source. (Courtesy of Michael Zemcov)*

4.3 Large Scale Structure and Dark Energy at Redshifts z=0–2.5

Observations of neutral hydrogen supported within galaxies promise to measure redshift dependence of Baryon Acoustic oscillations [177], resulting in a precise constraint of Dark Energy models at redshifts difficult to probe with optical galaxy surveys. Projections from 21 cm measurements of BAO show promise for tight constraints on dynamical dark energy [178–181], and 21 cm emission from galaxies at high redshift has been demonstrated through cross-correlation with deep optical galaxy surveys [182, 183], and a limit has been placed from the autocorrelation spectrum [111]. Upcoming instruments dedicated to measuring the matter power spectrum from 21-cm emission are described in this section, and focus on redshifts between 0.2–2.5 to target interesting regimes for Dark Energy probes. The SKA-MID will form a high-resolution galaxy survey in this redshift regime while other radio interferometers can be optimized to be sensitive to the scales of interest for BAO to form experiments dedicated to better understanding Dark Energy.

CHIME

The Canadian Hydrogen Intensity Mapping Experiment (CHIME) is a new cylindrical transit radio interferometer located at the Dominion Radio Astrophysical Observatory (49°19'15"N 119°37'26"W). CHIME consists of 4 cylindrical reflectors with 1024 dual-polarization feeds operating between $400 - 800$ MHz across four parabolic $f/0.25$ cylinders which are each 20 m wide $\times$ 100 m long. It will have angular resolution 20' – 40' and survey $f_{\rm sky} \sim 3/4$ with 50 K receiver noise across 1024 frequency channels. The primary science goal of CHIME is to measure the expansion rate of the Universe and better understand the nature of Dark Energy with Baryon Acoustic Oscillations (BAO) via intensity maps of neutral hydrogen between a redshift range of $z \sim 0.8 - 2.5$.

As is true of all 21 cm instruments, foreground emission from the Milky Way galaxy is far brighter than the cosmological signal of interest ($\sim$100 μK signal compared to foreground emission as high as 700 K). CHIME will use a Karhunen-Loeve transform method of foreground filtering, a technique that has been verified with simulations [181] however it requires that the foregrounds appear as spectrally smooth, setting a stringent requirements for instrument calibration. The CHIME collaboration is exploring a broad array of calibration techniques for gain and beam calibration [184, 185]. The wide sky coverage and high frequency resolution will provide maps of Large Scale Structure which could be cross-correlated with a variety of current and upcoming galaxy/quasar surveys (SDSS, DES, LSST, DESI, HSC, Hetdex).

CHIME has been built and will begin observations by the end of 2017, and will operate for five years to make sample variance limited measurements of BAO (the error bar projections are shown in Figure 30). Prior to building CHIME, the collaboration built the CHIME pathfinder [186], a test-bed instrument with 128 dual-polarization feeds deployed on two 20 m wide $\times$ 36 m long cylinders. The CHIME pathfinder started its two year survey in December 2015, and has published one constraint on the brightness of fast radio bursts (FRBs) [23], and should be capable of interesting constraints on Dark Energy (see pathfinder projections in Fig. 30).

HIRAX

The Hydrogen Intensity and Real-time Analysis eXperiment (HIRAX) [78] is a planned radio telescope array that will consist of ≈ 1000 close packed 6 m dishes that will be deployed in South Africa. HIRAX will operate between 400–800 MHz in 1024 linearly spaced frequency bins, corresponding to a redshift range of $0.8 < z < 2.5$ and a minimum $\delta z/z$ of ≈ 0.003. It will employ first stage amplifiers directly embedded in the wide-band feed, and use radio-frequency-over-fiber to transmit the radio signals from the dishes to the correlator to reduce the signal loss and temperature variations.

HIRAX will survey the majority of the southern sky to chart the expansion history of the universe and place competitive constraints on the dark energy equation of state and its time evolution. In addition to BAO cosmology, the large survey area and real-time analysis capabilities of the HIRAX array will make it a powerful tool for identifying pulsars and astrophysical transients such as fast radio bursts (FRBs) as well as providing an excellent platform for studying neutral hydrogen absorbers. The extensive overlap with other cosmological surveys in the Southern hemisphere should provide many opportunities for a variety of cross-correlation studies, including improved photometric redshift errors for LSST [90] and possibilities for understanding the HI bias from cross-correlations with CMB surveys [84], and for joint constraints on cosmological parameters.

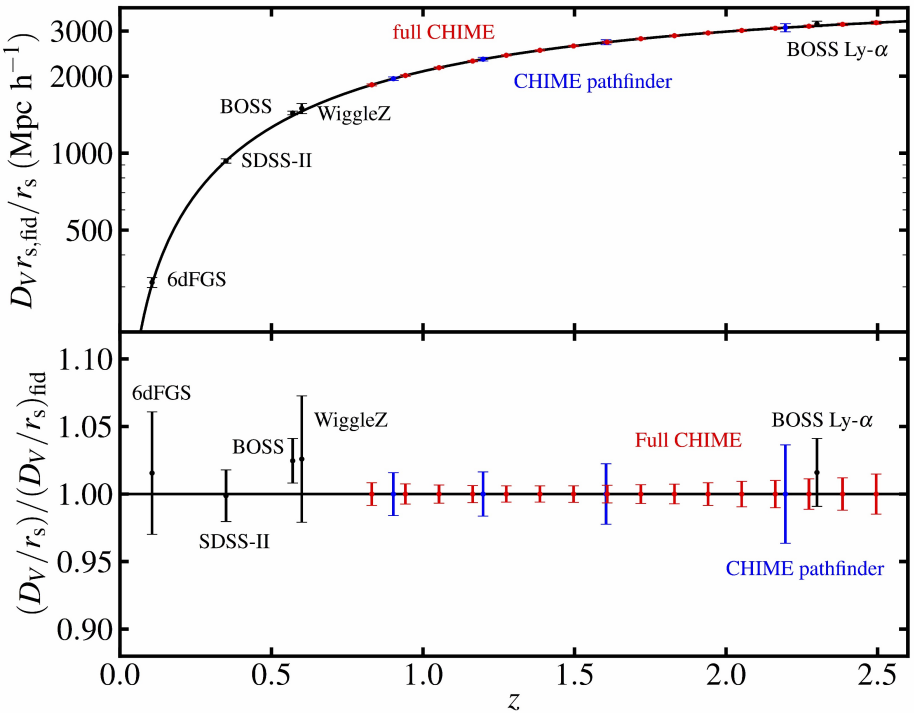

Figure 30. *Projections for CHIME and CHIME pathfinder error bars on the cosmological distance volume. CHIME and the CHIME pathfinder are expected to make sample variance limited measurements of BAO, improving constraints on Dark Energy. CHIME, as a physically larger interferometer, has improved error bars at higher redshift due to its higher resolution. (Courtesy of J.R. Shaw)*

A drone based calibration system is being developed for HIRAX, which will allow the array to be calibrated in situ, at zenith pointing, or over the range of operational dish elevations. The drone can easily be programmed to execute arbitrary beam mapping flight paths in the array far field. For a 6 m dish, the far field is at most $2D^2/\lambda = 200$ m at 800 MHz. Data taking and beam mapping are performed with a modified version of the ECHO software developed by Danny Jacobs [187].

As of the time of writing, an initial eight-element prototype array has been deployed at the Hartebeesthoek Radio Astronomy Observatory (HartRAO), providing the first end-to-end test of the HIRAX hardware. Build up to the full array will take place over an estimate period of three years, beginning in 2019. Because of the inherently modular nature of the array, the completed portions of the array will be able to operate throughout the array deployment.

Meerkat and SKA-MID

The SKA will have a second sub-array, SKA1-MID, which is a mid-frequency dish array to be constructed on the South African site. In addition to ~ 130 new (15m diameter) SKA1 dishes, it will also incorporate the 64 (13.5m) dishes of the co-sited MeerKAT array. SKA1-MID dishes will eventually be fitted with 5-band receivers, covering bands from 350 MHz up to 14 GHz. Initial construction will likely prioritize Bands 2, 5, and 1, the most relevant for 21cm intensity mapping being Band 2 (covering $950 - 1760$ MHz), and Band 1

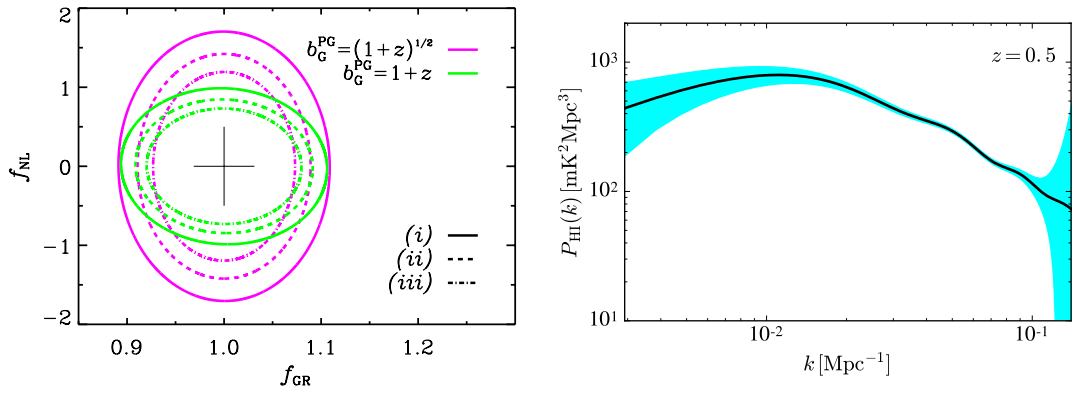

Figure 31. *Left: joint marginal error contours using the multi-tracer technique for primordial non-Gaussianity (f_{NL}) and GR corrections (f_{GR}) considering different scenarios for the bias and Euclid/LSST surveys [190]. Right: HI power spectrum detection with MeerKLASS, showing the expected signal (black solid) and measurement errors (cyan) [191]. (Courtesy of Mario Santos)*

(350 − 1050 MHz). The MeerKAT receivers support 2 bands with different frequency ranges to the SKA1 receivers.

Since its baselines are not small enough to probe the most relevant cosmological scales, the accepted plan is to use the auto-correlations from each dish which will be supported by calibration against noise diodes and an appropriate scan strategy to reduce $1/f$ noise. Assuming that residual foregrounds and calibration uncertainties can be controlled well enough, a 10,000 hour SKA1-MID IM survey over 30,000 deg^2 would rival large galaxy redshift surveys such as Euclid in terms of constraints on the dark energy equation of state [55] and provide powerful tests of dark energy models and modifications to General Relativity [188, 189]. Due to its low resolution in single dish mode, SKA1-MID will be particularly transformational on very large scales, where it can provide unique constraints on primordial non-Gaussianity and make the first detections of general relativistic corrections. This will be especially powerful when in combination with future optical/infrared surveys such as Euclid and LSST by using the multi-tracer technique [69, 190] (see Fig. 31, left).

In the immediate future, with 64, 13.5m dishes and two frequency bands covering the z=0 to 1.4 redshift range, MeerKAT, the SKA precursor in South Africa, will have the capability to produce high impact cosmological constraints using the same approach for HI intensity mapping (e.g. using the auto-correlations from each of its dishes). A wide area survey has therefore been proposed, known as MeerKLASS (MeerKAT Large Area Synoptic Survey [191, 192]) which aims to start observations in 2018. Covering an area of $\sim 4000\,\mathrm{deg}^2$ for ~ 4000 hours, it will potentially provide the first ever measurements of the baryon acoustic oscillations using the 21cm intensity mapping technique [193], with enough accuracy to constrain the nature of dark energy (see Fig. 31, right). The combination with multi-wavelength data over the same area, will give unique additional information, such as stringent constraints on primordial non-Gaussianity using the multi-tracer technique [194]. It will also be a crucial step on the road to using SKA1-MID for cosmological applications, as described in the top priority SKA key science projects.

BINGO

BINGO [Baryon acoustic oscillations In Neutral Gas Observations 195, 196] is a large (40m) transit telescope that is planned for construction in an open-cast mine in Minas Corrales, near the Uruguay-Brazil border. It will target baryon acoustic oscillations at $0.13 < z < 0.48$, with a drift-scan survey over a 15×200 degree patch of the sky. The telescope will have a large focal plane with at least 50 feeds operating in autocorrelation mode, with pseudo-correlation receivers to promote gain stability and thus reduce the impact of $1/f$ noise. The feed horns are large – 4.5m long with 1.7m apertures – and will be constructed from a lightweight foam wrapped in a conductor, to reduce mass. The instantaneous field-of-view is 15×15 degrees, with a ~ 40 arcmin resolution at 1 GHz. Being one of the few planned non-interferometric 21cm IM surveys, BINGO will be capable of recovering large scales in the HI distribution in addition to the BAOs. While foregrounds and instrumental effects remain important, they are expected to be less drastic than for lower-frequency experiments targeting the EoR [197]. BINGO will be largely funded by a grant from FAPESP (Brazil), with contributions from the other partners in the UK, Uruguay, Switzerland, South Africa and China. First results are expected by 2020.

5

Theoretical Backbone

5.1 Modeling

Line-intensity mapping has the potential to provide us with valuable insights into many physical quantities which play a role in the physics of the ISM, such as the strength of the radiation field, the number density of hydrogen and electrons in the neutral and ionized medium respectively, the gas metallicity and the mean star-formation rate. The observed signal in an intensity mapping survey depends on many physical processes governing the interplay between energetic sources, and gas and dust in galaxies. It is therefore very important to carefully consider how to model this signal, both when forecasting the signal-to-noise ratio of upcoming and future surveys, and when interpreting the results of these surveys.

Two main approaches are usually employed in modeling the strength of a given emission line: through interpretation of the clustering signal; or through its dependence on the local environment. The first method is phenomenological, and is usually built upon empirical relations between the intensity of a line and the measured far-infrared luminosity of a galaxy, which quantifies its total star-formation rate. Using scaling relations between star-formation rate (or infrared luminosity) and halo mass (derived from abundance matching), it is then possible to express the line luminosity of a galaxy as a function of its host halo mass, and use a halo model approach to compute statistical quantities of interest such as the three-dimensional power spectrum [123, 198–200]. This method, while providing rough predictions for the expected amplitude and shape of power spectra, relies on empirical relations based on a very limited set of observations of galaxies at some particular redshifts. Scaling relations based on different recipes result in quite different amplitudes of the power spectra [often of an order of magnitude or more, see, e.g., discussion in 201, 202]. Moreover, the redshift evolution of these relations is often poorly known, which can be problematic when targeting, e.g., the epoch of reionization. Furthermore, the power of intensity mapping is to probe objects too faint for individual detections—and therefore by definition outside of the range of the measured scaling relations.

The second approach is based on numerical simulations and semi-analytic models of galaxy formation and evolution. These models capture in detail many processes governing the physics of the Interstellar Medium (ISM), and are able to predict the emission from multiple lines up to very high redshifts [see, e.g. 203, 204]. However, they also require numerous assumptions, which often makes them computationally demanding, inflexible, and hard to implement for quick computations.

Most of the modeling work up to now has been focused on forecasting results for future surveys, but the real challenge of modeling will be to translate intensity mapping measurements into useful astrophysical information. Scaling relation models are straightforward to work with, but they provide relatively little insight into the physical processes which govern line emission. Semi-analytic models, on the other hand, are tied intimately into detailed physics of the galaxy population, but this complexity makes them difficult to use and may obscure useful information amid a large number of assumptions and free parameters. Going forward, it will be important to consider intermediary approaches to model the line emission of atoms and molecules in galaxies combining phenomenology, numerical analysis, and when available, direct observations.

5.1.1 [CII] line-intensity mapping

The [CII] 157.7 μm fine-structure line arising from the $^2P_{3/2} \rightarrow ^2 P_{1/2}$ transition is the brightest among all metal lines emitted by the interstellar medium (ISM) of star-forming galaxies. It is associated with the star formation in galaxies [205–208] and plays a key role in the energy balance of galaxies, as it provides one of the most efficient cooling processes for the neutral ISM. A particularly attractive application of intensity mapping is the study of faint galaxies in the Epoch of Reionization. In fact, if the galaxy luminosity function has a sufficiently steep faint end (as deduced from the study of UV luminosity functions), the observed radiation is actually dominated by unresolved sources [156].

The signal is however swamped by a combination of different foregrounds and contaminating lines that must be removed. In addition to the far-infrared (FIR) continuum foreground, other emission lines emitted from a range of redshifts fall at the same frequency of the [CII] signal; they act as *contaminants*. Among these are the OI line ($\lambda 145\,\mu$m), the two NII lines ($\lambda = 122, 205\,\mu$m), and a handful of CO rotational transition lines in the range 200-2610 μm. Among these, the CO rotational transition lines are the most relevant here. For example, since the CO(4-3) line has a wavelength 651 μm, if emitted from $z = 0.45$ galaxies, it contaminates the [CII] emission from $z = 5$ galaxies. However, the luminosity distance from $z = 0$ to 0.45 is only $\sim 5\%$ of that to $z = 5$. As the flux is inversely proportional to the square of the luminosity distance, whereas the proper distance interval that corresponds to the same bandwidth is $\propto (1+z)^{-3/2}$, the CO flux can be higher than the [CII] one, even ignoring the cosmological evolution of the star-formation rate density.

The relevant quantity for experiments is the power spectrum of the signal. This can be obtained analytically [2, 156], or numerically [4]. Although deducing the [CII] signal from simulation should be more robust, it implies a number of difficulties related to the large volumes required at the same time resolving galaxies contributing to the faint end of the luminosity function. For this reason, very often hybrid methods are used in which N-body simulations are used to provide the correct large scale structure correlation properties, and empirical relations between star formation, metallicity and [CII] emission are used.

Yue et al. [4] used star-formation rates and metallicity derived small scale (box size 10 h^{-1} Mpc) galaxy simulations including a sub-grid treatment of the interstellar medium [209] with an empirical approach to compute the $L_{\rm CII} - M_{\rm h}$ relation taken from Vallini et al. [210]. This relation is subsequently applied to halo catalogs built from the large-scale N-body simulation `BolshoiP`, to generate mock maps of [CII] signal. The FIR continuum foreground, derived from abundance-matching techniques was added to the generated mock maps, along with contamination from CO lines. The latter was computed from intermediate $L'^{\rm J}_{\rm CO} - L_{\rm IR}$ relations that were better fitted from measurements of both local and high-redshift samples. Mock maps were generated for FIR continuum and CO emission, in close analogy with the [CII] mock maps.

FIR foreground removal and CO masking experiments on the total mock maps was performed to recover the [CII] angular power spectrum. Efficient subtraction of the CO contamination can be achieved if the map has a sufficiently high spatial resolution (necessary to preserve a statistically meaningful number of pixels). In practice, a minimum resolution of $\sim 40''$ is required to remove CO contamination by dropping all pixels containing galaxies brighter than $m_K = 22$ in the relevant redshift range.

The [CII] signal from $z_{\rm CII} \sim 5 - 6$ is detectable, for example, by a ground-based, noise-limited telescope with a 6 m aperture, $T_{\rm sys} = 150\,$K, a FIR camera with 128×128 pixels in about 5000 hr total integration time. Fig. 32 shows that at redshift 5, most of the [CII] fluctuation signal is from halos in the mass range $M_h = 10^{11-12}\,M_\odot$ (H-band apparent magnitude $\sim 26.8{-}23.8$). According to this model, halos below $10^{11}\,M_\odot$ produce less than 1% of the total [CII] fluctuations. The measured high-z [CII] signal is particularly useful for studies of halos in the above narrow mass range. To access the fainter galaxies responsible for reionization, the [CII] flux from bright galaxies needs to be measured by a high-resolution interferometer array, and then

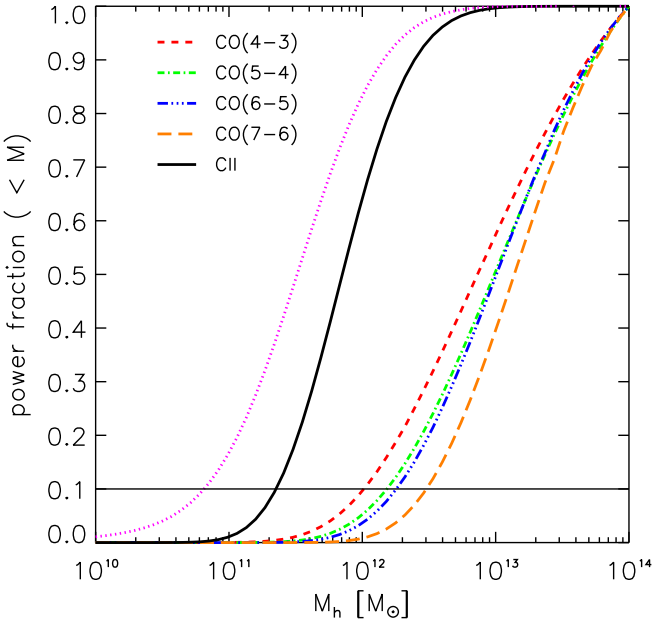

Figure 32. *Fractional contribution from halos below $M_{\rm h}$ to the clustering term of the angular power spectrum for the 316 ± 0.65 GHz frequency bin for various emission lines. Note the contribution from several contaminating CO lines. The purple dotted line is the FIR continuum. The horizontal line guides the eye on the reference value 0.1. Adapted from [4]. (Courtesy of Andrea Ferrara)*

subtracted in the relevant pixels. In practice, this operation would be challenging. For example, there are ~ 7000 halos in the light-cone used here whose [CII] emission appears in the (316 ± 0.65) GHz frequency bin and $\gtrsim 10^{-22}$ Wm^{-2}, corresponding a mass $M_{\rm h} \gtrsim 6 \times 10^{10}\, M_\odot$. In order to resolve them with a signal-to-noise ratio of > 5, assuming a line width 50 km s^{-1}, the required sensitivity is 4×10^{-5} Jy. For comparison, the 10 hr ALMA r.m.s. noise at $316\,{\rm GHz} \pm 50\,{\rm km\,s^{-1}}$ is $\sim 7 \times 10^{-5}$ Jy. To detect the [CII] signal from these sources, a space telescope with background-limited sensitivity, and an interferometer array that could measure radiation flux of all bright sources at relevant redshifts, are necessary.

5.1.2 CO Line-Intensity Mapping, Scaling Relations, and Direct Measurements

Carbon monoxide (CO) is the most abundant molecular species after H_2, whose emission lines arise from a "ladder" of rotational transitions ($J \to J-1$), with the ground-state CO(1–0) transition at $\nu_{1\to0} = 115.27$ GHz ($\lambda = 2.6$ mm) and higher transitions at $\nu_{J\to J-1} = J\nu_{1\to0}$. CO traces the metal-enriched cool to warm molecular ISM, where stars form efficiently, which motivates the empirical conversion between CO and H_2 [for a review, see 211], and by extension star-formation.

Several phenomenological models of the expected CO line-intensity mapping signal exist [e.g., 10, 122, 198, 199, 212, 213]. Some are analytic halo models based on halo occupation distributions, some rely on semi-analytic models, while others directly populate light-cone catalogs generated from numerical dark matter halo simulations (see Table 3 of 98, for a summary of the model differences). A common thread among many

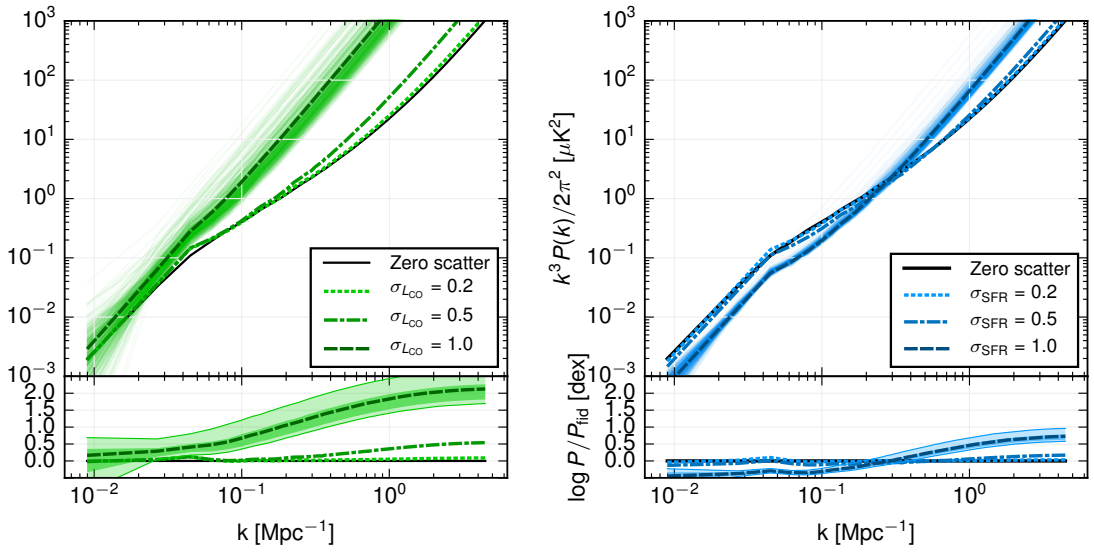

Figure 33. *Effect of scatter on the CO power spectrum, as parameterized by: SFR given $M_h(\sigma_{\rm SFR}, left)$ or $L_{\rm CO}$ given SFR ($\sigma_{L_{\rm CO}}, right$). As scatter approaches 1 two things are evident: (1) the power spectrum begins to look like a pure shot noise spectrum, since any clustering signature is increasingly buried by the large halo-to-halo scatter, and (2) the scatter introduces significant variance into the power spectrum, shown as thin lines (shaded region in the lower panels) for 100 realizations. (Courtesy of Tony Li)*

of them is the use of star-formation rate as a proxy for CO luminosity, through the use of empirical scaling relations based on observables, for which bolometric infrared luminosity (L_{IR}) — which traces the light from young stars as absorbed and re-radiated by dust grains, which are abundant in star-forming regions — is the most direct. L_{IR}, whose units are $L_\odot$, refers commonly to the integral of the thermal spectral energy distribution [effectively a modified blackbody, $\nu B(\nu)$; e.g., 214] over the rest-frame 8–1000 μm region.

The SFR–L_{IR} relation is typically taken from Kennicutt [215]:

$$\frac{\rm SFR}{M_\odot\ {\rm yr}^{-1}} = \delta_{\rm MF} \times 10^{-10} \left(\frac{L_{\rm IR}}{L_\odot}\right), \tag{5.1}$$

where $\delta_{\rm MF} \approx 1$ when assuming an initial mass function (IMF) from [216].

A power-law relation then connects the IR and CO luminosities:

$$\log\left(\frac{L_{\rm IR}}{L_\odot}\right) = \alpha \log\left(\frac{L'_{\rm CO}}{\rm K\ km\ s^{-1}\ pc^2}\right) + \beta. \tag{5.2}$$

Values for galaxies in the redshift range $z \approx 1-3$ for (α, β) span (1.13, 0.53), (1.37, -1.74), (1.0, 2.0), (1.17, 0.28) taken from [217–220], highlighting the uncertainties that are still present in the scaling relations.

In practice the mapping from halo mass to stellar mass and/or star-formation rate, and then to $L_{\rm IR}$ and finally CO luminosity are stochastic, and the level of scatter introduced at each step to account for that has consequences on the predicted power spectrum (Fig. 34). Li et al. [98] added log-scatter $\sigma_{\rm SFR}$ and $\sigma_{\rm L_{CO}}$ of both 0.3, motivated by the scatter in models of SFR at a given halo mass [221]. As shown in the following "FIRE Simulations" section, that may be an underestimate[1]. Also notable is a recent model from Wu and

[1] IMAPPER2 is a modeling code to populate dark matter halo catalogs with CO line luminosities, available on github at https://github.com/tonyyli/imapper2/

Doré [222] which predicts a deficit from Kennicutt [215] of $L_{\rm IR}$ in low-mass ($\log M/M_\odot < 10$) galaxies, which could impact the strength of the power spectrum signal.

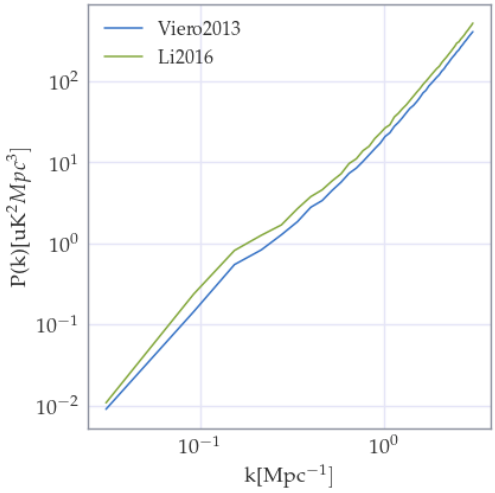

Figure 34. *Comparing the Li et al. [98] and Viero et al. [223] models applied to* IMAPPER2[1]. *Li et al. [98] converts SFR to $L_{\rm IR}$ to $L_{\rm CO}$, while Viero et al. [223] uses fits to direct measurements of the $L_{\rm IR}$ via* SIMSTACK. *Both use a minimum halo mass of $10^9\,{\rm M}_\odot$ and $\sigma_{L_{\rm CO}} = 0.3$, and a scaling relation $\alpha_{\rm CO} = 1.37$ [218]. (Courtesy of Marco Viero)*

Alternatively, models are under development that explore the dependence of the IR properties of galaxies on their physical properties — including stellar mass, age, and extinction — by fitting directly to measurements (Fig. 34). This in turn would bypass the SFR to $L_{\rm IR}$ step, and more naturally account for stochasticity in the global sample. Because measuring $L_{\rm IR}$ for large samples [e.g., 1 million objects in the $2\,{\rm deg}^2$ COSMOS field; 224] with ALMA is prohibitively expensive, and submillimeter images (SPIRE, SCUBA2, etc.) are so source-confusion dominated as to be effectively continuum intensity maps, statistical methods like stacking [e.g., SIMSTACK 223] are necessary. The first published model to use this approach was Sun et al. [225], which found a scatter of $L_{\rm IR}$ around the main sequence of star formation of $\sigma_{\rm LIR} = 0.3$.

5.1.3 Lyα Line-Intensity Mapping

The Lyα line most likely represents the optimal feature for a line-intensity mapping experiment. Historically, it has been used for high-z Lyα-emitting (LAE) galaxy searches as it is the most luminous UV line [226, 227]. These searches are often hampered by the fact that intergalactic H I can scatter the bulk of Lyα photons out of the line of sight, making systematic detections of LAE during the EoR very challenging [228]. Line-intensity mapping can overcome these problems, thanks to its sensitivity to even diffuse emission from the IGM. Therefore Lyα intensity mapping seems a very promising tool to study the properties of early, faint and distributed EoR sources.

Silva et al. [5] studied this problem with semi-numerical tools, focusing on the EoR emission at $z = 7$. In a following work, Gong et al. [7] tackled the problem of line confusion, proposing the masking of contaminated pixels as a cleaning technique. These authors find that recombinations in the ISM of galaxies largely dominate the Lyα intensity and power spectrum. Pullen et al. [229] developed a simple analytical model to study

the evolution of the Lyα power spectrum at $z > 2$: their results are qualitatively different from Silva et al. [5], in that they conclude that diffuse IGM emission is the dominant source. Recently, Croft et al. [105] attempted to observe the large scale clustering of Lyα emission at $z = 2-3$ by cross-correlating the residuals in the SDSS spectra with QSOs. They claim a detection of a mean Lyα surface brightness $\gtrsim 10$ times more intense than the one inferred from LAE surveys, but still compatible with the unobscured Lyα emission expected from LBGs.

Finally, in a series of papers, Comaschi and Ferrara [230] (see also [8, 231]) presented a complete study of Lyα intensity mapping including theoretical expectations and strategies to identify the optimal IM experiment. These authors find that Lyα intensity from the diffuse IGM emission is 1.3 (2.0) times more intense than the ISM emission at $z = 4(7)$; both components are fair tracers of the star-forming galaxy distribution. However, the power spectrum is dominated by ISM emission on small scales ($k > 0.01\,h\,\mathrm{Mpc}^{-1}$) with shot noise being significant only above $k = 1\,h\,\mathrm{Mpc}^{-1}$. At very large scales ($k < 0.01\,h\,\mathrm{Mpc}^{-1}$) diffuse IGM emission becomes important. The comoving Lyα luminosity density from IGM and galaxies, $\dot{\rho}_\alpha^{\mathrm{IGM}} = 8.73(6.51) \times 10^{40}\mathrm{erg\ s^{-1}Mpc^{-3}}$ and $\dot{\rho}_\alpha^{\mathrm{ISM}} = 6.62(3.21) \times 10^{40}\mathrm{erg\ s^{-1}Mpc^{-3}}$ at $z = 4(7)$, is consistent with recent SDSS determinations.

The predicted power spectrum is $k^3 P^\alpha(k,z)/2\pi^2 = 9.76 \times 10^{-4}(2.09 \times 10^{-5})\mathrm{nW^2m^{-4}sr^{-2}}$ at $z = 4(7)$ for $k = 0.1\,h\,\mathrm{Mpc}^{-1}$. Is such signal detectable? In principle the above Lyα PS for $z < 8$ is in reach of a small space telescope (40 cm in diameter, similar to the proposed SPHEREx, see [232]); detections with low S/N are possible only in some optimistic cases up to $z \sim 10$. However, the foreground interloper emission lines represent a serious source of confusion, and therefore must be removed. The host galaxies of these interloping lines can be resolved via an ancillary photometric galaxy survey in the NIR bands (Y, J, H, K). If the hosts are removed down to AB mag ~ 26, then the Lyα PS for $5 < z < 9$ can be recovered with good S/N. If [CII] intensity mapping data is available, by cross-correlating the two signals the required depth of the ancillary galaxy survey could be is within reach of Euclid (AB mag ~ 24). Alternatively, [231] suggested a promising method based on the cross-correlation between diffuse Lyα emission and LAEs. Using this technique, they show that signal-to-noise of the observed cross-correlation power spectrum does not depend significantly if the variance of the random noise introduced by contaminating lines is $\sigma_{\mathrm{N}} \leq 10\sigma_\alpha$. In these conditions the mean line intensity, I_α, can be precisely recovered. Even if $\sigma_{\mathrm{N}} = 100\sigma_\alpha$, I_α can be constrained within a factor 2. Since removing the contaminating lines in future IM surveys will not be an easy task, relying on a solid cross-correlation is crucial to extract information from these experiments.

5.1.4 Modeling the HI Power Spectrum on Non-Linear Scales

Over the next decade, several intensity mapping experiments will probe unprecedented volumes of Universe, allowing these surveys to span ultra-large scales (provided foreground contamination can be mitigated) as well as non-linear ones. Our current approaches of modeling clustering will soon reach their limits. They rely on the assumption that structure formation is linear on large scales and non-linear on smaller scales, nevertheless this statement is only true for dark matter and not for biased tracers. Indeed, short and large scale modes of biased tracers are coupled: density fluctuations of the tracer are enhanced in more massive regions as compared to those in less massive regions. Using a perturbative approach, Pénin et al. [236] showed that this coupling translates into a significant contribution of non-linear terms to the power spectrum on large scales. Therefore, on linear scales the bias is not constant but scale-dependent. This effective bias depends on the relation between the tracer and the Large Scale Structure. In the case of HI, a simple relation between the HI mass and the halo mass (MHIMh) is assumed. The HI effective bias is, at most, 15% lower than its linear counterpart at $z < 1.5$ while it is higher at $z > 1.5$. Nevertheless, the case of HI

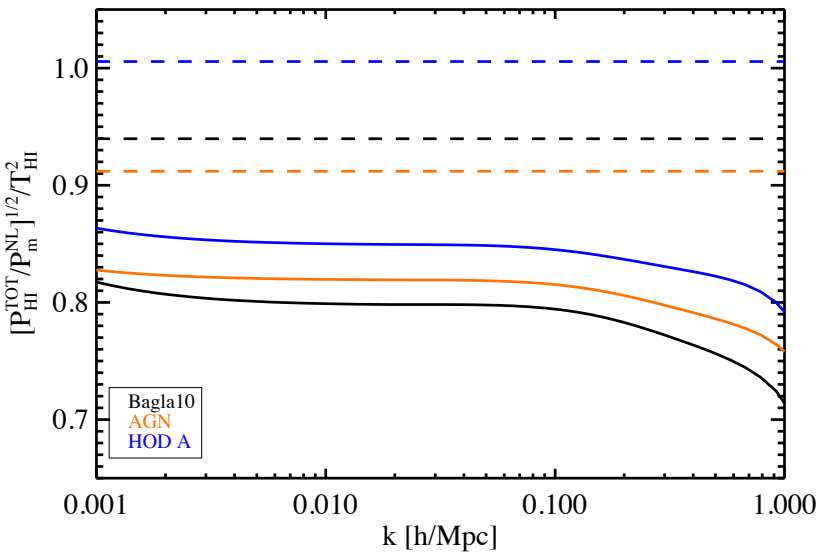

Figure 35. *Scale dependence of the HI effective bias at $z = 1$,defined as the ratio $\sqrt{P_{\rm HI}(k)/P_{\rm m}^{\rm NL}(k)}/\overline{T}_{\rm HI}^2$ (right) for several MHIMh prescriptions in real space. $P_{\rm m}^{\rm NL}$ is the non-linear power spectra of matter. Horizontal dashed lines are the linear biases associated to each MHIMh models. The Bagla10, AGN, and HOD A are the MHIMh relations from Bagla et al. [233], Villaescusa-Navarro et al. [234], and Padmanabhan et al. [235], respectively. Adapted from Pénin et al. [236]. (Courtesy of Aurélie Pénin)*

is peculiar as the HI linear bias is, uncommonly, below unity at low redshift and above at higher redshift [237, 238]. The effective bias is compared to the linear one in Fig. 35 for several MHIMh relations.

The scale dependence of the effective bias has a significant impact on the expected signatures of cosmological parameters. It alters the ratios of the BAO peaks, modifies the scale dependence of the power spectrum with $f_{\rm NL}$ on ultra large scales [239, 240], and notably changes the shape of the 2-dimensional power spectrum for the estimation of the growth factor. Further work is required to quantify these modifications and to which extent they flaw the estimation of cosmological parameters.

However, the main source of uncertainty today is the MHIMh relation; it controls the effective bias, and more importantly, the temperature of HI which rules the overall amplitude of the power spectrum. Indeed, the actual observable is the product $T_{\rm HI}\, b_{\rm HI}$ and there is an order of magnitude difference between the HI temperatures predicted by current MHIMh prescriptions. Lastly, the MHIMh relation rules the small scale behavior of the HI power spectrum. The fact that HI is less clustered than dark matter translates into a dip in the power spectrum on small scales as shown in Fig. 35.

From a broader point of view, these results hold for any intensity mapping (or galaxy) survey over several thousands of square degrees such as SPHEREX, among others. It is worth highlighting the fact that these results also apply to cross-correlations of two biased tracers. Finally, it is critical to improve our understanding of the bias of the tracers, namely how the line luminosity relates to dark matter.

5.1.5 Semi-Analytic Models and More

Existing simulations of the expected signal for line-intensity mapping, particularly for lines other than 21-cm, have been carried out using empirical scaling laws between dark matter halo properties and line luminosity [e.g. 98, 225]. This approach is relatively simple to implement, and computationally efficient, but has several disadvantages. First, line-intensity mapping is expected to probe below the flux scales of objects that can be readily detected individually at a given redshift, so it is inevitable that these scaling relations must be extrapolated well outside of the regime where they are well calibrated. Second, the emission luminosity of optical and IR lines such as Hα, [OIII], CO, and [CII] are sensitive to the detailed conditions in the sites of their production in the interstellar medium (ISM) of galaxies, such as density, temperature, metallicity, and local background radiation field strength. The detailed physical connection between the efficiency of production of these lines and dark matter halo properties is poorly understood, and likely to be complex. Third, most of these empirical approaches have so far not attempted to simultaneously model multiple lines. As discussed further in the Techniques section, cross-correlating intensity maps across multiple lines will have enormous leverage. Finally, although line-intensity mapping experiments have great potential to provide insights into the physics of galaxy formation and its interplay with cosmology, the empirical approach is limited in its ability to aid in this goal.

However, creating physics-based models for intensity mapping is an extremely challenging problem, because of the very wide range of scales and diversity of physical processes that come into play. The processes that determine the efficiency of star formation and luminosity of lines such as CO and [CII] occur on sub-pc scales within the ISM, while galaxy properties are known to depend on their large scale environment on scales of Mpc. Line-intensity mapping experiments will map significant fractions of the sky, requiring very large volume simulations (tens of Gpc).

A promising approach for overcoming these challenges may be the use of semi-analytic galaxy formation models [for a summary and references, see 241]. Semi-analytic models capture the cosmological formation history (including any correlation with larger scale environment) using halo merger trees extracted from dissipationless N-body simulations. Within these merger trees, the approach applies simple but physically motivated recipes for a broad variety of physical processes, which generally include cooling and accretion of gas, conversion of cold gas into stars, feedback from massive stars and supernovae, chemical enrichment, black hole formation and feedback from accreting black holes. State-of-the art semi-analytic models have been shown to produce consistent predictions for global galaxy properties and their evolution compared with much more computationally expensive numerical hydrodynamic simulations [241]. In a recent generation of models the cold ISM gas is partitioned into atomic, molecular, and ionized phases according to recipes motivated by empirical relations or fitting functions derived from numerical simulations [241–246].

These models can then be coupled with radiative transfer and Photodissociation Region (PDR) models to make predictions for the line emission of rotational transitions of CO and of [CII] (Lagos et al. [245]; Popping et al. [203, 246]). In the models developed by G. Popping and collaborators, each galaxy is populated with "clouds" selected from a probability distribution function motivated by observed molecular cloud mass functions, based on the average H_2 density in each annulus. The temperature of the gas and dust is then calculated by computing the heating-cooling balance, taking into account cosmic ray heating, photo-electric heating, gravitational heating, and the exchange of energy between dust and gas. The primary cooling mechanism for the gas is line radiation through CO, atomic carbon [CI], and ionized carbon [CII]. Finally, the level populations of the molecule or atom of interest, and the probability that a photon at some position in the cloud can escape the system, are calculated [see e.g. 247].

To date, these studies have focused on comparing the model predictions with observations of individually detected galaxies. P14 and P16 present a comparison of their model predictions with observed scaling

relations for CO and [CII] emission properties vs. galaxy properties such as FIR luminosity, SFR, and stellar mass, as well as CO and [CII] luminosity functions. They find very good agreement with existing CO-galaxy scaling relations and LFs over a broad range of redshifts. These models fare less well at reproducing the observed scaling relations and LFs for [CII]. However, work in progress (G. Popping et al. in prep) finds that implementing the approach presented in Narayanan and Krumholz [248], which takes into account the radial dependence of conditions *within* individual clouds, will lead to improved predictions for CO and [CII] by these semi-analytic models.

The approach described above can be used to create predictions for a few times $\sim 10^4$ galaxies, but is probably still prohibitively expensive for computing very large area maps. A promising approach would be to use statistical techniques such as principal component analysis or machine learning to develop computationally efficient methods for assigning sets of galaxy properties (UV-FIR continuum plus line emission) to dark matter halos in large volume cosmological simulations. Models run on merger trees extracted from numerical N-body simulations, as well as more detailed fully numerical hydrodynamic simulations, should be used to study the "second order" dependence of line emission efficiency on large scale environment, and to include this in these mappings.

Similarly, one can interface predictions from semi-analytic models with semi-numerical models of radiative transfer and reionization [e.g. 249–251] to create mock 21-cm maps. The semi-analytic model straightforwardly provides predictions for the ionizing emissivity of each halo, based on the modeled stellar population in each galaxy, thereby replacing the very simplified halo mass based parameterizations previously utilized in these types of models. An important unknown parameter is the escape fraction of ionizing photons, which may vary depending on the instantaneous galaxy properties such as star-formation rate, gas fraction, and metallicity.

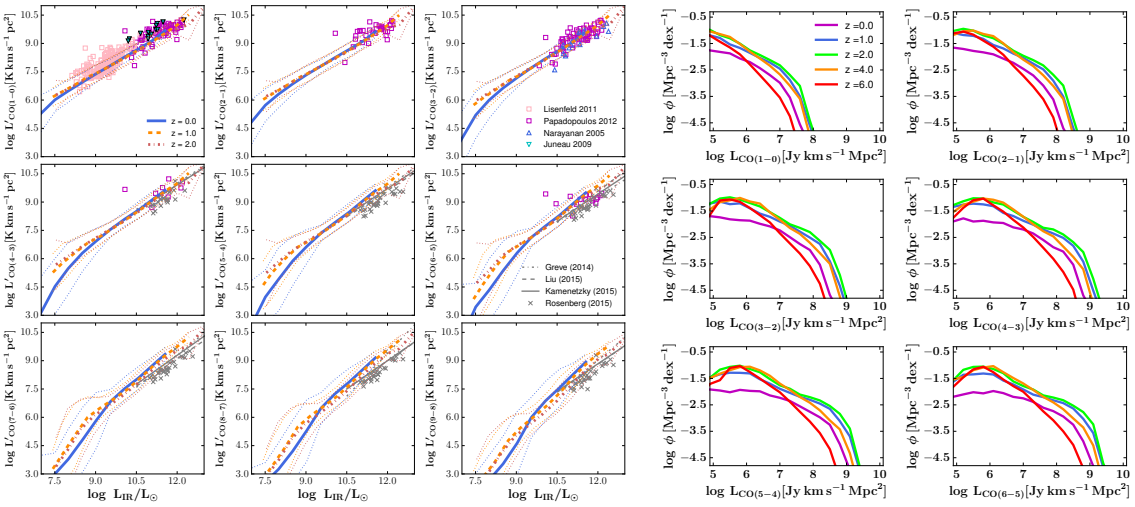

Figure 36. **Left** *CO line-luminosity of CO J=1-0 up to CO J=9-8 as a function of FIR luminosity at redshifts $z = 0$, $z = 1$, and $z = 2$. Model results are compared to observations taken from Narayanan et al. [252], Juneau et al. [253], Lisenfeld et al. [254],Papadopoulos et al. [255], Greve et al. [220], Liu et al. [256], Rosenberg et al. [257], and Kamenetzky et al. [258]. The thick lines show the median of the model predictions, whereas the dotted lines represent the two sigma deviation from the median.* **Right** *Model predictions of the CO J=1–0 up to the CO J=6–5 luminosity function of galaxies from $z = 0$ out to $z = 6$. Figures from Popping et al. [203] model. (Courtesy of Gergö Popping and Rachel Somerville)*

In summary, galaxy formation models have traditionally focused on predictions for the stellar properties of galaxies, such as UV-NIR emission. Recently, they have been extended to make detailed predictions for line emission such as CO and [CII]. It will be important to continue to validate and refine these models by confronting the predictions with deep observations of line properties for individually detected galaxies, as well as with the predictions of more detailed, spatially resolved numerical hydrodynamic simulations [e.g. 259]. With some additional effort, these tools can be adapted to provide detailed forecasts for intensity mapping, provide a testbed for developing new analysis tools, and to aid in the interpretation of upcoming experiments in terms of the constraints they can provide on the physics of galaxy formation and evolution.

5.1.6 High Resolution Numerical Hydrodynamic Simulations

High resolution numerical hydrodynamic simulations can be used to reproduce the observed stellar mass-halo mass relation and Kennicutt-Schmidt relation. The FIRE simulations, for example, are cosmological zoom-in simulations which are being used to make mock maps for the COMAP experiment.

Since CO gas is tightly correlated with molecular H_2, the technique described in Krumholz et al. [260] is first used to predict the molecular H_2 fraction as a function of the local gas column density and metallicity of gas. Then the model described in Narayanan et al. [261] is used to obtain CO luminosity as a function of the local molecular H_2 column density and metallicity of the gas. Contrary to previous studies in literature, the halo mass alone is found to not be a good indicator of the CO luminosity. As shown in Fig. 37, the CO luminosity varies by 3 dex over a time in which the halo mass varies by less than a factor of two. This shows that there is at least other physical parameter (besides halo mass) determining the CO luminosity of a given galaxy. The star-formation rate is strongly correlated with the CO luminosity. However, after accounting for the effect of the star-formation rate, one still observes 2 dex of fluctuations. Finding other hidden parameters which control the behavior of CO luminosity from a given halo is left to future work.

5.1.7 Modeling for Line-Intensity Mapping Cross-Correlations

Cross-correlations between different lines provide a number of exciting possibilities for intensity maps. In addition to allowing tests of systematics and foreground cleaning, they also make it possible to obtain significantly more information about a target population than can be learned from a single line alone. They can also allow access to lines far too faint to detect on their own. For an example, consider the cross-correlation between the usual 115 GHz ^{12}CO line and its 110 GHz ^{13}CO isotopologue discussed in Breysse and Rahman [262]. Figure 38 shows a schematic view of what the contributions to a survey from these two lines might look like. A given set of galaxies will emit both ^{12}CO and ^{13}CO lines at a given position in physical space. The two lines are then redshifted to different bands in frequency space as shown in the bottom two panels, then added together to produce the observed signal in the top panel. For illustration purposes, Figure 38 assumes that the observed ^{13}CO intensity from all galaxies is 10% of the ^{12}CO intensity.

The cross-spectrum of a pair of lines takes a similar form to those in the Introduction:

$$P_{1\times2}(k,z) = \overline{I}_1(z)\overline{I}_2(z)\overline{b_1}(z)\overline{b_2}(z)P_m(k,z) + P_{\rm shot}^{1\times2}, \tag{5.3}$$

where $\overline{I}_{1,2}$ and $\overline{b}_{1,2}$ are the mean intensities and biases of the two lines. The shot noise amplitude becomes

$$P_{1\times2}^{\rm shot} \propto \int_0^\infty L_1 f(L_1) \frac{dn_{\rm gal}}{dL_1} dL_1, \tag{5.4}$$

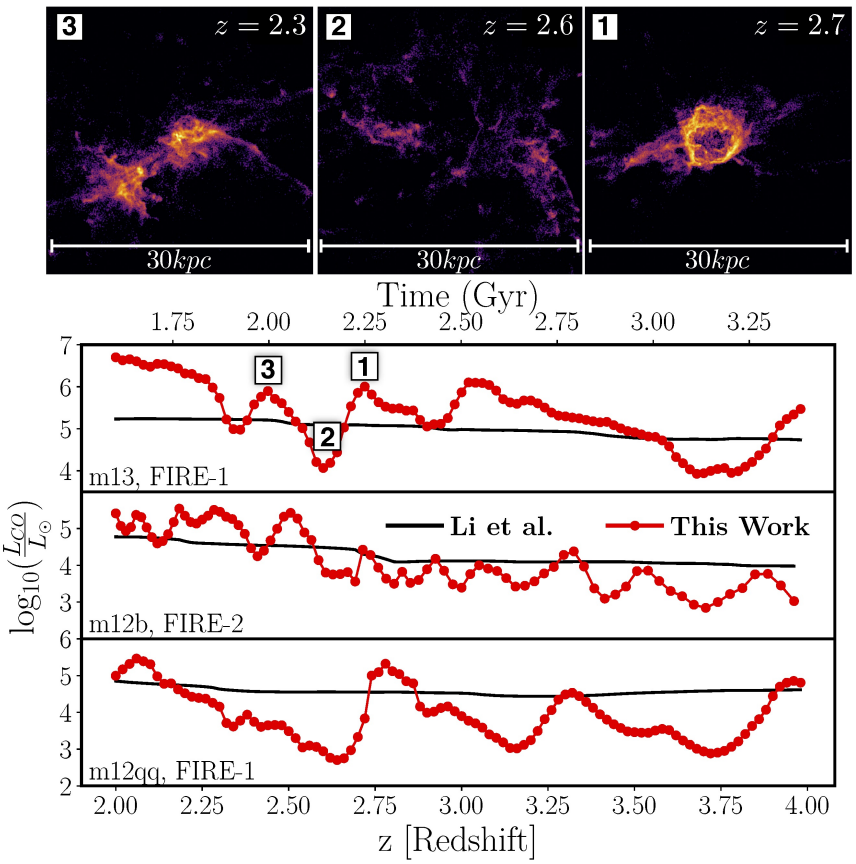

Figure 37. *CO Luminosity trajectories for three FIRE runs as a function of redshift. Top panel shows the* H_2 *column density from a halo with mass* $10^{12}\,M_\odot$ *at different redshifts (the halo mass is* $10^{13}\,M_\odot$ *at* $z = 0$*, hence the name "m13") which correspond to the* H_2 *emission before, during and after a gas blowout. FIRE-1 and FIRE-2 are different simulation runs. (Courtesy of Gunjan Lakhlani and Norman Murray)*

where it was assumed that $L_2 \equiv f(L_1)$. The cross-spectrum thus allows a measurement of the intensity ratio of the lines as well as how they vary with respect to one another from source to source. This gives it great potential as a tool to probe the high-redshift interstellar medium in great detail.

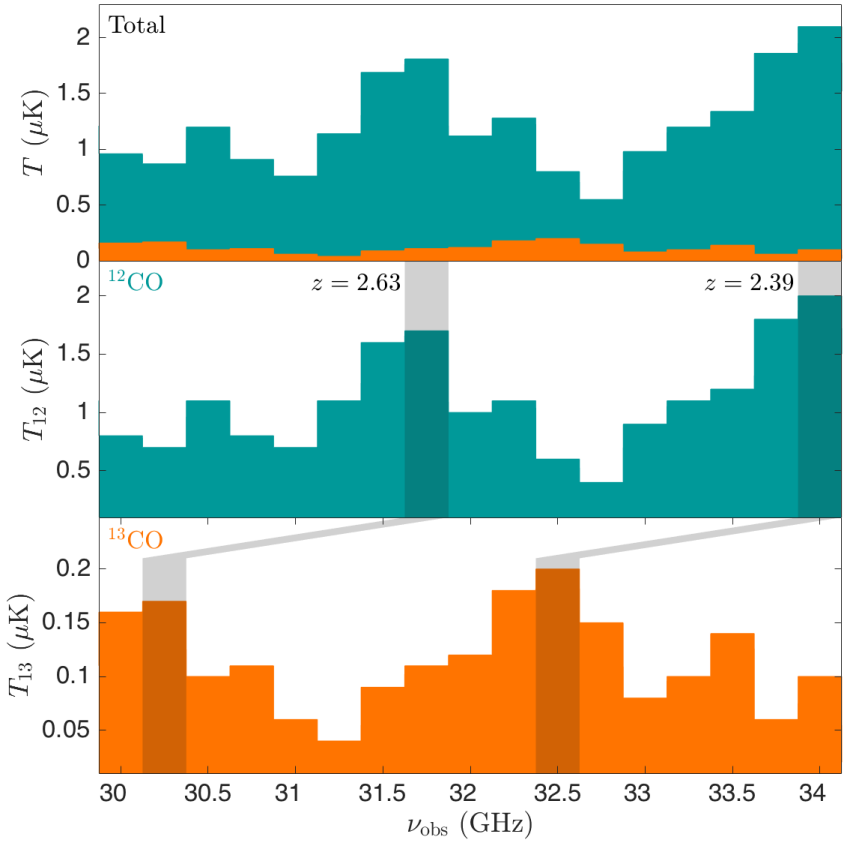

Figure 38. *A schematic view of the contributions from ^{12}CO and ^{13}CO to a hypothetical intensity mapping survey. The top panel shows the total observed intensity in each frequency bin assuming that the observed ^{13}CO intensity from all galaxies is 10% of the ^{12}CO intensity. The middle and bottom panels show the contribution to the total signal from ^{12}CO and ^{13}CO emission respectively. The shaded regions in these panels highlight emission that comes from the same slice of physical space. (Courtesy of Patrick Breysse)*

5.2 Techniques

A range of theoretical work is underway to further develop line-intensity mapping analysis and simulation techniques. These efforts aim to: identify interesting science targets for line-intensity mapping surveys and produce methods for extracting this science (§5.2.1 and §5.2.2), to develop rapid techniques for generating mock line-intensity mapping data cubes (§5.2.3), to optimize analysis methodologies (§5.2.4), and to explore strategies for foreground mitigation (§5.2.6). This work is important for sharpening the science case for line-intensity mapping, for planning upcoming survey efforts, in developing end-to-end simulations of analysis pipelines, and ultimately for interpreting the actual survey data as it becomes available. The subsections below provide the flavor of some current work in this area.

5.2.1 Studying Galaxy Evolution with Intensity Mapping Cross-Correlations

Line-intensity mapping data cubes may be cross-correlated with galaxy surveys, providing a reliable means of statistically detecting the cosmological matter distribution in datasets dominated by instrumental noise and systematic effects. The resulting cross-power spectrum, $P_x(k)$, depends on the bias factor of the optically selected galaxies, $b_{\rm gal}$, the neutral hydrogen bias, $b_{\rm HI}$, and the average HI brightness temperature, $\overline{T_{\rm HI}}$. It is therefore highly sensitive to the HI distribution and to how the sample of optical galaxies is selected. The cross-correlation coefficient, $r(k)$, expresses the intrinsic correlation of the two probes and is defined as $r(k) = P_x(k)\left[P_{\rm HI}(k)P_{\rm gal}(k)\right]^{-1/2}$.

As described in Section 3, the first cosmological detection of an HI intensity map was through cross-correlating redshifted 21-cm data from the Green Bank Telescope (GBT) at $z \approx 0.8$ [86] with an overlapping optically-selected galaxy sample from the WiggleZ Dark Energy survey [110]. Thus far, only upper limits have been obtained on the HI intensity mapping auto power spectrum from the GBT data [111], and so $r(k)$ has not yet been derived observationally. Nevertheless, the prospect of near-term measurements of $r(k)$ have motivated efforts to understand how this quantity may inform models of galaxy evolution.

First, simulations of the GBT-WiggleZ cross-correlation [263] found that the cross-correlation coefficient decreases on small scales around $k > 1.0$ Mpc^{-1}, and exhibits a varying shape, dependent on how the optical galaxies are selected. Specifically, the WiggleZ selected galaxies are highly star-forming and usually HI-rich and show a much higher correlation on small scales than quiescent, red galaxies. In further theoretical studies, this effect has been traced back to a previously unaccounted-for shot-noise contribution to the cross-correlation power spectrum which scales with the HI content of the optically selected sample [89]. The scale-independent shot-noise contribution is caused by Poisson noise in the discrete galaxy sample, which in cross-correlation with the HI maps is weighted by the average HI temperature of the sample, such that $P_{\rm shot} = \overline{T_{\rm HI,gal}}/N_{\rm gal}$. The observed cross-correlation coefficient $\hat{r}(k)$ can be rewritten as $\hat{r}(k) = \left(P_x(k) + P_{\rm shot}\right)\left(P_{\rm HI}(k)P_{\rm gal}(k)\right)^{-1/2}$. Measuring the cross shot-noise contribution either in $\hat{r}(k)$ or $P_x(k)$ allows one to determine the average HI mass of the selected galaxy sample from $\overline{T_{\rm HI,gal}}$. In other words, one can establish scaling relations between the selection criteria of the optical samples and their HI mass.

Fig. 39 shows an example of how the average HI mass relates to the optical color selection $(u-g)$, which indicates the level of star-formation activity in a galaxy. These results are derived from the hydro-dynamical EAGLE simulation at redshifts $0 < z < 3.5$ [265]. The HI mass of each simulated galaxy is given in del P Lagos et al. [264]. The solid lines indicate the true HI mass and color extracted directly from the simulation, while the circles mark the values derived from the shot-noise contribution to the simulated cross-correlation power spectrum. This illustrates how the cross-correlation between intensity maps and optically selected galaxy samples may be used to derive scaling relations between the gas contents and star-formation properties of the samples, and thereby provide insight into universal laws governing galaxy evolution.

5.2.2 Complementing 21cm Probes of the EoR with other Line-Intensity Mapping Surveys

Line-intensity mapping observations may potentially be used to trace large scale structure in the galaxy distribution during the EoR, and thereby complement redshifted 21-cm observations of intergalactic neutral hydrogen from the same epoch. Reionization involves the interplay between the ionizing sources – which are likely abundant, low mass galaxies – and intergalactic hydrogen. Stated generally, our understanding of

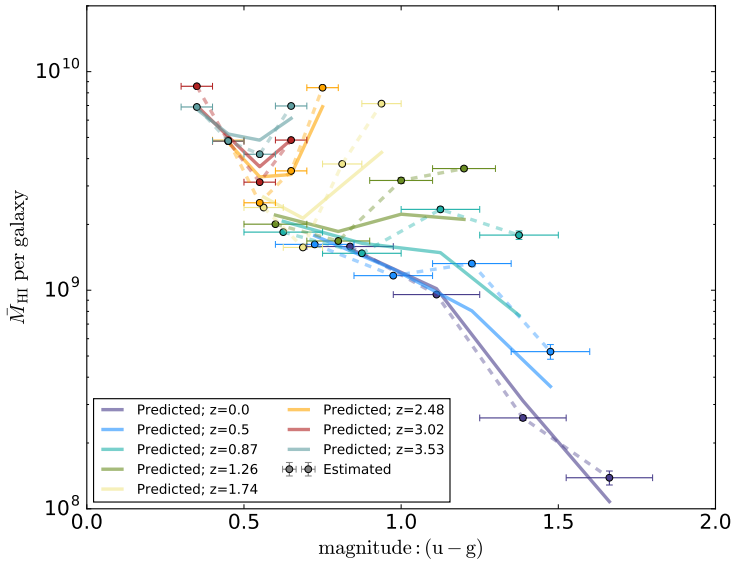

Figure 39. *Extracting galaxy properties from cross shot-noise measurements. The average HI mass per galaxy sample, as selected by their color $(u-g)$ (moving from blue to red in the increasing direction along the x-axis) for redshifts from $0 < z < 3.5$. A $(100\mathrm{Mpc}/h)^3$ volume EAGLE simulation box is used with HI masses provided by del P Lagos et al. [264], based on the Gnedin-Krumholz scheme. The solid lines indicate the true scaling relation from the simulation output, while the dashed lines with circles show the values obtained through the cross shot-noise measurements. See Wolz et al. [89] for a more detailed description of the method. (Courtesy of Laura Wolz)*

reionization should therefore benefit from tracking both the intergalactic gas (through the 21-cm line) and the sources themselves (using other convenient emission lines).

More concrete synergies may also be identified. For example, cross-correlating a 21-cm data cube with emission in another line at the same redshift may help to verify a putative redshifted 21-cm detection [10, 266, 267]. A significant challenge for 21-cm measurements from the EoR is to separate strong foreground contamination, and it may initially be tricky to distinguish a genuine cosmological signal from residual foreground contamination. A smoking-gun validation would be to show that the putative 21-cm signal correlates with another high redshift tracer of large-scale structure. This, however, requires an additional probe which spans a large field of view, yet has accurate redshift information.[2] Although high redshift galaxy surveys with the JWST or ALMA, for example, will provide valuable information about early galaxy populations, they are poorly suited for direct cross-correlation with 21-cm measurements given the $\sim$ arcminute fields of view of these instruments. A more promising approach for cross-correlation purposes is to give up on detecting individual sources, and to focus instead on measuring the spatial fluctuations in the combined emission from many individually unresolved galaxies in convenient tracer lines (e.g. Lidz et al. [10], Gong et al. [268]). In other words, one can perform line-intensity mapping observations – using various

[2] A survey with coarse photometric redshift estimates measures mainly transverse modes, but these spectrally-smooth modes are hardest to separate from foregrounds in the 21-cm survey. In order to be well-matched to the 21-cm survey, accurate redshifts are required of the "tracer" survey.

emission lines – to trace-out galaxy populations across the same large cosmic volumes in which the 21-cm surveys track neutral hydrogen.

Fig. 40 illustrates how a hypothetical CO(2-1) line-intensity mapping survey might be fruitfully combined with 21-cm measurements.[3] On large scales, the CO(2-1) emission should be anti-correlated with the 21-cm signal: bright areas in the CO map trace upward fluctuations in the galaxy abundance but these regions are ionized and dim in 21 cm. On the other hand, the 21-cm and CO fields should be roughly uncorrelated on scales much smaller than the size of the ionized regions. This occurs because the gas interior to ionized regions is highly ionized irrespective of the precise galaxy abundance, while completely neutral regions do not contain galaxies (see Lidz et al. [10, 267] for further discussion and model variations). Fig. 41 shows this more quantitatively, plotting the cross-correlation coefficient between the model CO(2-1) and 21-cm fields. In short, the cross-correlation may be used to determine the typical size of ionized bubbles at different stages of the reionization process.

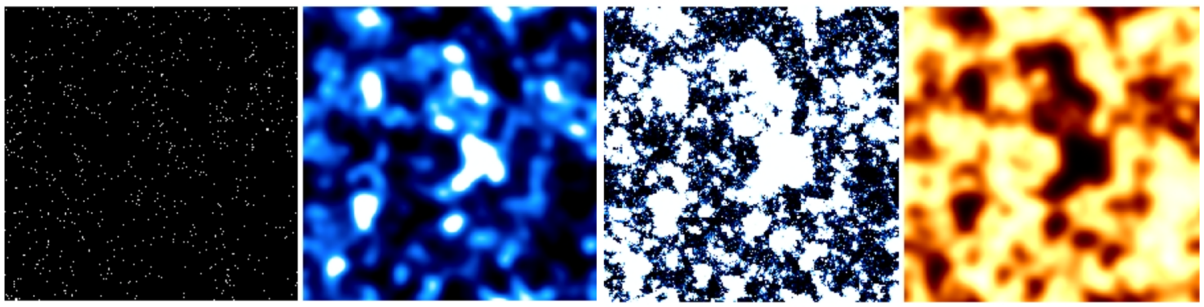

Figure 40. *Complementing redshifted 21-cm observations of the EoR with intensity mapping observations in other lines.* ***Panel 1****: The simulated distribution of EoR galaxies.* ***Panel 2****: A model for the CO(2-1) line-intensity mapping signal from these galaxies.* ***Panel 3****: The ionization field from the simulation slice. The white regions are highly ionized, while the dark regions show neutral hydrogen.* ***Panel 4****: The redshifted 21-cm signal from the same region of the IGM. Each simulation slice is* 130 *co-moving Mpc/h on a side (spanning roughly a degree across on the sky), and* 0.25 *Mpc/h thick. The CO(2-1) and 21-cm maps are smoothed to* 6 *arcminute spatial resolution and* 0.035 *GHz spectral resolution. On large scales, the CO and 21-cm fields are anti-correlated. This large scale anti-correlation may be used to confirm a possible redshifted 21-cm detection, and to help understand the properties of cosmic reionization. (Courtesy of Adam Lidz)*

In addition, line-intensity mapping observations may provide valuable information about the bulk properties of galaxy populations during the EoR. This may be especially valuable given recent observations, which suggest that reionization is driven largely by abundant, low luminosity galaxies (e.g. Robertson et al. [269]). These faint sources are challenging to detect individually, but their collective impact may nevertheless be studied with line-intensity mapping observations. The key issue that requires further quantitative study, however, is just how luminous the bulk of the ionizing sources – which may be quite metal poor – are in convenient tracer lines. Targeted ALMA observations may provide valuable guidance here, which can then sharpen line-intensity mapping forecasts. If line-intensity mapping observations are possible in multiple lines, and the relative strength of emission fluctuations in the different lines is measurable, this should help elucidate the bulk ISM properties in early galaxy populations.

[3]Note that CO(2-1) provides just one illustrative example transition and other lines such as [CII] may, in fact, be superior for mapping galaxy populations during the EoR (e.g. Gong et al. [2]).

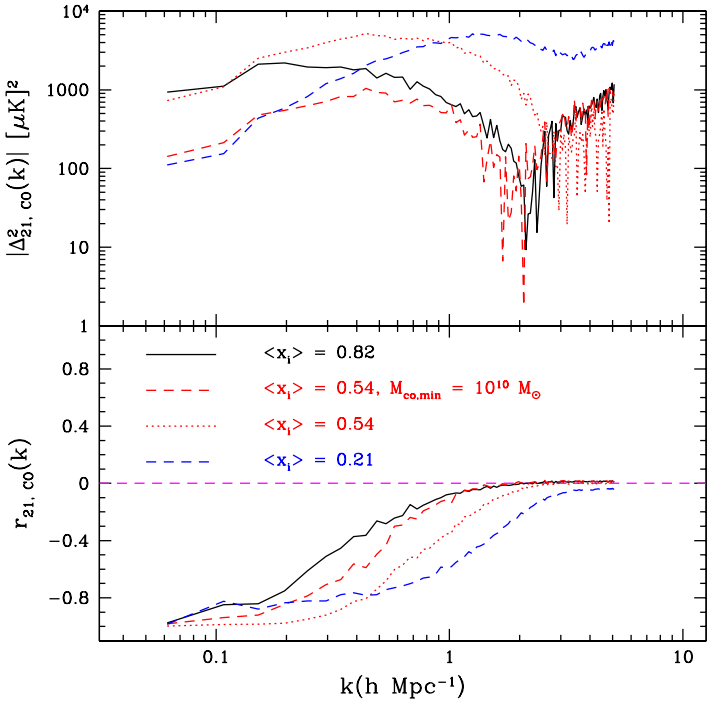

Figure 41. *Cross-correlation between CO(2-1) and 21-cm brightness temperature fluctuations during the EoR.* ***Top Panel****: The absolute value of the cross power spectrum between the fluctuations in each line at different stages of the reionization process. The quantity* $\langle x_i \rangle$ *in the legend refers to the volume-averaged ionization fraction.* ***Bottom Panel****: The cross correlation coefficient between the two fields. On scales larger than the characteristic size of the ionized regions at the redshift of interest, the cross-correlation coefficient approaches* $r_{21,\mathrm{CO}} \sim -1$*, while it goes to zero on significantly smaller scales. As reionization proceeds, a progressively larger fraction of the IGM volume is ionized, and the typical size of the ionized regions increases. The cross-correlation hence turns over at smaller and smaller wavenumber with increasing* $\langle x_i \rangle$*, charting the overall progress of reionization. From Lidz et al. [10]. (Courtesy of Adam Lidz)*

5.2.3 Developing Mock Line-Intensity Mapping Surveys

Mocking line-intensity mapping experiments requires accurate large scale structure simulations. N-body methods work well for a subset of these simulations [98], but when larger cosmological volumes or many independent realizations are needed, more efficient methods are required. Examples include studying map-to-map covariances and cosmological parameter variations, especially for efforts to explore physics beyond the standard model of cosmology (e.g., primordial non-Gaussianity, dark energy, and modified gravity).

To create mocks for COMAP the mass-peak-patch method for finding halos is used, based on ellipsoidal dynamics applied to Lagrangian (initial condition) regions defined by collapse along all three axes [270]. The speed of this method allows an 1140^3 Mpc^3, $2.4 < z < 3.4$, $n_{cell} = 4096^3$ simulation to be completed in only 580 CPU hours using 2.3Tb of memory on 2048 Intel Xeon E5540 2.53 GHz processors of the Scinet General Purpose Cluster. The resulting halo catalogs, with a minimum mass of $2.5 \times 10^{10} M_\odot$, are used to generate a multi-frequency realization of the observed line intensity by assigning a CO(1-0) flux to each halo, using properties such as mass, redshift, and formation time. Given the COMAP resolution, equivalent maps would be obtained without using an HOD model for central and satellite galaxies in the halos. The final mock intensity map is created by binning the resulting halo fluxes by angular position and observed frequency, including redshift space distortions, using publicly available code[4].

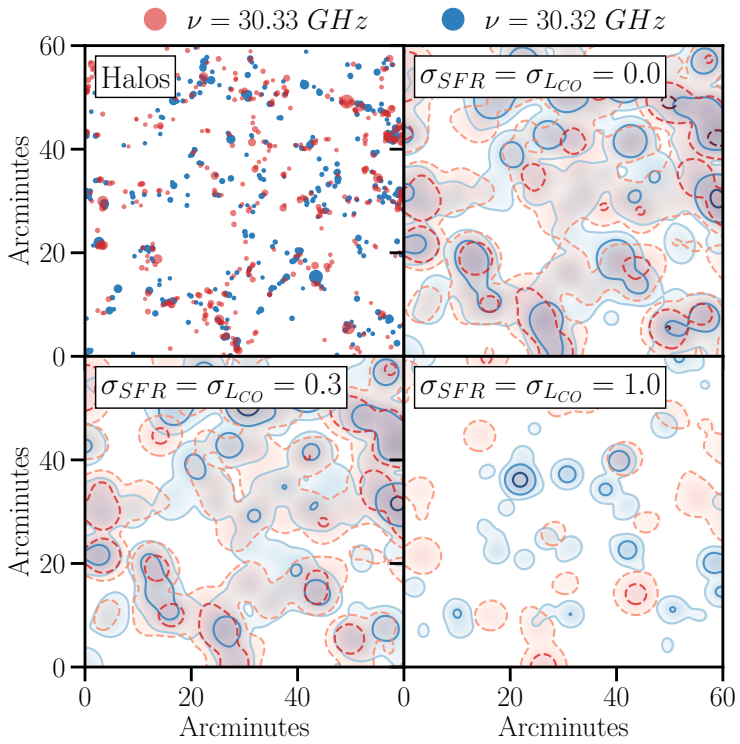

Figure 42. *COMAP mocks created using a peak patch lightcone halo catalogue for the standard model of cosmology, ΛCDM. The cosmological parameters and $L_{CO}(M_{halo}, z)$ model are the same as assumed in Li et al. [98].* ***Top Left****: Dark matter halos in two neighboring COMAP frequency slices (corresponding to CO(1-0) emission redshifts of $z = 2.800, 2.801$) are shown to illustrate the level of slice-to-slice correlations. An HOD model is used to treat central and satellite galaxies.* ***Top Right****: CO(1-0) emission smoothed with a beam of FWHM=4′ . Contours correspond to brightness temperature thresholds of $T_{CO} = 0.1\mu K$, $1\mu K$, and $10\mu K$.* ***Bottom Left****: A log-normal scatter of 0.3 dex on the $SFR(M_{halo}, z)$ and $L_{CO}(L_{IR})$ relations is adopted, as in Li et al. [98].* ***Bottom Right****: The effect of increasing the log-normal scatter to 1.0 dex, more in line with the scatter measured in FIRE gasdynamical simulations. This scatter is primarily a consequence of the bursty nature of star formation, but a proper study of correlations among the variables defining L_{CO} is still in progress. These maps were created with the publicly available code github.com/georgestein/limlam_mocker. (Courtesy of George Stein and J. Richard Bond)*

[4]github.com/georgestein/limlam_mocker

This technique has been used to create thousands of independent realizations covering the COMAP survey volume, which each consist of a 1140 Mpc comoving line of site depth, covering a 90 deg^2 field of view. Initially COMAP plans to survey a few $\sim$ 2 deg^2 regions, but the simulations cover a much larger region of the sky with the given minimum mass resolution. Example results are shown in Fig. 42. One can see the cosmic web revealed, and so additional statistical measures beyond the traditional power spectrum are needed to fully describe the maps. For example, one can consider the $P(\{D, z\})$ statistic, a generalization of the classic radio astronomy one-point measure generalized to tomography, and applied to CO mapping by Breysse et al. [271] (which is discussed in more detail below), stacking on peaks, etc. This is especially important given the large sample variance for such small patches. Fig. 42 also illustrates the importance of (uncorrelated) scatter in the $L_{CO}(M, z)$ relationship. The same mock methods have been applied to HI intensity mapping for surveys such as CHIME and HIRAX, covering much larger volumes (although at much lower resolution), while [CII] intensity mapping mocks are underway.

5.2.4 Line-Intensity Mapping Analysis Methods

Constructing an Optimal Observable

It is interesting to consider in which regimes line-intensity mapping is advantageous to a "traditional" survey mode, where one considers catalogs of the individual objects that are robustly detected in a survey. Of course upcoming survey data may ultimately be analyzed using an intensity mapping approach as well by cataloging individual objects, but it is still valuable to identify the optimal technique for achieving a given scientific goal.

The intensity mapping method includes the information from all faint sources below the detection limit, by measuring the total emission from a (large) pixel (or voxel in 3D). In contrast, a traditional survey uses high angular resolution to pick out the bright sources, applying a thresholding operation to the pixels or voxels. These two distinct approaches can be described by a unified "observable" function $\hat{O}(L)$. In both cases, a "map" is created by applying $\hat{O}(L)$ on a voxel-by-voxel basis. In the galaxy detection methodology, the signal in a voxel is labeled as a "detection" if it is brighter than a threshold luminosity L_{th} (say 5 times the rms noise for a 5σ detection). The underlying density distribution is then encoded in this "digital map", consisting of 1's (detections) and 0's (non-detections), and cosmological constraints can be extracted from the power spectrum of this map. Therefore, in the galaxy detection case, $\hat{O}(L)$ is a step function with the step at L_{th} . On the other hand, intensity mapping takes the power spectrum of the measured intensity (or luminosity) map directly, so the observable is a linear function of L, $\hat{O}(L) = L$.

In Cheng et al. 2017 (in prep.), the authors generalize the line-intensity mapping formalism by seeking the "optimal observable", $\hat{O}_{opt}(L)$, which is optimal for measuring the underlying density field for a given survey design and source population. The optimal observable can be derived from the probability distribution of the total luminosity in a voxel, $P(L)$, and its dependence on the underlying density. The key quantity distinguishing the line-intensity mapping and galaxy detection regimes is the effective number of sources per voxel, $N_{\rm eff}$. Fig. 43 shows that the optimal observable is indeed very close to the line-intensity mapping and galaxy detection scenarios for $N_{\rm eff} > 1$ and $N_{\rm eff} < 1$, respectively. The source population is assumed to follow the Schechter form and different levels of Gaussian (instrumental) noise, σ_L, are considered. In the low $N_{\rm eff}$ regime (**Top Panels**, with $N_{\rm eff} = 7 \times 10^{-4}$), the optimal observables are similar to step functions with the steps at a few times σ_L, which is the traditional thresholding/galaxy detection approach; while in the large $N_{\rm eff}$ scenario (**Bottom Panels**, with $N_{\rm eff} = 3$), the optimal observable function is approximately linear over a wide range of L. This result justifies the usage of the line-intensity mapping approach in the highly confused limit. Moreover, Cheng et al. 2017 (in prep.) also identify scenarios where intermediate

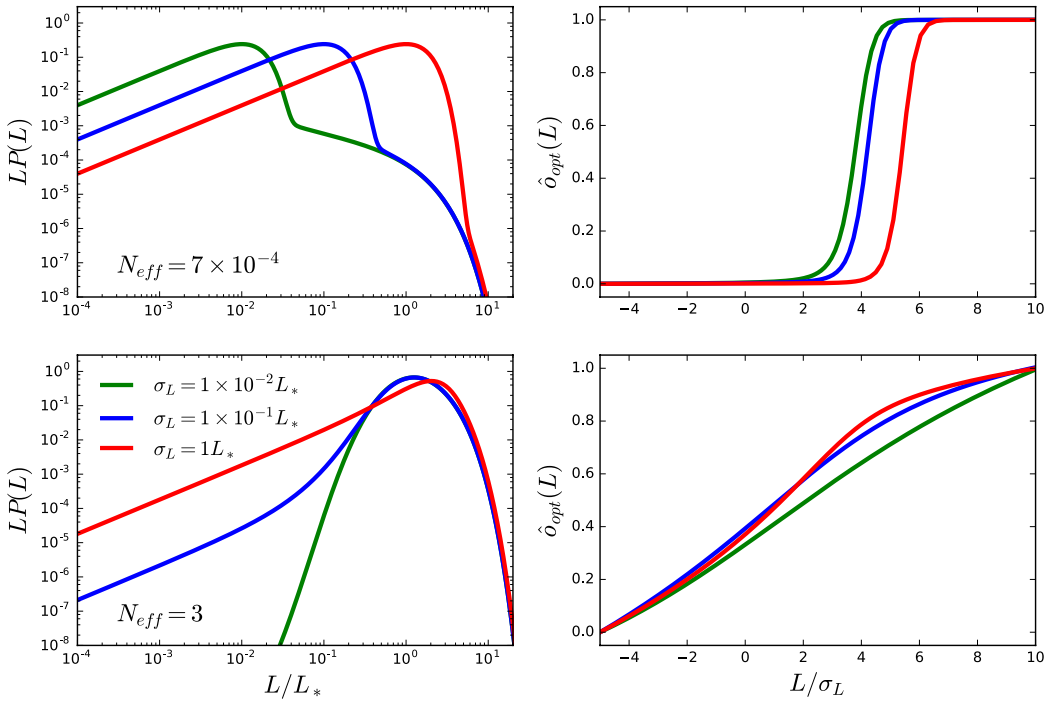

Figure 43. *Identifying the optimal observable. The probability distribution of total voxel luminosity (**Left Panels**) and the optimal observable/weight function (**Right Panels**) for a low (**Top Panels**) and high (**Bottom Panels**) effective number of sources per pixel, $N_{\rm eff}$. The colors indicate different levels of Gaussian instrumental noise, σ_L. In the low $N_{\rm eff}$ regime, the optimal observable is close to a step function, corresponding to the detection of bright sources, whereas in the high $N_{\rm eff}$ regime, the optimal observable is close to a linear function of L, corresponding to intensity mapping. (Courtesy of Yun-Ting Cheng)*

estimators are optimal; i.e., in these cases neither pure line-intensity mapping nor galaxy detection analysis strategies are ideal.

5.2.5 Multi-Tracer Analysis

A promising strategy to overcome the limits imposed by systematics and sample variance is to perform *multi-tracer* analyses, whereby two differently-biased tracers of large-scale structure are combined in such a way that sample variance is cancelled from the noise terms for some combinations of bias-dependent terms [272]. The cross-correlation of multiple tracers should also significantly reduce many systematic effects, which tend to be uncorrelated between surveys. These methods should be fruitfully applied using various future line-intensity mapping survey data sets, both in conjunction with each other, and when combined with traditional galaxy surveys. For example, recent studies have found that post-reionization 21-cm intensity mapping surveys are well-matched to large optical surveys like LSST and Euclid [69, 70]. These analyses should help probe the

power spectrum on ultra-large scales, which in turn may be used to test General Relativity and to search for possible signatures of primordial non-Gaussianity (see §2 and references therein).

Furthermore, on large scales a key quantity of interest for line-intensity mapping is the product of the average specific intensity $\langle I(z)\rangle$ and a luminosity-weighted bias factor, $b(z)$ (see Eq. (1.1)). Determining this quantity from cross-correlating a line-intensity map with a traditional galaxy survey is more akin to template fitting than power spectral estimation, and so this can be done without sample variance [164]. In surveys of the cosmic microwave background, a common strategy is to map each mode to SNR = 1 [273]. Time is better spent integrating a larger number of modes rather than having high signal-to-noise on a mode that is ultimately limited by sample variance. In contrast, determination of the amplitude through cross-correlation could pursue deeper surveys with fewer modes. Hence, the possibility of carrying out multi-tracer analyses has important implications for the design of line-intensity mapping surveys.

P(D) analysis

The primary statistic used to date when discussing intensity maps is the power spectrum, $P(k)$. The power spectrum is the Fourier transform of the two-point correlation function, and is thus a two-point statistic. As seen throughout this document, it is a very powerful tool for studying cosmological density fields. However, it suffers from a key limitation: all of the information about a random field is contained within its power spectrum if and only if the field is perfectly Gaussian. The small-scale fluctuations in an intensity map are expected to be highly non-Gaussian, as the measured intensity is the product of highly nonlinear processes within the galaxy population. Thus, the power spectrum alone misses out on much of the information content of a map. This is illustrated in the left two panels of Fig. 44, where applying Eq. (1.1) to two very different luminosity functions gives identical power spectra.

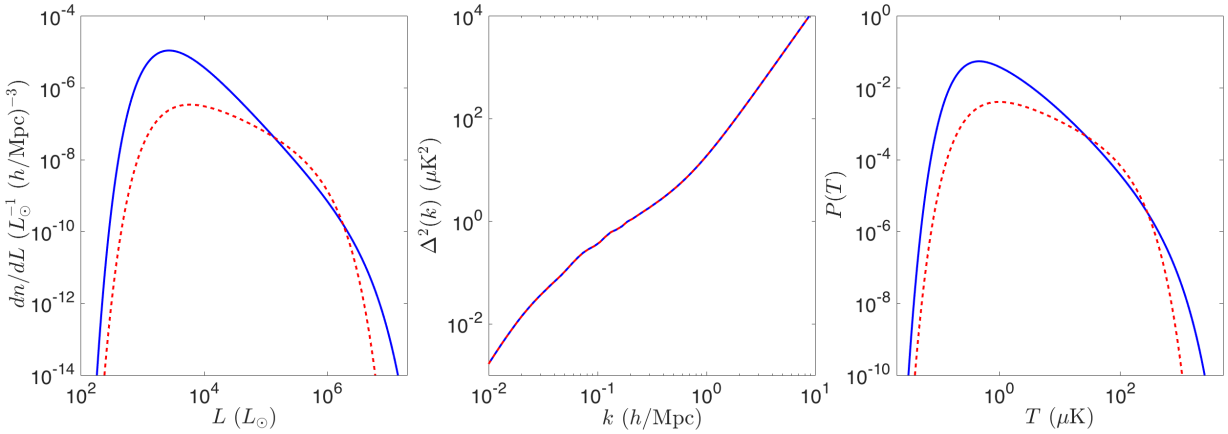

Figure 44. *Importance of statistics beyond the power spectrum and VIDs.* ***Left Panel****: Two generic luminosity functions for a hypothetical line, each with the modified Schechter form from Breysse et al. [271]. The red dashed curve is chosen to have five times fewer total emitters than the blue.* ***Center Panel****: Power spectra computed for the two luminosity functions in the left panel. Parameters of the two Schechter functions were chosen so that these two power spectra are identical (for the purposes of this illustration, both spectra were assigned the same average bias factor). An infinite number of other luminosity functions would also give the same spectrum.* ***Right Panel****: VIDs for the two luminosity functions. Though the two functions have the same power spectra, they can be distinguished by their VIDs. (Courtesy of Patrick Breysse)*

One possibility for accessing this extra information is to look additionally at the one-point statistics of a map. Breysse et al. [96] and Breysse et al. [271] propose to do this using $P(D)$ analysis methods, which were originally developed for radio astronomy [274] but have since been applied to observations across the electromagnetic spectrum (see, for example, Barcons et al. [275], Windridge and Phillipps [276], Lee et al. [277], Patanchon et al. [278]). $P(D)$ analysis provides a means of mapping the underlying luminosity function of a source population onto the observed histogram of voxel intensities (termed the Voxel Intensity Distribution, or VID by Breysse et al. [271]). By doing so, one can measure the full shape of the luminosity function, rather than simply the first two moments (see the right-hand panel of Fig. 44). Intensity mapping is particularly well-suited to this type of analysis for two reasons. First, the distances to the target sources are known, which allows one to infer the distribution of their intrinsic luminosities, while most $P(D)$ studies are limited to flux distributions. In addition, because intensity maps are inherently three-dimensional, sources can be localized into small voxels rather than 2D pixels which span the full line-of-sight. This lessens confusion caused by having many sources in each pixel.

Breysse et al. [271] applied $P(D)$ analysis to a CO(1-0) luminosity function model with a similar shape to that of Li et al. [98]. Fig. 45 compares the constraints on the luminosity function obtained using the power spectrum (shown in grey) to those using the VID (shown in blue). The power spectrum estimates assume much stronger priors than the VID estimates, but the VID produces a considerably tighter constraint. Both of these error bands make strong assumptions about the exact form of the luminosity function, and both neglect complications from foregrounds and systematics, and therefore should not be taken as an exact forecast of instrumental constraining power. However, Fig. 45 does make clear the advantage of VID methods over the power spectrum when measuring luminosity functions. Breysse et al. [271] go on to demonstrate the effectiveness of the VID in the presence of line and continuum foregrounds as well as gravitational lensing. $P(D)$ techniques appear to be a promising tool for extracting astrophysical information from intensity maps.

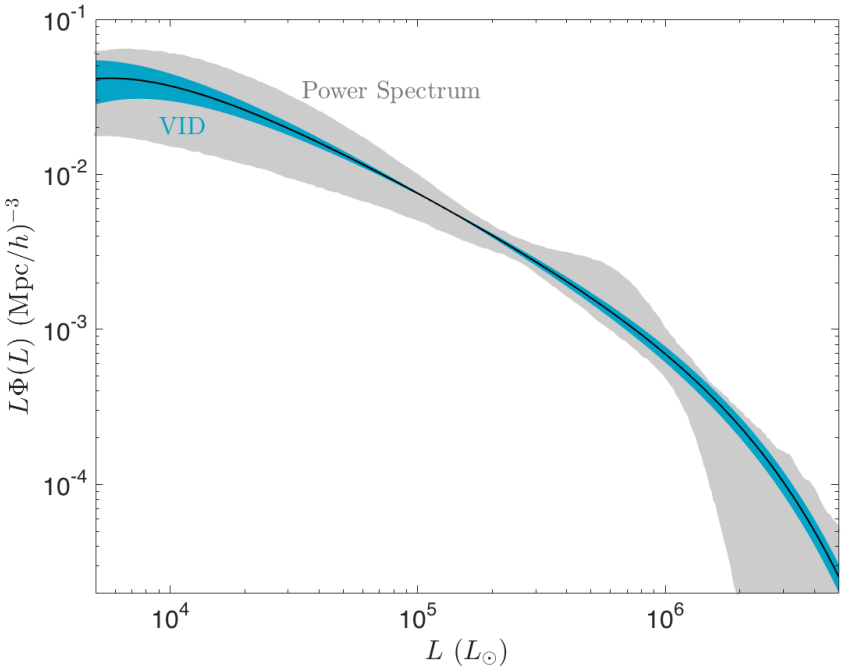

Figure 45. *Forecasted VID constraints on the CO(1-0) luminosity function. The shaded regions show forecasted 95% confidence regions around a model CO luminosity function using the VID (blue) by Breysse et al. [271] and using the power spectrum (gray) by Li et al. [98]. (Courtesy of Patrick Breysse)*

5.2.6 Foreground Contamination and Interloper Lines

It is helpful to divide the foreground contamination problem for line-intensity mapping surveys into the case of continuum foregrounds from, e.g. synchrotron radiation or thermal emission from dust grains, and that of line emission foregrounds. Strategies for mitigating the continuum foregrounds have been well developed for the case of 21-cm intensity mapping, and these should carry over for surveys in other emission lines of interest as well. The main idea here is that the continuum foregrounds are spectrally smooth, while the line emission signal — although generally much lower in amplitude than the continuum foregrounds — has a great deal of spectral structure. Consequently, the continuum foreground contamination is confined to Fourier modes with small line-of-sight wavenumbers, unlike the signal itself, and this feature can be used to avoid or excise the contamination.

One complication here is mode-mixing from the frequency dependence of the instrumental beam. The instrumental response inevitably moves spectrally smooth contamination into other regions of Fourier space. However, 21-cm studies have accounted for mode-mixing effects and shown that the continuum foregrounds nevertheless corrupt only a well-defined "wedge" shaped region in the $k_{\parallel} - k_{\perp}$ plane. Here $k_{\parallel}$ denotes the line-of-sight component of the wavevector, $\boldsymbol{k}$, while $k_{\perp}$ labels the magnitude of components in the plane of the sky. A conservative analysis strategy is simply to excise the foreground corrupted wedge, and measure statistics in the remaining part of Fourier space. Although the details will depend on the specifics of each survey, this basic approach should be broadly applicable across different line-intensity mapping surveys.

A more challenging issue for surveys targeting emission lines such as CO, Ly-α, and [CII], for example, is line confusion: in general, multiple "interloper" line transitions from gas at various redshifts may overlap in observed frequency with that of the "target" line at the redshift of interest (e.g. Visbal and Loeb [198]). Consider the interesting example case of a [CII] intensity mapping survey at a target redshift of $z_t = 7$, corresponding to an observed frequency of $\nu_{\rm obs} = 238$ GHz. Here important interloper lines include CO(3-2) from $z = 0.45$, CO(4-3) at $z = 0.88$, CO(5-4) at $z = 1.4$, and CO(6-5) at $z = 1.8$. Indeed, the spatial fluctuations in the combined emission from these CO transitions may exceed that from the [CII] emission of interest [122, 201]. Unlike the continuum foregrounds, the interloper contamination will obviously have a great deal of spectral structure, and so a different approach is required to avoid or excise it. Note, however, that interloper contamination is *not* expected to be an issue for redshifted 21-cm surveys, simply because there are few conceivable emission lines at the low frequencies of interest for these surveys. Below we discuss several different strategies for removing or avoiding interloper contamination.

Blind Bright-Voxel Masking

The first approach is to mitigate interloper contamination by masking out the brightest voxels in a survey. This technique is motived, in part, by the fact that important interloper lines generally come from gas at significantly lower redshifts than the target lines. Since galaxy masses tend to grow with decreasing redshift, one expects there to be more very bright sources of emission in the interloper lines than in the target line. This means that the brightest voxels in a survey are often sourced by foreground galaxies; the foreground contamination can be removed or reduced by masking out the bright voxels.

This method, the blind masking of bright voxels to mitigate line foregrounds, is investigated in [14]. Using empirical luminosity function models and simulated intensity maps these authors quantify how masking changes the simulated power spectra for three cases: CO(1-0) contaminated with HCN, Ly-α contaminated with various atomic lines, and [CII] contaminated with higher order CO lines. As demonstrated in Fig. 46, for the CO survey, the foreground line emission is faint enough on average that removing the brightest voxels significantly drops the amplitude of the foreground spectrum. In fact, this model makes pessimistic

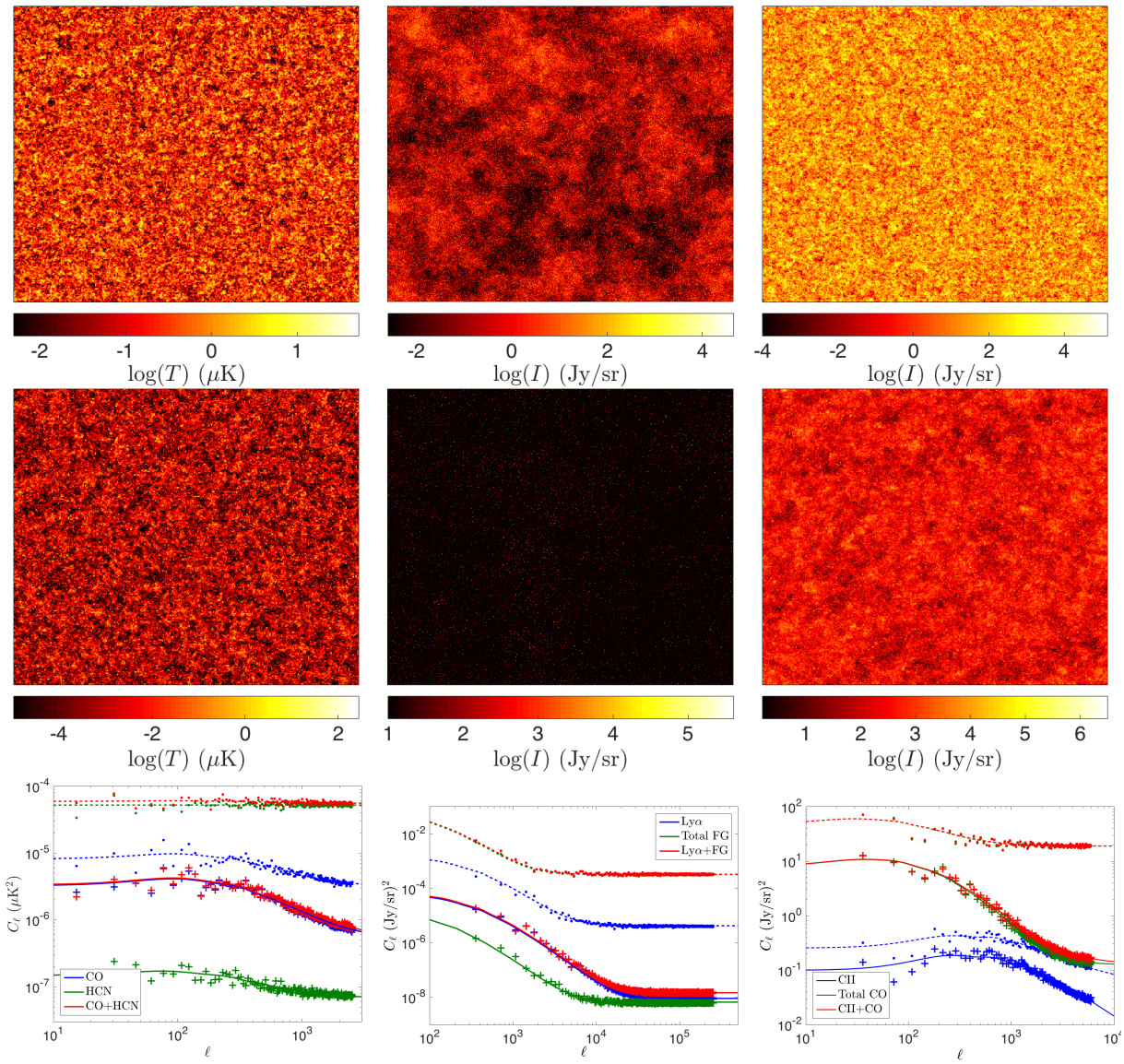

Figure 46. *Cleaning interlopers by bright voxel masking.* ***Top panels:*** *Simulated maps of CO(1-0) at $z = 3$, Ly-α at $z = 7$, and [CII] at $z = 7$ (top row, left to right) along with their foregrounds (middle row). The CO simulations cover 550 deg^2 with 10 arcmin resolution, the Ly-α simulations cover 1 deg^2 with 0.1 arcmin resolution, and the [CII] simulations cover 100 deg^2 with 3.2 arcmin resolution.* ***Bottom panels:*** *Power spectra and best fit curves for each of the signals in the simulated maps above (blue), the total corresponding foreground contribution (green), and the total emission (red). Dashed curves/dots show the spectra before masking, solid curves/pluses show the results after masking all voxels brighter than 1%, 3% and 1% of the voxels in the total emission map. For both CO and Ly-α, the masking removes a large fraction of the foreground contamination. In the case of [CII] at EoR redshifts, however, the foregrounds continue to dominate over the signal regardless of the masking percentage. (Courtesy of Ely Kovetz and Patrick Breysse)*

assumptions about the brightness of the HCN foreground (see also Fig. 48), yet bright pixel masking is still quite efficient. The high angular resolution in the Ly-α survey limits the foreground contamination to a few voxels, which can be easily masked. The [CII] survey, however, has both bright foregrounds and large voxels, and so blind masking is found to be ineffective.

For each emission line considered, masking bright voxels alters the recovered power spectrum from its input, uncorrupted form. This means that masking removes some of the information in the spectrum. However, in the two surveys where masking is effective, the *shape* of the clustering component of the power spectrum is preserved after masking. Therefore, though much of the *astrophysical* content of the map is lost, the *cosmological* information contained in the shape of the clustering spectrum can still be recovered from a masked map. Thus, voxel masking seems to be a useful technique for obtaining information from even a highly contaminated CO or Ly-α map. If one is to obtain the remainder of the information in these surveys, it will be necessary to use some other foreground cleaning technique, such as cross-correlation, or to augment it with a P(D) analysis of the progressively masked survey. If one is to fully unlock all of the benefits of line-intensity mapping surveys, it is imperative that one utilizes these or other methods to isolate the signal from the foregrounds.

Targeted Masking

Another approach, "targeted masking", uses existing (e.g. optically selected) galaxy catalogs at the redshifts of suspected interloper lines to identify which survey voxels to mask. This strategy has been studied for use in [CII] and Lyα surveys (see Silva et al. [5], Silva et al. [122]) and is being developed by the TIME project to mask-out CO interloper emission that lands in their observing band. The brightest CO lines in the TIME band come from CO transitions with upper rotational levels of $J_{\rm upper} = 3 - 6$ from galaxies at $z < 3$.

This approach requires catalogs of likely interloping galaxies with accurate redshift information. TIME plans to observe patches of the sky that have good observational coverage in multiple wavelength bands, and to supplement existing catalogs by obtaining additional spectroscopic redshifts using MOSFIRE or another similar instrument. Targeted masking should be efficient provided the galaxy catalogs obtained contain good observable proxies for the CO interloper emission. The details of this methodology, including uncertainties arising from scatter in the relation between CO emission and the properties of catalog galaxies, are discussed in Sun et al. [279].

Anisotropic Power Spectrum Method

An additional technique for separating out the interloper contamination exploits the redshift dependence of the mapping between observed frequency and angular separation on the sky into co-moving spatial scales [7, 198, 201, 280]. If one assumes the target redshift in performing this mapping, then the interloper emission fluctuations are mapped to the wrong spatial scales. Specifically, consider interloper emission at redshift z_i contaminating a survey for line emission at redshift z_t. Further, let us denote the apparent co-moving line of sight coordinate of this interloper emission by $\tilde{x}_\parallel$ while the true coordinate is $x_\parallel$, and the apparent (true) transverse separation by $\tilde{\boldsymbol{x}}_\perp$ ($\boldsymbol{x}_\perp$). The apparent coordinates of the interloper emission are related to the true coordinates by [201]: $\tilde{x}_\parallel = \frac{H(z_i)}{H(z_t)} \frac{1+z_t}{1+z_i} x_\parallel$, and $\tilde{\boldsymbol{x}}_\perp = \frac{D_{\rm A,co}(z_t)}{D_{\rm A,co}(z_i)} \boldsymbol{x}_\perp$, where $H(z)$ is the Hubble parameter, and $D_{\rm A,co}(z)$ is the co-moving angular diameter distance. Under these coordinate transformations, the apparent power spectrum of the interloper emission becomes highly anisotropic owing to the different mis-mappings in the line of sight and transverse directions. This is essentially the Alcock-Paczynski effect [281], except here the warping arises from assuming an incorrect redshift rather than the wrong cosmology.

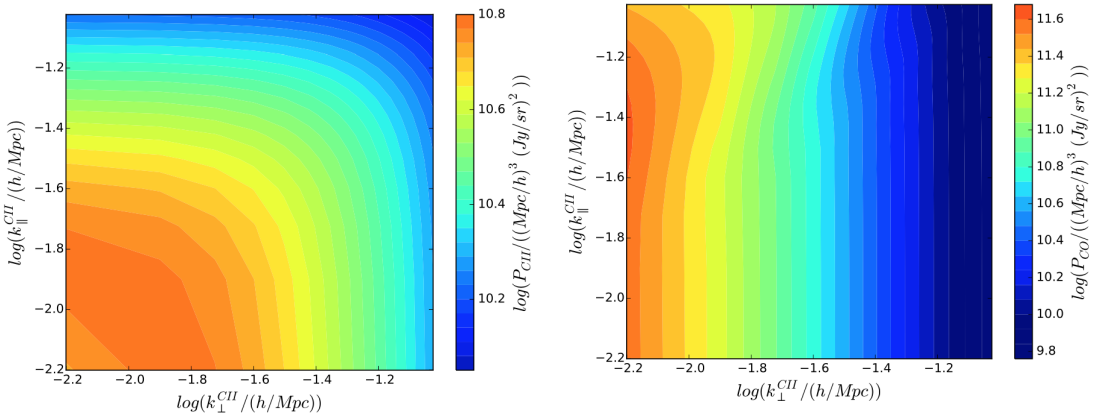

Figure 47. *Fitting-out interloper contamination using their anisotropic contribution to the line-intensity mapping power spectrum.* ***Left panel****: 3D Power spectrum of [CII] from $z = 6$.* ***Right Panel*** *: The brightest CO interloper power spectrum, CO(3-2) from $z = 0.27$, projected onto the [CII] co-moving frame. The CO interloper power spectrum contours are highly elongated as a consequence of the coordinate mapping distortion described in the text. (Courtesy of Yun-Ting Cheng)*

This interloper emission anisotropy is illustrated in Fig. 47 for the case of a $z = 6$ [CII] line-intensity mapping survey. After projecting the observed volume onto the $z = 6$ [CII] co-moving frame, the resulting total power spectrum is a superposition of [CII] and CO power spectra at different redshifts, each with a different but predictable 3D shape due to the projection. Fig. 47 shows the projected [CII] and brightest CO interloper – CO (3-2) from $z = 0.27$ — emission power spectra. Cheng et al. [280] demonstrate, using an MCMC approach, that a sufficiently sensitive survey can use this distinctive anisotropy to fit out the interloper contamination. Although the method is illustrated here for the specific case of a $z = 6$ [CII] survey, it should be broadly applicable to a range of different line-intensity mapping measurements.

Modeling Assumptions and Uncertainties

It is worth emphasizing explicitly that interloper contamination predictions are subject to significant uncertainties in the modeling and sensitive to the precise assumptions made in these calculations. One illustration of this is provided by Fig. 48 for the specific case of HCN(1-0) interloper contamination for CO(1-0) line-intensity mapping surveys.

If a power-law luminosity halo mass relation is assumed, as in Breysse et al. [14], then simulated HCN emission may seriously impact CO power spectra and detection significances in a COMAP-like survey, if steps are not made to remove this contamination (e.g. Fig. 46). However, a more realistic model informed by empirical constraints on high mass galaxies likely includes a turnover at high mass owing to declining star-formation efficiency. Incorporating this turnover in both CO and HCN modeling, as in Li et al. [98], Chung et al. [282] find that the simulated HCN auto spectrum lies several orders of magnitude below the CO auto spectrum, across all spatial modes (see Figure 48). The resulting contamination in total detection significance is small, and while several other interloper lines emit at luminosities similar to HCN(1-0), one nonetheless expects the total effect to be subdominant compared to other systematics and foregrounds expected in CO surveys [282]. More generally, it is important to bear in mind that power-law models often over-predict the relative contribution of high-mass emitters (with halo masses greater than $\sim 10^{12}\,M_\odot$) to the line-intensity spectrum, especially to the shot-noise component. The precise impact, however, depends on, for example,

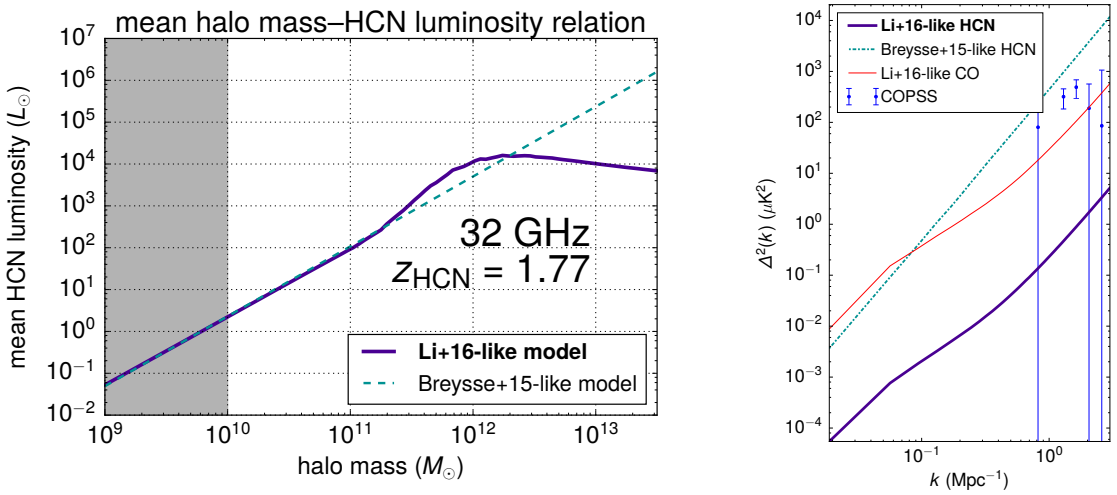

Figure 48. *Illustration of the difference in predicted HCN contamination in a CO survey based on the modeling approach taken, adapted from Chung et al. [282].* ***Left Panel:*** *the mean halo mass–HCN line-luminosity relation, given a power-law model following Breysse et al. [14] and a model following Li et al. [98], which incorporates a declining star-formation efficiency at high-mass.* ***Right Panel:*** *the resulting HCN auto power spectrum, plotted as $\Delta^2(k)$ against the COPSS tentative detections and the CO power spectrum expected from the model in Li et al. [98]. The power-law model predicts high shot-noise contamination from HCN, but the more complex model does not, since it lacks rare, extreme-luminosity ($\gtrsim 10^4\,L_\odot$) HCN emitters. (Courtesy of Dongwoo Chung)*

the relationship between line luminosity and star-formation rate. Future refinements in modeling efforts (such as those described in §5.1), studies based on semi-numerical simulations [122] and additional empirical constraints should help improve efforts to forecast the impact of interlopers and techniques to mitigate them.

6

Conclusion

This Status Report has summarized the recent ideas in intensity mapping theory and experiment presented at the first two annual workshops held at Stanford and Johns Hopkins in 2016 and 2017. After providing a short introduction to the field, various high-profile science goals that have been identified were laid out above, followed by a description of the first detections made in this new but rapidly advancing field. A separate section was dedicated to the experimental frontier, covering the different instruments that are planned to harvest the enormous volume between redshifts of unity to those of reionization and beyond. The final chapter discussed the methodologies being pursued as part of the effort to model and simulate the signals being sought, as well as the techniques that have been devised to efficiently analyze the data statistically, separate out foreground contamination and make optimal use of cross correlations between measurements at different frequencies. As this report demonstrates, the intensity mapping field is standing on firm ground, supported globally by the efforts of many dozens of scientists, and is set to make giant leaps forward over the next few years. The motivation for continued investment in this research, both in experiments and theory, is as strong as can be.

References

[1] Eli Visbal, Hy Trac, and Abraham Loeb. Demonstrating the Feasibility of Line Intensity Mapping Using Mock Data of Galaxy Clustering from Simulations. *JCAP*, 1108:010, 2011. doi: 10.1088/1475-7516/2011/08/010.

[2] Yan Gong, Asantha Cooray, Marta Silva, Mario G. Santos, James Bock, Matt Bradford, and Michael Zemcov. Intensity Mapping of the [CII] Fine Structure Line during the Epoch of Reionization. *Astrophys. J.*, 745:49, 2012. doi: 10.1088/0004-637X/745/1/49.

[3] A. T. Crites et al. The time-pilot intensity mapping experiment. *Proc.SPIE*, 9153:9153 – 9153 – 9, 2014. doi: 10.1117/12.2057207. URL `http://dx.doi.org/10.1117/12.2057207`.

[4] Bin Yue, Andrea Ferrara, Andrea Pallottini, Simona Gallerani, and Livia Vallini. Intensity mapping of [CII] emission from early galaxies. *Mon. Not. Roy. Astron. Soc.*, 450(4):3829–3839, 2015. doi: 10.1093/mnras/stv933.

[5] M. B. Silva, M. G. Santos, Y. Gong, A. Cooray, and J. Bock. Intensity Mapping of Lyα Emission during the Epoch of Reionization. *Ap. J.* , 763:132, February 2013. doi: 10.1088/0004-637X/763/2/132.

[6] Anthony R. Pullen, Olivier Doré, and Jamie Bock. Intensity Mapping across Cosmic Times with the *Lyα* Line. *Astrophys. J.*, 786:111, 2014. doi: 10.1088/0004-637X/786/2/111.

[7] Yan Gong, Marta Silva, Asantha Cooray, and Mario G. Santos. Foreground Contamination in Lyα Intensity Mapping during the Epoch of Reionization. *Astrophys. J.*, 785:72, 2014. doi: 10.1088/0004-637X/785/1/72.

[8] P. Comaschi and A. Ferrara. Probing high-redshift galaxies with Lyα intensity mapping. *Mon. Not. Roy. Astron. Soc.*, 455(1):725–738, 2016. doi: 10.1093/mnras/stv2339.

[9] Mattia Righi, Carlos Hernandez-Monteagudo, and Rashid Sunyaev. Carbon monoxide line emission as a CMB foreground: tomography of the star-forming universe with different spectral resolutions. *Astron. Astrophys.*, 489:489–504, 2008. doi: 10.1051/0004-6361:200810199.

[10] Adam Lidz, Steven R. Furlanetto, S. Peng Oh, James Aguirre, Tzu-Ching Chang, Olivier Doré, and Jonathan R. Pritchard. Intensity Mapping with Carbon Monoxide Emission Lines and the Redshifted 21 cm Line. *Astrophys. J.*, 741:70, 2011. doi: 10.1088/0004-637X/741/2/70.

[11] Anthony Pullen, Tzu-Ching Chang, Olivier Doré, and Adam Lidz. Cross-correlations as a carbon monoxide detector. 2013. doi: 10.1088/0004-637X/768/1/15.

[12] Natalie Mashian, Amiel Sternberg, and Abraham Loeb. Predicting the intensity mapping signal for multi-*J* CO lines. *JCAP*, 1511(11):028, 2015. doi: 10.1088/1475-7516/2015/11/028.

[13] Patrick C. Breysse, Ely D. Kovetz, and Marc Kamionkowski. Carbon Monoxide Intensity Mapping at Moderate Redshifts. *Mon. Not. Roy. Astron. Soc.*, 443(4):3506–3512, 2014. doi: 10.1093/mnras/stu1312.

[14] Patrick C. Breysse, Ely D. Kovetz, and Marc Kamionkowski. Masking line foregrounds in intensity mapping surveys. *Mon. Not. Roy. Astron. Soc.*, 452(4):3408–3418, 2015. doi: 10.1093/mnras/stv1476.

[15] Maki Suginohara, Tatsushi Suginohara, and David N. Spergel. Detecting Z ¿ 10 objects through carbon, nitrogen and oxygen emission lines. *Astrophys. J.*, 512:547, 1999. doi: 10.1086/306787.

[16] Olivier Doré et al. Cosmology with the SPHEREX All-Sky Spectral Survey. 2014.

[17] Asantha Cooray et al. Cosmic Dawn Intensity Mapper. 2016.

[18] Steven Furlanetto, S. Peng Oh, and Frank Briggs. Cosmology at Low Frequencies: The 21 cm Transition and the High-Redshift Universe. *Phys. Rept.*, 433:181–301, 2006. doi: 10.1016/j.physrep.2006.08.002.

[19] Miguel F. Morales and J. Stuart B. Wyithe. Reionization and Cosmology with 21 cm Fluctuations. *Ann. Rev. Astron. Astrophys.*, 48:127–171, 2010. doi: 10.1146/annurev-astro-081309-130936.

[20] J. R. Pritchard and A. Loeb. 21 cm cosmology in the 21st century. *Reports on Progress in Physics*, 75(8):086901, August 2012. doi: 10.1088/0034-4885/75/8/086901.

[21] Olivier Doré et al. Science Impacts of the SPHEREx All-Sky Optical to Near-Infrared Spectral Survey: Report of a Community Workshop Examining Extragalactic, Galactic, Stellar and Planetary Science. 2016.

[22] C. Creque-Sarbinowski et al. in preparation. 2017.

[23] Mandana Amiri et al. Limits on the ultra-bright Fast Radio Burst population from the CHIME Pathfinder. *Astrophys. J.*, 844(2):161, 2017. doi: 10.3847/1538-4357/aa713f.

[24] Eyal A. Kazin et al. The WiggleZ Dark Energy Survey: improved distance measurements to z = 1 with reconstruction of the baryonic acoustic feature. *Mon. Not. Roy. Astron. Soc.*, 441(4):3524–3542, 2014. doi: 10.1093/mnras/stu778.

[25] Ashley J. Ross et al. The clustering of galaxies in the completed SDSS-III Baryon Oscillation Spectroscopic Survey: Observational systematics and baryon acoustic oscillations in the correlation function. *Mon. Not. Roy. Astron. Soc.*, 464(1):1168–1191, 2017. doi: 10.1093/mnras/stw2372.

[26] Timothée Delubac et al. Baryon acoustic oscillations in the Lyα forest of BOSS DR11 quasars. *Astron. Astrophys.*, 574:A59, 2015. doi: 10.1051/0004-6361/201423969.

[27] Catherine Heymans et al. CFHTLenS tomographic weak lensing cosmological parameter constraints: Mitigating the impact of intrinsic galaxy alignments. *Mon. Not. Roy. Astron. Soc.*, 432:2433, 2013. doi: 10.1093/mnras/stt601.

[28] M. Jarvis et al. The DES Science Verification Weak Lensing Shear Catalogues. *Mon. Not. Roy. Astron. Soc.*, 460(2):2245–2281, 2016. doi: 10.1093/mnras/stw990.

[29] F. Köhlinger et al. KiDS-450: The tomographic weak lensing power spectrum and constraints on cosmological parameters. 2017.

[30] M. A. Troxel et al. Dark Energy Survey Year 1 Results: Cosmological Constraints from Cosmic Shear. 2017.

[31] Edward Macaulay, Ingunn Kathrine Wehus, and Hans Kristian Eriksen. Lower Growth Rate from Recent Redshift Space Distortion Measurements than Expected from Planck. *Phys. Rev. Lett.*, 111 (16):161301, 2013. doi: 10.1103/PhysRevLett.111.161301.

[32] Planck Collaboration XIII. Planck 2015 results. XIII. Cosmological parameters. *Astron. Astrophys.*, 594:A13, 2016. doi: 10.1051/0004-6361/201525830.

[33] Richard A. Battye and Adam Moss. Evidence for Massive Neutrinos from Cosmic Microwave Background and Lensing Observations. *Phys. Rev. Lett.*, 112(5):051303, 2014. doi: 10.1103/PhysRevLett.112.051303.

[34] Marco Raveri. Are cosmological data sets consistent with each other within the Λ cold dark matter model? *Phys. Rev.*, D93(4):043522, 2016. doi: 10.1103/PhysRevD.93.043522.

[35] Eleonora Di Valentino, Alessandro Melchiorri, and Joseph Silk. Reconciling Planck with the local value of H_0 in extended parameter space. *Phys. Lett.*, B761:242–246, 2016. doi: 10.1016/j.physletb.2016.08.043.

[36] Savvas Nesseris, George Pantazis, and Leandros Perivolaropoulos. Tension and constraints on modified gravity parametrizations of $G_{\rm eff}(z)$ from growth rate and Planck data. 2017.

[37] Janina Renk, Miguel Zumalacárregui, Francesco Montanari, and Alexandre Barreira. Galileon Gravity in Light of ISW, CMB, BAO and H_0 data. 2017.

[38] Wendy L. Freedman. Cosmology at at Crossroads: Tension with the Hubble Constant. *Nat. Astron.*, 1:0169, 2017.

[39] Amir Aghamousa et al. The DESI Experiment Part I: Science,Targeting, and Survey Design. 2016.

[40] Luca Amendola et al. Cosmology and fundamental physics with the Euclid satellite. *Living Rev. Rel.*, 16:6, 2013. doi: 10.12942/lrr-2013-6.

[41] Alexandra Abate et al. Large Synoptic Survey Telescope: Dark Energy Science Collaboration. 2012.

[42] Héctor Gil-Marín, Jorge Noreña, Licia Verde, Will J. Percival, Christian Wagner, Marc Manera, and Donald P. Schneider. The power spectrum and bispectrum of SDSS DR11 BOSS galaxies – I. Bias and gravity. *Mon. Not. Roy. Astron. Soc.*, 451(1):539–580, 2015. doi: 10.1093/mnras/stv961.

[43] G. J. Hill et al. The Hobby-Eberly Telescope Dark Energy Experiment (HETDEX): Description and Early Pilot Survey Results. *ASP Conf. Ser.*, 399:115–118, 2008.

[44] José Fonseca, Marta Silva, Mário G. Santos, and Asantha Cooray. Cosmology with intensity mapping techniques using atomic and molecular lines. *Mon. Not. Roy. Astron. Soc.*, 464(2):1948–1965, 2017. doi: 10.1093/mnras/stw2470.

[45] S. Saito, E. Komatsu, C.-T. Chiang, D. Jeong, and Ryu Makiya. Sparse sampling of line intensity mapping. in preparation, 2017.

[46] F. Villaescusa-Navarro, P. Bull, and M. Viel. Weighing Neutrinos with Cosmic Neutral Hydrogen. *Ap. J.* , 814:146, December 2015. doi: 10.1088/0004-637X/814/2/146.

[47] A. Liu and A. R. Parsons. Constraining cosmology and ionization history with combined 21 cm power spectrum and global signal measurements. *Mon. Not. Roy. Astron. Soc.*, 457:1864–1877, April 2016. doi: 10.1093/mnras/stw071.

[48] N. S. Kern, A. Liu, A. R. Parsons, A. Mesinger, and B. Greig. Emulating Simulations of Cosmic Dawn for 21cm Power Spectrum Constraints on Cosmology, Reionization, and X-ray Heating. *ArXiv e-prints*, May 2017.

[49] Y. Mao, M. Tegmark, M. McQuinn, M. Zaldarriaga, and O. Zahn. How accurately can 21cm tomography constrain cosmology? *Phys. Rev.* **D** , 78(2):023529, July 2008. doi: 10.1103/PhysRevD.78.023529.

[50] S. Clesse, L. Lopez-Honorez, C. Ringeval, H. Tashiro, and M. H. G. Tytgat. Background reionization history from omniscopes. *Phys. Rev.* **D** , 86(12):123506, December 2012. doi: 10.1103/PhysRevD.86.123506.

[51] R. Barkana and A. Loeb. A Method for Separating the Physics from the Astrophysics of High-Redshift 21 Centimeter Fluctuations. *Ap. J. Lett.*, 624:L65–L68, May 2005. doi: 10.1086/430599.

[52] P. R. Shapiro, Y. Mao, I. T. Iliev, G. Mellema, K. K. Datta, K. Ahn, and J. Koda. Will Nonlinear Peculiar Velocity and Inhomogeneous Reionization Spoil 21 cm Cosmology from the Epoch of Reionization? *Physical Review Letters*, 110(15):151301, April 2013. doi: 10.1103/PhysRevLett.110.151301.

[53] A. Liu, J. R. Pritchard, R. Allison, A. R. Parsons, U. Seljak, and B. D. Sherwin. Eliminating the optical depth nuisance from the CMB with 21 cm cosmology. *Phys. Rev.* **D** , 93(4):043013, February 2016. doi: 10.1103/PhysRevD.93.043013.

[54] Marco Raveri, Philip Bull, Alessandra Silvestri, and Levon Pogosian. Priors on the effective Dark Energy equation of state in scalar-tensor theories. 2017.

[55] Philip Bull. Extending cosmological tests of General Relativity with the Square Kilometre Array. *Astrophys. J.*, 817(1):26, 2016. doi: 10.3847/0004-637X/817/1/26.

[56] Justin Khoury and Amanda Weltman. Chameleon fields: Awaiting surprises for tests of gravity in space. *Phys. Rev. Lett.*, 93:171104, 2004. doi: 10.1103/PhysRevLett.93.171104.

[57] Justin Khoury and Amanda Weltman. Chameleon cosmology. *Phys. Rev.*, D69:044026, 2004. doi: 10.1103/PhysRevD.69.044026.

[58] A. I. Vainshtein. To the problem of nonvanishing gravitation mass. *Phys. Lett.*, 39B:393–394, 1972. doi: 10.1016/0370-2693(72)90147-5.

[59] Bhuvnesh Jain et al. Novel Probes of Gravity and Dark Energy. 2013.

[60] Cora Dvorkin, Kfir Blum, and Marc Kamionkowski. Constraining Dark Matter-Baryon Scattering with Linear Cosmology. *Phys. Rev.*, D89(2):023519, 2014. doi: 10.1103/PhysRevD.89.023519.

[61] Y. Ali-Haïmoud, J. Chluba, and M. Kamionkowski. Constraints on Dark Matter Interactions with Standard Model Particles from Cosmic Microwave Background Spectral Distortions. *Physical Review Letters*, 115(7):071304, August 2015. doi: 10.1103/PhysRevLett.115.071304.

[62] Tracy R. Slatyer and Chih-Liang Wu. General Constraints on Dark Matter Decay from the Cosmic Microwave Background. *Phys. Rev.*, D95(2):023010, 2017. doi: 10.1103/PhysRevD.95.023010.

[63] C. Evoli, A. Mesinger, and A. Ferrara. Unveiling the nature of dark matter with high redshift 21 cm line experiments. *Journal of Cosmology and Astroparticle Physics*, 2014(11):024, 2014. URL `http://stacks.iop.org/1475-7516/2014/i=11/a=024`.

[64] A. Mesinger, A. Ewall-Wice, and J. Hewitt. Reionization and beyond: detecting the peaks of the cosmological 21 cm signal. *Mon. Not. Roy. Astron. Soc.*, 439:3262–3274, April 2014. doi: 10.1093/mnras/stu125.

[65] J. B. Muñoz, E. D. Kovetz, and Y. Ali-Haïmoud. Heating of baryons due to scattering with dark matter during the dark ages. *Phys. Rev.* **D** , 92(8):083528, October 2015. doi: 10.1103/PhysRevD.92.083528.

[66] Roland de Putter, Jérôme Gleyzes, and Olivier Doré. Next non-Gaussianity frontier: What can a measurement with σ $(\mathrm{f}_{NL})\lesssim 1$ tell us about multifield inflation? *Phys. Rev.*, D95(12):123507, 2017. doi: 10.1103/PhysRevD.95.123507.

[67] Neal Dalal, Olivier Doré, Dragan Huterer, and Alexander Shirokov. The imprints of primordial non-gaussianities on large-scale structure: scale dependent bias and abundance of virialized objects. *Phys. Rev.*, D77:123514, 2008. doi: 10.1103/PhysRevD.77.123514.

[68] Uros Seljak. Extracting primordial non-gaussianity without cosmic variance. *Phys. Rev. Lett.*, 102: 021302, 2009. doi: 10.1103/PhysRevLett.102.021302.

[69] David Alonso and Pedro G. Ferreira. Constraining ultralarge-scale cosmology with multiple tracers in optical and radio surveys. *Phys. Rev.*, D92(6):063525, 2015. doi: 10.1103/PhysRevD.92.063525.

[70] José Fonseca, Stefano Camera, Mário Santos, and Roy Maartens. Hunting down horizon-scale effects with multi-wavelength surveys. *Astrophys. J.*, 812(2):L22, 2015. doi: 10.1088/2041-8205/812/2/L22.

[71] B. E. Robertson, R. S. Ellis, S. R. Furlanetto, and J. S. Dunlop. Cosmic Reionization and Early Star-forming Galaxies: A Joint Analysis of New Constraints from Planck and the Hubble Space Telescope. *Ap. J. Lett.*, 802:L19, April 2015. doi: 10.1088/2041-8205/802/2/L19.

[72] D. R. DeBoer, A. R. Parsons, J. E. Aguirre, P. Alexander, Z. S. Ali, A. P. Beardsley, G. Bernardi, J. D. Bowman, R. F. Bradley, C. L. Carilli, C. Cheng, E. de Lera Acedo, J. S. Dillon, A. Ewall-Wice, G. Fadana, N. Fagnoni, R. Fritz, S. R. Furlanetto, B. Glendenning, B. Greig, J. Grobbelaar, B. J. Hazelton, J. N. Hewitt, J. Hickish, D. C. Jacobs, A. Julius, M. Kariseb, S. A. Kohn, T. Lekalake, A. Liu, A. Loots, D. MacMahon, L. Malan, C. Malgas, M. Maree, Z. Martinot, N. Mathison, E. Matsetela, A. Mesinger, M. F. Morales, A. R. Neben, N. Patra, S. Pieterse, J. C. Pober, N. Razavi-Ghods, J. Ringuette, J. Robnett, K. Rosie, R. Sell, C. Smith, A. Syce, M. Tegmark, N. Thyagarajan, P. K. G. Williams, and H. Zheng. Hydrogen Epoch of Reionization Array (HERA). *Publ. Astron. Soc. Pac.*, 129(4):045001, April 2017. doi: 10.1088/1538-3873/129/974/045001.

[73] J. C. Pober, A. Liu, J. S. Dillon, J. E. Aguirre, J. D. Bowman, R. F. Bradley, C. L. Carilli, D. R. DeBoer, J. N. Hewitt, D. C. Jacobs, M. McQuinn, M. F. Morales, A. R. Parsons, M. Tegmark, and D. J. Werthimer. What Next-generation 21 cm Power Spectrum Measurements can Teach us About the Epoch of Reionization. *Ap. J.* , 782:66, February 2014. doi: 10.1088/0004-637X/782/2/66.

[74] B. Greig and A. Mesinger. 21CMMC: an MCMC analysis tool enabling astrophysical parameter studies of the cosmic 21 cm signal. *Mon. Not. Roy. Astron. Soc.*, 449:4246–4263, June 2015. doi: 10.1093/mnras/stv571.

[75] B. Greig and A. Mesinger. Simultaneously constraining the astrophysics of reionisation and the epoch of heating with 21CMMC. *ArXiv e-prints*, May 2017.

[76] R. A. Battye, I. W. A. Browne, C. Dickinson, G. Heron, B. Maffei, and A. Pourtsidou. HI intensity mapping : a single dish approach. *Mon. Not. Roy. Astron. Soc.*, 434:1239–1256, 2013. doi: 10.1093/mnras/stt1082.

[77] Kevin Bandura et al. Canadian Hydrogen Intensity Mapping Experiment (CHIME) Pathfinder. *Proc. SPIE Int. Soc. Opt. Eng.*, 9145:22, 2014. doi: 10.1117/12.2054950.

[78] L. B. Newburgh et al. HIRAX: A Probe of Dark Energy and Radio Transients. *Proc. SPIE Int. Soc. Opt. Eng.*, 9906:99065X, 2016. doi: 10.1117/12.2234286.

[79] José Fonseca, Roy Maartens, and Mário G. Santos. Probing the primordial Universe with MeerKAT and DES. *Mon. Not. Roy. Astron. Soc.*, 466(3):2780–2786, 2017. doi: 10.1093/mnras/stw3248.

[80] Mario G. Santos et al. Cosmology with a SKA HI intensity mapping survey. 2015.

[81] Xuelei Chen. The Tianlai project: a 21cm cosmology experiment. *Int. J. Mod. Phys. Conf. Ser.*, 12: 256–263, 2012. doi: 10.1142/S2010194512006459.

[82] S. W. Henderson et al. Advanced ACTPol Cryogenic Detector Arrays and Readout. *J. Low. Temp. Phys.*, 184(3-4):772–779, 2016. doi: 10.1007/s10909-016-1575-z.

[83] B. A. Benson et al. SPT-3G: A Next-Generation Cosmic Microwave Background Polarization Experiment on the South Pole Telescope. *Proc. SPIE Int. Soc. Opt. Eng.*, 9153:91531P, 2014. doi: 10.1117/12.2057305.

[84] H. Prince K.M̃oodley and A. Pénin. Cross-correlation of CMB lensing with 21cm intensity mapping surveys. 2017. in prep.

[85] Hong-Ming Zhu, Ue-Li Pen, Yu Yu, and Xuelei Chen. Recovering lost 21 cm radial modes via cosmic tidal reconstruction. 2016.

[86] K. W. Masui et al. Measurement of 21 cm brightness fluctuations at z 0.8 in cross-correlation. *Astrophys. J.*, 763:L20, 2013. doi: 10.1088/2041-8205/763/1/L20.

[87] Hee-Jong Seo and Christopher M. Hirata. The foreground wedge and 21 cm BAO surveys. *Mon. Not. Roy. Astron. Soc.*, 456(3):3142–3156, 2016. doi: 10.1093/mnras/stv2806.

[88] J. D. Cohn, Martin White, Tzu-Ching Chang, Gil Holder, Nikhil Padmanabhan, and Olivier Doré. Combining galaxy and 21-cm surveys. *Mon. Not. Roy. Astron. Soc.*, 457(2):2068–2077, 2016. doi: 10.1093/mnras/stw108.

[89] L. Wolz, C. Blake, and J. S. B. Wyithe. Determining the HI content of galaxies via intensity mapping cross-correlations. 2017. doi: 10.1093/mnras/stx1388.

[90] David Alonso, Pedro G. Ferreira, Matt J. Jarvis, and Kavilan Moodley. Calibrating photometric redshifts with intensity mapping observations. *Phys. Rev.*, D96:043515, 2017. doi: 10.1103/PhysRevD.96.043515.

[91] Piero Madau and Mark Dickinson. Cosmic Star Formation History. *Ann. Rev. Astron. Astrophys.*, 52: 415–486, 2014. doi: 10.1146/annurev-astro-081811-125615.

[92] M. T. Huynh, B. H. C. Emonts, A. E. Kimball, N. Seymour, I. Smail, A. M. Swinbank, W. N. Brandt, C. M. Casey, S. C. Chapman, H. Dannerbauer, J. A. Hodge, R. J. Ivison, E. Schinnerer, A. P. Thomson, P. van der Werf, and J. L. Wardlow. The AT-LESS CO(1-0) survey of submillimetre galaxies in the Extended Chandra Deep Field South: First results on cold molecular gas in galaxies at z 2. *Mon. Not. Roy. Astron. Soc.*, 467:1222–1230, May 2017. doi: 10.1093/mnras/stx156.

[93] Fabian Walter, Frank Bertoldi, Chris Carilli, Pierre Cox, K. Y. Lo, Roberto Neri, Xiao-Hui Fan, Alain Omont, Michael A. Strauss, and Karl M. Menten. Molecular gas in the host galaxy of a quasar at redshift z=6.42. *Nature*, 424:406–408, 2003. doi: 10.1038/nature01821.

[94] Mark T. Sargent, E. Daddi, M. Béthermin, H. Aussel, G. Magdis, H. S. Hwang, S. Juneau, D. Elbaz, and E. da Cunha. Regularity underlying complexity: A redshift-independent description of the continuous variation of galaxy-scale molecular gas properties in the mass-star formation rate plane. *Astrophys. J.*, 793(1):19, 2014. doi: 10.1088/0004-637X/793/1/19.

[95] R. Davé, R. Thompson, and P. F. Hopkins. MUFASA: galaxy formation simulations with meshless hydrodynamics. *Mon. Not. Roy. Astron. Soc.*, 462:3265–3284, November 2016. doi: 10.1093/mnras/stw1862.

[96] Patrick C. Breysse, Ely D. Kovetz, and Marc Kamionkowski. The high redshift star-formation history from carbon-monoxide intensity maps. *Mon. Not. Roy. Astron. Soc.*, 457(1):L127–L131, 2016. doi: 10.1093/mnrasl/slw005.

[97] G. K. Keating, G. C. Bower, D. P. Marrone, D. R. DeBoer, C. Heiles, T.-C. Chang, J. E. Carlstrom, C. H. Greer, D. Hawkins, J. W. Lamb, E. Leitch, A. D. Miller, S. Muchovej, and D. P. Woody. First Results from COPSS: The CO Power Spectrum Survey. *Ap. J.* , 814:140, December 2015. doi: 10.1088/0004-637X/814/2/140.

[98] Tony Y. Li, Risa H. Wechsler, Kiruthika Devaraj, and Sarah E. Church. Connecting CO Intensity Mapping to Molecular Gas and Star Formation in the Epoch of Galaxy Assembly. *Astrophys. J.*, 817 (2):169, 2016. doi: 10.3847/0004-637X/817/2/169.

[99] Matthew D. Kistler, Hasan Yuksel, and Andrew M. Hopkins. The Cosmic Star Formation Rate from the Faintest Galaxies in the Unobservable Universe. 2013.

[100] E. Visbal, Z. Haiman, and G. L. Bryan. Looking for Population III stars with He II line intensity mapping. *Mon. Not. Roy. Astron. Soc.*, 450:2506–2513, July 2015. doi: 10.1093/mnras/stv785.

[101] D. Schaerer. On the properties of massive Population III stars and metal-free stellar populations. *A & A* , 382:28–42, January 2002. doi: 10.1051/0004-6361:20011619.

[102] Patrick C. Breysse and Mubdi Rahman. Feeding cosmic star formation: Exploring high-redshift molecular gas with CO intensity mapping. *Mon. Not. Roy. Astron. Soc.*, 468(1):741–750, 2017. doi: 10.1093/mnras/stx451.

[103] M. Fukugita, C. J. Hogan, and P. J. E. Peebles. The Cosmic baryon budget. *Astrophys. J.*, 503:518, 1998. doi: 10.1086/306025.

[104] Renyue Cen and Jeremiah P. Ostriker. Where are the baryons? *Astrophys. J.*, 514:1–6, 1999. doi: 10.1086/306949.

[105] R. A. C. Croft, J. Miralda-Escudé, Z. Zheng, A. Bolton, K. S. Dawson, J. B. Peterson, D. G. York, D. Eisenstein, J. Brinkmann, J. Brownstein, R. Cen, T. Delubac, A. Font-Ribera, J.-C. Hamilton, K.-G. Lee, A. Myers, N. Palanque-Delabrouille, I. Pâris, P. Petitjean, M. M. Pieri, N. P. Ross, G. Rossi, D. J. Schlegel, D. P. Schneider, A. Slosar, J. Vazquez, M. Viel, D. H. Weinberg, and C. Yèche. Large-scale clustering of Lyman α emission intensity from SDSS/BOSS. *Mon. Not. Roy. Astron. Soc.*, 457: 3541–3572, April 2016. doi: 10.1093/mnras/stw204.

[106] Emmanuel Schaan et al. Evidence for the kinematic Sunyaev-Zeldovich effect with the Atacama Cosmology Telescope and velocity reconstruction from the Baryon Oscillation Spectroscopic Survey. *Phys. Rev.*, D93(8):082002, 2016. doi: 10.1103/PhysRevD.93.082002.

[107] Tzu-Ching Chang, Ue-Li Pen, Kevin Bandura, and Jeffrey B. Peterson. Hydrogen 21-cm Intensity Mapping at redshift 0.8. *Nature*, 466:463–465, 2010. doi: 10.1038/nature09187.

[108] Marc Davis, Jeffrey A. Newman, Sandra M. Faber, and Andrew C. Phillips. The DEEP2 Redshift Survey. In *Proceedings, Workshop on Deep Fields: Garching, Germany, October 9-12, 2000*, 2000. doi: 10.1007/10854354_66.

[109] Alison L. Coil, Jeffrey A. Newman, Nick Kaiser, Marc Davis, Chung-Pei Ma, and Dale D. Kocevski. Evolution and color-dependence of the galaxy angular correlation function: 350,000 galaxies in 5 square degrees. *Astrophys. J.*, 617:765–781, 2004. doi: 10.1086/425676.

[110] Michael J. Drinkwater et al. The WiggleZ Dark Energy Survey: Survey Design and First Data Release. *Mon. Not. Roy. Astron. Soc.*, 401:1429–1452, 2010. doi: 10.1111/j.1365-2966.2009.15754.x.

[111] E. R. Switzer et al. Determination of z 0.8 neutral hydrogen fluctuations using the 21 cm intensity mapping auto-correlation. *Mon. Not. Roy. Astron. Soc.*, 434:L46, 2013. doi: 10.1093/mnrasl/slt074.

[112] Eric R. Switzer, Tzu-Ching Chang, Kiyoshi W. Masui, Ue-Li Pen, and Tabitha C. Voytek. Interpreting the unresolved intensity of cosmologically redshifted line radiation. *Astrophys. J.*, 815(1):51, 2015. doi: 10.1088/0004-637X/815/1/51.

[113] G. K. Keating, D. P. Marrone, G. C. Bower, E. Leitch, J. E. Carlstrom, and D. R. DeBoer. COPSS II: The Molecular Gas Content of Ten Million Cubic Megaparsecs at Redshift z 3. *Ap. J.* , 830:34, October 2016. doi: 10.3847/0004-637X/830/1/34.

[114] Anthony R. Pullen, Paolo Serra, Tzu-Ching Chang, Olivier Doré, and Shirley Ho. Search for CII Emission on Cosmological Scales at Redshift Z 2.6. 2017.

[115] R. Adam et al. Planck 2015 results. X. Diffuse component separation: Foreground maps. *Astron. Astrophys.*, 594:A10, 2016. doi: 10.1051/0004-6361/201525967.

[116] P. A. R. Ade et al. Planck 2013 results. XXX. Cosmic infrared background measurements and implications for star formation. *Astron. Astrophys.*, 571:A30, 2014. doi: 10.1051/0004-6361/201322093.

[117] Shadab Alam et al. The clustering of galaxies in the completed SDSS-III Baryon Oscillation Spectroscopic Survey: cosmological analysis of the DR12 galaxy sample. *Mon. Not. Roy. Astron. Soc.*, 470(3):2617–2652, 2017. doi: 10.1093/mnras/stx721.

[118] Beth Reid et al. SDSS-III Baryon Oscillation Spectroscopic Survey Data Release 12: galaxy target selection and large scale structure catalogues. *Mon. Not. Roy. Astron. Soc.*, 455(2):1553–1573, 2016. doi: 10.1093/mnras/stv2382.

[119] S. Alam, F. D. Albareti, C. Allende Prieto, F. Anders, S. F. Anderson, T. Anderton, B. H. Andrews, E. Armengaud, É. Aubourg, S. Bailey, and et al. The Eleventh and Twelfth Data Releases of the Sloan Digital Sky Survey: Final Data from SDSS-III. *Ap. J. Suppl.* , 219:12, July 2015. doi: 10.1088/0067-0049/219/1/12.

[120] C. Shang, Z. Haiman, L. Knox, and S. P. Oh. Improved models for cosmic infrared background anisotropies: new constraints on the infrared galaxy population. *Mon. Not. Roy. Astron. Soc.*, 421:2832–2845, April 2012. doi: 10.1111/j.1365-2966.2012.20510.x.

[121] Y. Gong, A. Cooray, M. Silva, M. G. Santos, J. Bock, C. M. Bradford, and M. Zemcov. Intensity Mapping of the [C II] Fine Structure Line during the Epoch of Reionization. *Ap. J.* , 745:49, January 2012. doi: 10.1088/0004-637X/745/1/49.

[122] Marta B. Silva, Mário G. Santos, Asantha Cooray, and Yan Gong. Prospects for Detecting [CII] Emission During the Epoch of Reionization. *Astrophys. J.*, 806(2):209, 2015. doi: 10.1088/0004-637X/806/2/209.

[123] Paolo Serra, Olivier Doré, and Guilaine Lagache. Dissecting the high-z interstellar medium through intensity mapping cross-correlations. *Astrophys. J.*, 833(2):153, 2016. doi: 10.3847/1538-4357/833/2/153.

[124] Michael Levi et al. The DESI Experiment, a whitepaper for Snowmass 2013. 2013.

[125] Rupert A. C. Croft et al. Large-scale clustering of Lyα emission intensity from SDSS/BOSS. *Mon. Not. Roy. Astron. Soc.*, 457(4):3541–3572, 2016. doi: 10.1093/mnras/stw204.

[126] F. J. Castander, O. Ballester, A. Bauer, L. Cardiel-Sas, J. Carretero, R. Casas, J. Castilla, M. Crocce, M. Delfino, M. Eriksen, E. Fernández, P. Fosalba, J. García-Bellido, E. Gaztañaga, F. Grañena, C. Hernández, J. Jiménez, L. López, P. Martí, R. Miquel, C. Neissner, C. Padilla, C. Pío, R. Ponce, E. Sanchez, S. Serrano, I. Sevilla, N. Tonello, and J. de Vicente. The PAU camera and the PAU survey at the William Herschel Telescope. In *Ground-based and Airborne Instrumentation for Astronomy IV*, volume 8446 of *Proc.SPIE*, page 84466D, September 2012. doi: 10.1117/12.926234.

[127] N. Benitez et al. J-PAS: The Javalambre-Physics of the Accelerated Universe Astrophysical Survey. 2014.

[128] D. Price, L. J. Greenhill, and et al. in prep.

[129] J. Kocz, L. J. Greenhill, B. R. Barsdell, D. Price, G. Bernardi, S. Bourke, M. A. Clark, J. Craig, M. Dexter, J. Dowell, T. Eftekhari, S. Ellingson, G. Hallinan, J. Hartman, A. Jameson, D. MacMahon, G. Taylor, F. Schinzel, and D. Werthimer. Digital Signal Processing Using Stream High Performance Computing: A 512-Input Broadband Correlator for Radio Astronomy. *Journal of Astronomical Instrumentation*, 4:1550003, March 2015. doi: 10.1142/S2251171715500038.

[130] A. Fialkov, R. Barkana, A. Pinhas, and E. Visbal. Complete history of the observable 21 cm signal from the first stars during the pre-reionization era. *Mon. Not. Roy. Astron. Soc.*, 437:L36–L40, January 2014. doi: 10.1093/mnrasl/slt135.

[131] M. W. Eastwood, G. Hallinan, and et al. The radio sky at meter wavelengths: m-mode analysis imaging with the Owens Valley Long Wavelength Array. in prep.

[132] D. R. DeBoer, A. R. Parsons, J. E. Aguirre, P. Alexander, Z. S. Ali, A. P. Beardsley, G. Bernardi, J. D. Bowman, R. F. Bradley, C. L. Carilli, C. Cheng, E. de Lera Acedo, J. S. Dillon, A. Ewall-Wice, G. Fadana, N. Fagnoni, R. Fritz, S. R. Furlanetto, B. Glendenning, B. Greig, J. Grobbelaar, B. J. Hazelton, J. N. Hewitt, J. Hickish, D. C. Jacobs, A. Julius, M. Kariseb, S. A. Kohn, T. Lekalake, A. Liu, A. Loots, D. MacMahon, L. Malan, C. Malgas, M. Maree, Z. Martinot, N. Mathison, E. Matsetela, A. Mesinger, M. F. Morales, A. R. Neben, N. Patra, S. Pieterse, J. C. Pober, N. Razavi-Ghods, J. Ringuette, J. Robnett, K. Rosie, R. Sell, C. Smith, A. Syce, M. Tegmark, N. Thyagarajan, P. K. G. Williams, and H. Zheng. Hydrogen Epoch of Reionization Array (HERA). *Publ. Astron. Soc. Pac.*, 129(4):045001, April 2017. doi: 10.1088/1538-3873/129/974/045001.

[133] B. Greig and A. Mesinger. 21CMMC: an MCMC analysis tool enabling astrophysical parameter studies of the cosmic 21 cm signal. *Mon. Not. Roy. Astron. Soc.*, 449:4246–4263, June 2015. doi: 10.1093/mnras/stv571.

[134] A. Ewall-Wice, J. Hewitt, A. Mesinger, J. S. Dillon, A. Liu, and J. Pober. Constraining high-redshift X-ray sources with next generation 21-cm power spectrum measurements. *Mon. Not. Roy. Astron. Soc.*, 458:2710–2724, May 2016. doi: 10.1093/mnras/stw452.

[135] C. L. Carilli and P. Sims. HERA Imaging: Mock Obserations using CASA. *HERA Memo Series #12*, (12), 2016.

[136] M. Malloy and A. Lidz. Identifying Ionized Regions in Noisy Redshifted 21 cm Data Sets. *Ap. J.* , 767:68, April 2013. doi: 10.1088/0004-637X/767/1/68.

[137] A. P. Beardsley, M. F. Morales, A. Lidz, M. Malloy, and P. M. Sutter. Adding Context to James Webb Space Telescope Surveys with Current and Future 21 cm Radio Observations. *Ap. J.* , 800:128, February 2015. doi: 10.1088/0004-637X/800/2/128.

[138] J. S. Dillon and A. R. Parsons. Redundant Array Configurations for 21 cm Cosmology. *Ap. J.* , 826: 181, August 2016. doi: 10.3847/0004-637X/826/2/181.

[139] A. R. Neben, R. F. Bradley, J. N. Hewitt, D. R. DeBoer, A. R. Parsons, J. E. Aguirre, Z. S. Ali, C. Cheng, A. Ewall-Wice, N. Patra, N. Thyagarajan, J. Bowman, R. Dickenson, J. S. Dillon, P. Doolittle, D. Egan, M. Hedrick, D. C. Jacobs, S. A. Kohn, P. J. Klima, K. Moodley, B. R. B. Saliwanchik, P. Schaffner, J. Shelton, H. A. Taylor, R. Taylor, M. Tegmark, B. Wirt, and H. Zheng. The Hydrogen Epoch of Reionization Array Dish. I. Beam Pattern Measurements and Science Implications. *Ap. J.* , 826:199, August 2016. doi: 10.3847/0004-637X/826/2/199.

[140] A. Ewall-Wice, R. Bradley, D. Deboer, J. Hewitt, A. Parsons, J. Aguirre, Z. S. Ali, J. Bowman, C. Cheng, A. R. Neben, N. Patra, N. Thyagarajan, M. Venter, E. de Lera Acedo, J. S. Dillon, R. Dickenson, P. Doolittle, D. Egan, M. Hedrick, P. Klima, S. Kohn, P. Schaffner, J. Shelton, B. Saliwanchik, H. A. Taylor, R. Taylor, M. Tegmark, and B. Wirt. The Hydrogen Epoch of Reionization Array Dish. II. Characterization of Spectral Structure with Electromagnetic Simulations and Its Science Implications. *Ap. J.* , 831:196, November 2016. doi: 10.3847/0004-637X/831/2/196.

[141] N. Patra, A. R. Parsons, D. R. DeBoer, N. Thyagarajan, A. Ewall-Wice, G. Hsyu, T. Kuk Leung, C. K. Day, J. E. Aguirre, P. Alexander, Z. S. Ali, A. P. Beardsley, J. D. Bowman, R. F. Bradley, C. L. Carilli, C. Cheng, E. de Lera Acedo, J. S. Dillon, G. Fadana, N. Fagnoni, R. Fritz, S. R. Furlanetto, B. Glendenning, B. Greig, J. Grobbelaar, B. J. Hazelton, J. N. Hewitt, D. C. Jacobs, A. Julius, M. Kariseb, S. A. Kohn, A. Lebedeva, T. Lekalake, A. Liu, A. Loots, D. MacMahon, L. Malan, C. Malgas, M. Maree, Z. Martinot, N. Mathison, E. Matsetela, A. Mesinger, M. F. Morales, A. R. Neben, S. Pieterse, J. C. Pober, N. Razavi-Ghods, J. Ringuette, J. Robnett, K. Rosie, R. Sell, C. Smith, A. Syce, M. Tegmark, P. K. G. Williams, and H. Zheng. The Hydrogen Epoch of Reionization Array Dish III: Measuring Chromaticity of Prototype Element with Reflectometry. *ArXiv e-prints 1701.03209*, January 2017.

[142] N. Thyagarajan, A. R. Parsons, D. R. DeBoer, J. D. Bowman, A. M. Ewall-Wice, A. R. Neben, and N. Patra. Effects of Antenna Beam Chromaticity on Redshifted 21 cm Power Spectrum and Implications for Hydrogen Epoch of Reionization Array. *Ap. J.* , 825:9, July 2016. doi: 10.3847/0004-637X/825/1/9.

[143] L. V. E. Koopmans et al. The Cosmic Dawn and Epoch of Reionization with the Square Kilometre Array. *PoS*, AASKA14:001, 2015.

[144] M. Aravena, R. Decarli, F. Walter, R. Bouwens, P. A. Oesch, C. L. Carilli, F. E. Bauer, E. Da Cunha, E. Daddi, J. Gónzalez-López, R. J. Ivison, D. A. Riechers, I. Smail, A. M. Swinbank, A. Weiss, T. Anguita, R. Bacon, E. Bell, F. Bertoldi, P. Cortes, P. Cox, J. Hodge, E. Ibar, H. Inami, L. Infante, A. Karim, B. Magnelli, K. Ota, G. Popping, P. van der Werf, J. Wagg, and Y. Fudamoto. The ALMA Spectroscopic Survey in the Hubble Ultra Deep Field: Search for [CII] Line and Dust Emission in 6. *Ap. J.* , 833:71, December 2016. doi: 10.3847/1538-4357/833/1/71.

[145] N. H. Hayatsu, Y. Matsuda, H. Umehata, N. Yoshida, I. Smail, A. M. Swinbank, R. Ivison, K. Kohno, Y. Tamura, M. Kubo, D. Iono, B. Hatsukade, K. Nakanishi, R. Kawabe, T. Nagao, A. K. Inoue, T. T. Takeuchi, M. Lee, Y. Ao, S. Fujimoto, T. Izumi, Y. Yamaguchi, S. Ikarashi, and T. Yamada. ALMA deep field in SSA22: Blindly detected CO emitters and [C II] emitter candidates. *Publications of the Astronomical Society of Japan*, 69:45, June 2017. doi: 10.1093/pasj/psx018.

[146] Shoubaneh Hemmati, Lin Yan, Tanio Diaz-Santos, Lee Armus, Peter Capak, Andreas Faisst, and Daniel Masters. The local [cii] 158 nm emission line luminosity function. *The Astrophysical Journal*, 834(1):36, 2017. URL `http://stacks.iop.org/0004-637X/834/i=1/a=36`.

[147] S. Doyle et al. Lumped element kinetic inductance detectors. *Journal of Low Temperature Physics*, 151(1):530–536, Apr 2008. ISSN 1573-7357. doi: 10.1007/s10909-007-9685-2. URL `https://doi.org/10.1007/s10909-007-9685-2`.

[148] S. Doyle et al. A review of the lumped element kinetic inductance detector. volume 7741, pages 7741 – 7741 – 10, 2010. doi: 10.1117/12.857341. URL `http://dx.doi.org/10.1117/12.857341`.

[149] R. Adam, A. Adane, P. A. R. Ade, P. André, A. Andrianasolo, H. Aussel, A. Beelen, A. Benoit, A. Bideaud, N. Billot, O. Bourrion, A. Bracco, M. Calvo, A. Catalano, G. Coiffard, B. Comis, M. De Petris, F.-X. Désert, S. Doyle, E. F. C. Driessen, R. Evans, J. Goupy, C. Kramer, G. Lagache, S. Leclercq, J.-P. Leggeri, J.-F. Lestrade, J.-F. Macias-Perez, P. Mauskopf, F. Mayet, A. Maury, A. Monfardini, S. Navarro, E. Pascale, L. Perotto, G. Pisano, N. Ponthieu, V. Reveret, A. Rigby, A. Ritacco, C. Romero, H. Roussel, F. Ruppin, K. Schuster, A. Sievers, S. Triqueneaux, C. Tucker, and R. Zylka. The NIKA2 large field-of-view millimeter continuum camera for the 30-m IRAM telescope. *ArXiv e-prints*, July 2017.

[150] P. A. R. Ade et al. Planck 2013 results. XVIII. The gravitational lensing-infrared background correlation. *Astron. Astrophys.*, 571:A18, 2014. doi: 10.1051/0004-6361/201321540.

[151] E. Visbal and A. Loeb. Measuring the 3D clustering of undetected galaxies through cross correlation of their cumulative flux fluctuations from multiple spectral lines. *JCAP* , 11:016, November 2010. doi: 10.1088/1475-7516/2010/11/016.

[152] Matthieu Bethermin, Hao-Yi Wu, Guilaine Lagache, Iary Davidzon, Nicolas Ponthieu, Morgane Cousin, Lingyu Wang, Olivier Dore, Emanuele Daddi, and Andrea Lapi. The impact of clustering and angular resolution on far-infrared and millimeter continuum observations. 2017.

[153] Y. Matsuda, T. Nagao, D. Iono, B. Hatsukade, K. Kohno, Y. Tamura, Y. Yamaguchi, and I. Shimizu. The ALMA Patchy Deep Survey: a blind search for [C II] emitters at z 4.5. *Mon. Not. Roy. Astron. Soc.*, 451:1141–1145, July 2015. doi: 10.1093/mnras/stv1044.

[154] G. C. Bower, G. K. Keating, D. P. Marrone, and S. T. YT Lee Array Team. Cosmic Structure and Galaxy Evolution through Intensity Mapping of Molecular Gas. In *American Astronomical Society Meeting Abstracts*, volume 227 of *American Astronomical Society Meeting Abstracts*, page 426.04, January 2016.

[155] K. Cleary, M.-A. Bigot-Sazy, D. Chung, S. E. Church, C. Dickinson, H. Eriksen, t. gaier, P. Goldsmith, J. O. Gundersen, S. Harper, A. I. Harris, J. Lamb, T. Li, R. Munroe, T. J. Pearson, A. C. S. Readhead, R. H. Wechsler, I. Kathrine Wehus, and D. Woody. The CO Mapping Array Pathfinder (COMAP). In *American Astronomical Society Meeting Abstracts*, volume 227 of *American Astronomical Society Meeting Abstracts*, page 426.06, January 2016.

[156] B. D. Uzgil, J. E. Aguirre, C. M. Bradford, and A. Lidz. Measuring Galaxy Clustering and the Evolution of [C II] Mean Intensity with Far-IR Line Intensity Mapping during 0.5 ¡ z ¡ 1.5. *Ap. J.* , 793:116, October 2014. doi: 10.1088/0004-637X/793/2/116.

[157] A. Barlis, S. Hailey-Dunsheath, C. M. Bradford, C. McKenney, H. G. Le Duc, and J. Aguirre. Development of low-noise kinetic inductance detectors for far-infrared astrophysics. In *APS April Meeting Abstracts*, January 2017.

[158] C. Gruppioni, F. Pozzi, G. Rodighiero, I. Delvecchio, S. Berta, L. Pozzetti, G. Zamorani, P. Andreani, A. Cimatti, O. Ilbert, E. Le Floc'h, D. Lutz, B. Magnelli, L. Marchetti, P. Monaco, R. Nordon, S. Oliver, P. Popesso, L. Riguccini, I. Roseboom, D. J. Rosario, M. Sargent, M. Vaccari, B. Altieri,

H. Aussel, A. Bongiovanni, J. Cepa, E. Daddi, H. Domínguez-Sánchez, D. Elbaz, N. Förster Schreiber, R. Genzel, A. Iribarrem, M. Magliocchetti, R. Maiolino, A. Poglitsch, A. Pérez García, M. Sanchez-Portal, E. Sturm, L. Tacconi, I. Valtchanov, A. Amblard, V. Arumugam, M. Bethermin, J. Bock, A. Boselli, V. Buat, D. Burgarella, N. Castro-Rodríguez, A. Cava, P. Chanial, D. L. Clements, A. Conley, A. Cooray, C. D. Dowell, E. Dwek, S. Eales, A. Franceschini, J. Glenn, M. Griffin, E. Hatziminaoglou, E. Ibar, K. Isaak, R. J. Ivison, G. Lagache, L. Levenson, N. Lu, S. Madden, B. Maffei, G. Mainetti, H. T. Nguyen, B. O'Halloran, M. J. Page, P. Panuzzo, A. Papageorgiou, C. P. Pearson, I. Pérez-Fournon, M. Pohlen, D. Rigopoulou, M. Rowan-Robinson, B. Schulz, D. Scott, N. Seymour, D. L. Shupe, A. J. Smith, J. A. Stevens, M. Symeonidis, M. Trichas, K. E. Tugwell, L. Vigroux, L. Wang, G. Wright, C. K. Xu, M. Zemcov, S. Bardelli, M. Carollo, T. Contini, O. Le Févre, S. Lilly, V. Mainieri, A. Renzini, M. Scodeggio, and E. Zucca. The Herschel PEP/HerMES luminosity function - I. Probing the evolution of PACS selected Galaxies to z $<$ 4. *Mon. Not. Roy. Astron. Soc.*, 432:23–52, June 2013. doi: 10.1093/mnras/stt308.

[159] L. Spinoglio, K. M. Dasyra, A. Franceschini, C. Gruppioni, E. Valiante, and K. Isaak. Far-IR/Submillimeter Spectroscopic Cosmological Surveys: Predictions of Infrared Line Luminosity Functions for z $<$ 4 Galaxies. *Ap. J.* , 745:171, February 2012. doi: 10.1088/0004-637X/745/2/171.

[160] T. Nakagawa, H. Shibai, H. Kaneda, K. Kohno, H. Matsuhara, H. Ogawa, T. Onaka, P. Roelfsema, and SPICA Team. The Next-Generation Infrared Space Mission Spica: Project Updates. *Publication of Korean Astronomical Society*, 32:331–335, March 2017. doi: 10.5303/PKAS.2017.32.1.331.

[161] C. M. Bradford, P. F. Goldsmith, A. Bolatto, L. Armus, J. Bauer, P. Appleton, A. Cooray, C. Casey, D. Dale, B. Uzgil, J. Aguirre, J. D. Smith, K. Sheth, E. J. Murphy, C. McKenney, W. Holmes, M. Rizzo, E. Bergin, and G. Stacey. A Cryogenic Space Telescope for Far-Infrared Astrophysics: A Vision for NASA in the 2020 Decade. *ArXiv e-prints*, May 2015.

[162] Natalie Mashian, Avi Loeb, and Amiel Sternberg. Spectral Distortion of the CMB by the Cumulative CO Emission from Galaxies throughout Cosmic History. *Mon. Not. Roy. Astron. Soc.*, 458(1):L99–L103, 2016. doi: 10.1093/mnrasl/slw027.

[163] C. L. Carilli, J. Chluba, R. Decarli, F. Walter, M. Aravena, J. Wagg, G. Popping, P. Cortes, J. Hodge, A. Weiss, F. Bertoldi, and D. Riechers. The ALMA Spectroscopic Survey in the Hubble Ultra Deep Field: Implications for Spectral Line Intensity Mapping at Millimeter Wavelengths and CMB Spectral Distortions. *Ap. J.* , 833:73, December 2016. doi: 10.3847/1538-4357/833/1/73.

[164] Eric R. Switzer. Tracing the cosmological evolution of stars and cold gas with CMB spectral surveys. *Astrophys. J.*, 838(2):82, 2017. doi: 10.3847/1538-4357/aa6576.

[165] A. Cooray, J. J. Bock, B. Keating, A. E. Lange, and T. Matsumoto. First Star Signature in Infrared Background Anisotropies. *Ap. J.* , 606:611–624, May 2004. doi: 10.1086/383137.

[166] A. Kashlinsky, R. Arendt, J. P. Gardner, J. C. Mather, and S. H. Moseley. Detecting Population III Stars through Observations of Near-Infrared Cosmic Infrared Background Anisotropies. *Ap. J.* , 608: 1–9, June 2004. doi: 10.1086/386365.

[167] James Bock et al. The cosmic infrared background experiment. *New Astron. Rev.*, 50:215–220, 2006. doi: 10.1016/j.newar.2005.11.034.

[168] M. Zemcov, T. Arai, J. Battle, J. Bock, A. Cooray, V. Hristov, B. Keating, M. G. Kim, D. H. Lee, L. R. Levenson, P. Mason, T. Matsumoto, S. Matsuura, U. W. Nam, T. Renbarger, I. Sullivan, K. Suzuki, K. Tsumura, and T. Wada. The Cosmic Infrared Background Experiment (CIBER): A Sounding Rocket Payload to Study the near Infrared Extragalactic Background Light. *Ap. J. Suppl.* , 207:31, August 2013. doi: 10.1088/0067-0049/207/2/31.

[169] M. Zemcov, J. Smidt, T. Arai, J. Bock, A. Cooray, Y. Gong, M. G. Kim, P. Korngut, A. Lam, D. H. Lee, T. Matsumoto, S. Matsuura, U. W. Nam, G. Roudier, K. Tsumura, and T. Wada. On the origin of near-infrared extragalactic background light anisotropy. *Science*, 346:732–735, November 2014. doi: 10.1126/science.1258168.

[170] A. Lanz, T. Arai, J. Battle, J. Bock, A. Cooray, V. Hristov, P. Korngut, D. H. Lee, P. Mason, T. Matsumoto, S. Matsuura, T. Morford, Y. Onishi, M. Shirahata, K. Tsumura, T. Wada, and M. Zemcov. Studying extragalactic background fluctuations with the Cosmic Infrared Background ExpeRiment 2 (CIBER-2). In *Space Telescopes and Instrumentation 2014: Optical, Infrared, and Millimeter Wave*, volume 9143 of *Proc.SPIE*, page 91433N, August 2014. doi: 10.1117/12.2057304.

[171] K. Helgason, M. Ricotti, and A. Kashlinsky. Reconstructing the Near-infrared Background Fluctuations from Known Galaxy Populations Using Multiband Measurements of Luminosity Functions. *Ap. J.* , 752:113, June 2012. doi: 10.1088/0004-637X/752/2/113.

[172] K. Mitchell-Wynne, A. Cooray, Y. Gong, M. Ashby, T. Dolch, H. Ferguson, S. Finkelstein, N. Grogin, D. Kocevski, A. Koekemoer, J. Primack, and J. Smidt. Ultraviolet luminosity density of the universe during the epoch of reionization. *Nature Communications*, 6:7945, September 2015. doi: 10.1038/ncomms8945.

[173] R. I. Thompson, D. Eisenstein, X. Fan, M. Rieke, and R. C. Kennicutt. Evidence for a z ¡ 8 Origin of the Source-subtracted Near-Infrared Background. *Ap. J.* , 666:658–662, September 2007. doi: 10.1086/520634.

[174] A. Kashlinsky, R. G. Arendt, M. L. N. Ashby, G. G. Fazio, J. Mather, and S. H. Moseley. New Measurements of the Cosmic Infrared Background Fluctuations in Deep Spitzer/IRAC Survey Data and Their Cosmological Implications. *Ap. J.* , 753:63, July 2012. doi: 10.1088/0004-637X/753/1/63.

[175] A. Cooray, J. Smidt, F. de Bernardis, Y. Gong, D. Stern, M. L. N. Ashby, P. R. Eisenhardt, C. C. Frazer, A. H. Gonzalez, C. S. Kochanek, S. Kozłowski, and E. L. Wright. Near-infrared background anisotropies from diffuse intrahalo light of galaxies. *Nature*, 490:514–516, October 2012. doi: 10.1038/nature11474.

[176] T. Matsumoto, H. J. Seo, W.-S. Jeong, H. M. Lee, S. Matsuura, H. Matsuhara, S. Oyabu, J. Pyo, and T. Wada. AKARI Observation of the Fluctuation of the Near-infrared Background. *Ap. J.* , 742:124, December 2011. doi: 10.1088/0004-637X/742/2/124.

[177] Bruce A. Bassett and Renee Hlozek. Baryon Acoustic Oscillations. 2009.

[178] Jeffrey B. Peterson, Kevin Bandura, and Ue Li Pen. The Hubble Sphere Hydrogen Survey. In *Proceedings, 41st Rencontres de Moriond, 2006 Contents and structure of the universe: La Thuile, Val d'Aoste, Italy, Mar 18-25, 2006*, pages 283–289, 2006. URL `https://inspirehep.net/record/718577/files/Pages_from_C06-03-18--2_283.pdf`.

[179] H.-J. Seo, S. Dodelson, J. Marriner, D. Mcginnis, A. Stebbins, C. Stoughton, and A. Vallinotto. A Ground-based 21 cm Baryon Acoustic Oscillation Survey. *Ap. J.* , 721:164–173, September 2010. doi: 10.1088/0004-637X/721/1/164.

[180] J. Richard Shaw, Kris Sigurdson, Ue-Li Pen, Albert Stebbins, and Michael Sitwell. All-Sky Interferometry with Spherical Harmonic Transit Telescopes. *Astrophys. J.*, 781:57, 2014. doi: 10.1088/0004-637X/781/2/57.

[181] J. Richard Shaw, Kris Sigurdson, Michael Sitwell, Albert Stebbins, and Ue-Li Pen. Coaxing cosmic 21 cm fluctuations from the polarized sky using m-mode analysis. *Phys. Rev.*, D91(8):083514, 2015. doi: 10.1103/PhysRevD.91.083514.

[182] T.-C. Chang, U.-L. Pen, K. Bandura, and J. B. Peterson. Hydrogen 21-cm Intensity Mapping at redshift 0.8. *ArXiv e-prints*, July 2010.

[183] K. W. Masui, E. R. Switzer, N. Banavar, K. Bandura, C. Blake, L.-M. Calin, T.-C. Chang, X. Chen, Y.-C. Li, Y.-W. Liao, A. Natarajan, U.-L. Pen, J. B. Peterson, J. R. Shaw, and T. C. Voytek. Measurement of 21 cm Brightness Fluctuations at z ˜ 0.8 in Cross-correlation. *Ap. J. Lett.*, 763:L20, January 2013. doi: 10.1088/2041-8205/763/1/L20.

[184] Laura B. Newburgh et al. Calibrating CHIME, A New Radio Interferometer to Probe Dark Energy. *Proc. SPIE Int. Soc. Opt. Eng.*, 9145:4V, 2014. doi: 10.1117/12.2056962.

[185] Philippe Berger et al. Holographic Beam Mapping of the CHIME Pathfinder Array. *Proc. SPIE Int. Soc. Opt. Eng.*, 9906:99060D, 2016. doi: 10.1117/12.2233782.

[186] K. Bandura, G. E. Addison, M. Amiri, J. R. Bond, D. Campbell-Wilson, L. Connor, J.-F. Cliche, G. Davis, M. Deng, N. Denman, M. Dobbs, M. Fandino, K. Gibbs, A. Gilbert, M. Halpern, D. Hanna, A. D. Hincks, G. Hinshaw, C. Höfer, P. Klages, T. L. Landecker, K. Masui, J. Mena Parra, L. B. Newburgh, U.-l. Pen, J. B. Peterson, A. Recnik, J. R. Shaw, K. Sigurdson, M. Sitwell, G. Smecher, R. Smegal, K. Vanderlinde, and D. Wiebe. Canadian Hydrogen Intensity Mapping Experiment (CHIME) pathfinder. In *Ground-based and Airborne Telescopes V*, volume 9145 of *Proc.SPIE*, page 914522, July 2014. doi: 10.1117/12.2054950.

[187] D. C. Jacobs, J. Burba, J. Bowman, A. R. Neben, B. Stinnett, and L. Turner. The External Calibrator for Hydrogen Observatories. 2016.

[188] P. Bull, P. G. Ferreira, P. Patel, and M. G. Santos. Late-time cosmology with 21cm intensity mapping experiments. *ArXiv e-prints*, May 2014.

[189] P. Bull. Extending Cosmological Tests of General Relativity with the Square Kilometre Array. *Ap. J.* , 817:26, January 2016. doi: 10.3847/0004-637X/817/1/26.

[190] J. Fonseca, S. Camera, M. G. Santos, and R. Maartens. Hunting Down Horizon-scale Effects with Multi-wavelength Surveys. *Ap. J. Lett.*, 812:L22, October 2015. doi: 10.1088/2041-8205/812/2/L22.

[191] M. Santos and et al. A large sky survey with MeerKAT. *PoS*, art. 00, September 2017.

[192] Mario G. Santos et al. MeerKLASS: MeerKAT Large Area Synoptic Survey. 2017. URL `https://inspirehep.net/record/1624378/files/arXiv:1709.06099.pdf`.

[193] A. Pourtsidou, D. Bacon, and R. Crittenden. H i and cosmological constraints from intensity mapping, optical and CMB surveys. *Mon. Not. Roy. Astron. Soc.*, 470:4251–4260, October 2017. doi: 10.1093/mnras/stx1479.

[194] J. Fonseca, R. Maartens, and M. G. Santos. Probing the primordial Universe with MeerKAT and DES. *Mon. Not. Roy. Astron. Soc.*, 466:2780–2786, April 2017. doi: 10.1093/mnras/stw3248.

[195] R. A. Battye, I. W. A. Browne, C. Dickinson, G. Heron, B. Maffei, and A. Pourtsidou. H I intensity mapping: a single dish approach. *Mon. Not. Roy. Astron. Soc.*, 434:1239–1256, September 2013. doi: 10.1093/mnras/stt1082.

[196] M.-A. Bigot-Sazy, Y.-Z. Ma, R. A. Battye, I. W. A. Browne, T. Chen, C. Dickinson, S. Harper, B. Maffei, L. C. Olivari, and P. N. Wilkinsondagger. HI Intensity Mapping with FAST. In L. Qain and D. Li, editors, *Frontiers in Radio Astronomy and FAST Early Sciences Symposium 2015*, volume 502 of *Astronomical Society of the Pacific Conference Series*, page 41, February 2016.

[197] M.-A. Bigot-Sazy, C. Dickinson, R. A. Battye, I. W. A. Browne, Y.-Z. Ma, B. Maffei, F. Noviello, M. Remazeilles, and P. N. Wilkinson. Simulations for single-dish intensity mapping experiments. *Mon. Not. Roy. Astron. Soc.*, 454:3240–3253, December 2015. doi: 10.1093/mnras/stv2153.

[198] Eli Visbal and Abraham Loeb. Measuring the 3D Clustering of Undetected Galaxies Through Cross Correlation of their Cumulative Flux Fluctuations from Multiple Spectral Lines. *JCAP*, 1011:016, 2010. doi: 10.1088/1475-7516/2010/11/016.

[199] A. R. Pullen, T.-C. Chang, O. Doré, and A. Lidz. Cross-correlations as a Cosmological Carbon Monoxide Detector. *Ap. J.* , 768:15, May 2013. doi: 10.1088/0004-637X/768/1/15.

[200] P. C. Breysse, E. D. Kovetz, and M. Kamionkowski. Carbon monoxide intensity mapping at moderate redshifts. *Mon. Not. Roy. Astron. Soc.*, 443:3506–3512, October 2014. doi: 10.1093/mnras/stu1312.

[201] Adam Lidz and Jessie Taylor. On Removing Interloper Contamination from Intensity Mapping Power Spectrum Measurements. *Astrophys. J.*, 825:143, 2016. doi: 10.3847/0004-637X/825/2/143.

[202] Y.-T. Cheng, T.-C. Chang, J. Bock, C. M. Bradford, and A. Cooray. Spectral Line De-confusion in an Intensity Mapping Survey. *ArXiv e-prints*, April 2016.

[203] G. Popping, E. van Kampen, R. Decarli, M. Spaans, R. S. Somerville, and S. C. Trager. Sub-mm emission line deep fields: CO and [C II] luminosity functions out to z = 6. *Mon. Not. Roy. Astron. Soc.*, 461:93–110, September 2016. doi: 10.1093/mnras/stw1323.

[204] P. F. Hopkins, D. Kereš, J. Oñorbe, C.-A. Faucher-Giguère, E. Quataert, N. Murray, and J. S. Bullock. Galaxies on FIRE (Feedback In Realistic Environments): stellar feedback explains cosmologically inefficient star formation. *Mon. Not. Roy. Astron. Soc.*, 445:581–603, November 2014. doi: 10.1093/mnras/stu1738.

[205] A. Boselli, G. Gavazzi, J. Lequeux, and D. Pierini. [CII] at 158 mu m as a star formation tracer in late-type galaxies. *A & A* , 385:454–463, April 2002. doi: 10.1051/0004-6361:20020156.

[206] I. De Looze, M. Baes, G. J. Bendo, L. Cortese, and J. Fritz. The reliability of [C II] as an indicator of the star formation rate. *Mon. Not. Roy. Astron. Soc.*, 416:2712–2724, October 2011. doi: 10.1111/j.1365-2966.2011.19223.x.

[207] E. Wisnioski, N. M. Förster Schreiber, S. Wuyts, E. Wuyts, K. Bandara, D. Wilman, R. Genzel, R. Bender, R. Davies, M. Fossati, P. Lang, J. T. Mendel, A. Beifiori, G. Brammer, J. Chan, M. Fabricius, Y. Fudamoto, S. Kulkarni, J. Kurk, D. Lutz, E. J. Nelson, I. Momcheva, D. Rosario, R. Saglia, S. Seitz, L. J. Tacconi, and P. G. van Dokkum. The KMOS^{3D} Survey: Design, First Results, and the Evolution of Galaxy Kinematics from 0.7 ¡= z ¡= 2.7. *Ap. J.* , 799:209, February 2015. doi: 10.1088/0004-637X/799/2/209.

[208] R. Herrera-Camus, A. D. Bolatto, M. G. Wolfire, J. D. Smith, K. V. Croxall, R. C. Kennicutt, D. Calzetti, G. Helou, F. Walter, A. K. Leroy, B. Draine, B. R. Brandl, L. Armus, K. M. Sandstrom, D. A. Dale, G. Aniano, S. E. Meidt, M. Boquien, L. K. Hunt, M. Galametz, F. S. Tabatabaei, E. J. Murphy, P. Appleton, H. Roussel, C. Engelbracht, and P. Beirao. [C II] 158 μm Emission as a Star Formation Tracer. *Ap. J.* , 800:1, February 2015. doi: 10.1088/0004-637X/800/1/1.

[209] A. Pallottini, A. Ferrara, S. Gallerani, S. Salvadori, and V. D'Odorico. Simulating cosmic metal enrichment by the first galaxies. *Mon. Not. Roy. Astron. Soc.*, 440:2498–2518, May 2014. doi: 10.1093/mnras/stu451.

[210] L. Vallini, S. Gallerani, A. Ferrara, A. Pallottini, and B. Yue. On the [CII]-SFR Relation in High Redshift Galaxies. *Ap. J.* , 813:36, November 2015. doi: 10.1088/0004-637X/813/1/36.

[211] A. D. Bolatto, M. Wolfire, and A. K. Leroy. The CO-to-H_2 Conversion Factor. *Ann. Rev. Astron. Astroph.*, 51:207–268, August 2013. doi: 10.1146/annurev-astro-082812-140944.

[212] M. Righi, C. Hernández-Monteagudo, and R. A. Sunyaev. Carbon monoxide line emission as a CMB foreground: tomography of the star-forming universe with different spectral resolutions. *A & A* , 489: 489–504, October 2008. doi: 10.1051/0004-6361:200810199.

[213] C. L. Carilli. Intensity Mapping of Molecular Gas During Cosmic Reionization. *Ap. J. Lett.*, 730:L30, April 2011. doi: 10.1088/2041-8205/730/2/L30.

[214] A. W. Blain, V. E. Barnard, and S. C. Chapman. Submillimetre and far-infrared spectral energy distributions of galaxies: the luminosity-temperature relation and consequences for photometric redshifts. *Mon. Not. Roy. Astron. Soc.*, 338:733–744, January 2003. doi: 10.1046/j.1365-8711.2003.06086.x.

[215] R. C. Kennicutt, Jr. Star Formation in Galaxies Along the Hubble Sequence. *Ann. Rev. Astron. Astroph.*, 36:189–232, 1998. doi: 10.1146/annurev.astro.36.1.189.

[216] G. Chabrier. Galactic Stellar and Substellar Initial Mass Function. *Publ. Astron. Soc. Pac.*, 115: 763–795, July 2003. doi: 10.1086/376392.

[217] E. Daddi, D. Elbaz, F. Walter, F. Bournaud, F. Salmi, C. Carilli, H. Dannerbauer, M. Dickinson, P. Monaco, and D. Riechers. Different Star Formation Laws for Disks Versus Starbursts at Low and High Redshifts. *Ap. J. Lett.*, 714:L118–L122, May 2010. doi: 10.1088/2041-8205/714/1/L118.

[218] C. L. Carilli and F. Walter. Cool Gas in High-Redshift Galaxies. *Ann. Rev. Astron. Astroph.*, 51: 105–161, August 2013. doi: 10.1146/annurev-astro-082812-140953.

[219] M. Dessauges-Zavadsky, M. Zamojski, D. Schaerer, F. Combes, E. Egami, A. M. Swinbank, J. Richard, P. Sklias, T. D. Rawle, M. Rex, J.-P. Kneib, F. Boone, and A. Blain. Molecular gas content in strongly lensed z ˜ 1.5-3 star-forming galaxies with low infrared luminosities. *A & A* , 577:A50, May 2015. doi: 10.1051/0004-6361/201424661.

[220] T. R. Greve, I. Leonidaki, E. M. Xilouris, A. Weiß, Z.-Y. Zhang, P. van der Werf, S. Aalto, L. Armus, T. Díaz-Santos, A. S. Evans, J. Fischer, Y. Gao, E. González-Alfonso, A. Harris, C. Henkel, R. Meijerink, D. A. Naylor, H. A. Smith, M. Spaans, G. J. Stacey, S. Veilleux, and F. Walter. Star Formation Relations and CO Spectral Line Energy Distributions across the J-ladder and Redshift. *Ap. J.* , 794:142, October 2014. doi: 10.1088/0004-637X/794/2/142.

[221] P. S. Behroozi, R. H. Wechsler, and C. Conroy. The Average Star Formation Histories of Galaxies in Dark Matter Halos from z = 0-8. *Ap. J.* , 770:57, June 2013. doi: 10.1088/0004-637X/770/1/57.

[222] H.-Y. Wu and O. Doré. A minimal empirical model for the cosmic far-infrared background anisotropies. *Mon. Not. Roy. Astron. Soc.*, 466:4651–4658, April 2017. doi: 10.1093/mnras/stx024.

[223] M. P. Viero, L. Moncelsi, R. F. Quadri, V. Arumugam, R. J. Assef, M. Béthermin, J. Bock, C. Bridge, C. M. Casey, A. Conley, A. Cooray, D. Farrah, J. Glenn, S. Heinis, E. Ibar, S. Ikarashi, R. J. Ivison, K. Kohno, G. Marsden, S. J. Oliver, I. G. Roseboom, B. Schulz, D. Scott, P. Serra, M. Vaccari, J. D. Vieira, L. Wang, J. Wardlow, G. W. Wilson, M. S. Yun, and M. Zemcov. HerMES: The Contribution to the Cosmic Infrared Background from Galaxies Selected by Mass and Redshift. *Ap. J.* , 779:32, December 2013. doi: 10.1088/0004-637X/779/1/32.

[224] C. Laigle, H. J. McCracken, O. Ilbert, B. C. Hsieh, I. Davidzon, P. Capak, G. Hasinger, J. D. Silverman, C. Pichon, J. Coupon, H. Aussel, D. Le Borgne, K. Caputi, P. Cassata, Y.-Y. Chang, F. Civano, J. Dunlop, J. Fynbo, J. S. Kartaltepe, A. Koekemoer, O. Le Fèvre, E. Le Floc'h, A. Leauthaud, S. Lilly, L. Lin, S. Marchesi, B. Milvang-Jensen, M. Salvato, D. B. Sanders, N. Scoville, V. Smolcic, M. Stockmann, Y. Taniguchi, L. Tasca, S. Toft, M. Vaccari, and J. Zabl. The COSMOS2015 Catalog: Exploring the 1 ¡ z ¡ 6 Universe with Half a Million Galaxies. *Ap. J. Suppl.* , 224:24, June 2016. doi: 10.3847/0067-0049/224/2/24.

[225] G. Sun, L. Moncelsi, M. P. Viero, J. Bock, C. M. Bradford, T.-C. Chang, Y.-T. Cheng, A. Cooray, A. Crites, S. Hailey-Dunsheath, J. Hunacek, M. B. Silva, B. Uzgil, and M. Zemcov. A Foreground Removal Strategy for Future [CII] Intensity Mapping Experiments Using Galaxies Selected by Stellar Mass and Redshift. *ArXiv e-prints*, October 2016.

[226] M. Ouchi, K. Shimasaku, M. Akiyama, C. Simpson, T. Saito, Y. Ueda, H. Furusawa, K. Sekiguchi, T. Yamada, T. Kodama, N. Kashikawa, S. Okamura, M. Iye, T. Takata, M. Yoshida, and M. Yoshida. The Subaru/XMM-Newton Deep Survey (SXDS). IV. Evolution of Lyα Emitters from z = 3.1 to 5.7 in the 1 deg^2 Field: Luminosity Functions and AGN. *Ap. J. Suppl.* , 176:301-330, June 2008. doi: 10.1086/527673.

[227] J. Matthee, D. Sobral, S. Santos, H. Röttgering, B. Darvish, and B. Mobasher. Identification of the brightest Lyα emitters at z = 6.6: implications for the evolution of the luminosity function in the reionization era. *Mon. Not. Roy. Astron. Soc.*, 451:400–417, July 2015. doi: 10.1093/mnras/stv947.

[228] P. Dayal, A. Maselli, and A. Ferrara. The visibility of Lyman α emitters during reionization. *Mon. Not. Roy. Astron. Soc.*, 410:830–843, January 2011. doi: 10.1111/j.1365-2966.2010.17482.x.

[229] A. R. Pullen, O. Doré, and J. Bock. Intensity Mapping across Cosmic Times with the Lyα Line. *Ap. J.* , 786:111, May 2014. doi: 10.1088/0004-637X/786/2/111.

[230] P. Comaschi and A. Ferrara. Empowering line intensity mapping to study early galaxies. *Mon. Not. Roy. Astron. Soc.*, 463:3078–3082, December 2016. doi: 10.1093/mnras/stw2199.

[231] P. Comaschi, B. Yue, and A. Ferrara. Observational challenges in Lyα intensity mapping. *Mon. Not. Roy. Astron. Soc.*, 463:3193–3203, December 2016. doi: 10.1093/mnras/stw2198.

[232] O. Doré, J. Bock, M. Ashby, P. Capak, A. Cooray, R. de Putter, T. Eifler, N. Flagey, Y. Gong, S. Habib, K. Heitmann, C. Hirata, W.-S. Jeong, R. Katti, P. Korngut, E. Krause, D.-H. Lee, D. Masters, P. Mauskopf, G. Melnick, B. Mennesson, H. Nguyen, K. Öberg, A. Pullen, A. Raccanelli, R. Smith, Y.-S. Song, V. Tolls, S. Unwin, T. Venumadhav, M. Viero, M. Werner, and M. Zemcov. Cosmology with the SPHEREX All-Sky Spectral Survey. *ArXiv e-prints*, December 2014.

[233] J. S. Bagla, N. Khandai, and K. K. Datta. HI as a probe of the large-scale structure in the post-reionization universe. *Mon. Not. Roy. Astron. Soc.*, 407:567–580, September 2010. doi: 10.1111/j.1365-2966.2010.16933.x.

[234] F. Villaescusa-Navarro, S. Planelles, S. Borgani, M. Viel, E. Rasia, G. Murante, K. Dolag, L. K. Steinborn, V. Biffi, A. M. Beck, and C. Ragone-Figueroa. Neutral hydrogen in galaxy clusters: impact of AGN feedback and implications for intensity mapping. *Mon. Not. Roy. Astron. Soc.*, 456:3553–3570, March 2016. doi: 10.1093/mnras/stv2904.

[235] H. Padmanabhan, A. Refregier, and A. Amara. A halo model for cosmological neutral hydrogen : abundances and clustering. *Mon. Not. Roy. Astron. Soc.*, 469:2323–2334, August 2017. doi: 10.1093/mnras/stx979.

[236] A. Pénin, O. Umeh, and M. Santos. A scale dependent bias on linear scales: the case for HI intensity mapping at z=1. *ArXiv e-prints*, June 2017.

[237] A. M. Martin, R. Giovanelli, M. P. Haynes, and L. Guzzo. The Clustering Characteristics of H I-selected Galaxies from the 40% ALFALFA Survey. *Ap. J.* , 750:38, May 2012. doi: 10.1088/0004-637X/750/1/38.

[238] D. Sarkar, S. Bharadwaj, and S. Anathpindika. Modelling the post-reionization neutral hydrogen (H I) bias. *Mon. Not. Roy. Astron. Soc.*, 460:4310–4319, August 2016. doi: 10.1093/mnras/stw1111.

[239] O. Umeh, R. Maartens, and M. Santos. Nonlinear modulation of the HI power spectrum on ultra-large scales. I. *JCAP* , 3:061, March 2016. doi: 10.1088/1475-7516/2016/03/061.

[240] O. Umeh. Imprint of non-linear effects on HI intensity mapping on large scales. *JCAP* , 6:005, June 2017. doi: 10.1088/1475-7516/2017/06/005.

[241] R. S. Somerville and R. Davé. Physical Models of Galaxy Formation in a Cosmological Framework. *Ann. Rev. Astron. Astroph.*, 53:51–113, August 2015. doi: 10.1146/annurev-astro-082812-140951.

[242] J. Fu, Q. Guo, G. Kauffmann, and M. R. Krumholz. The atomic-to-molecular transition and its relation to the scaling properties of galaxy discs in the local Universe. *Mon. Not. Roy. Astron. Soc.*, 409:515–530, December 2010. doi: 10.1111/j.1365-2966.2010.17342.x.

[243] J. Fu, G. Kauffmann, C. Li, and Q. Guo. The effect of star formation on the redshift evolution of interstellar metals, atomic and molecular gas in galaxies. *Mon. Not. Roy. Astron. Soc.*, 424:2701–2714, August 2012. doi: 10.1111/j.1365-2966.2012.21356.x.

[244] C. D. P. Lagos, C. G. Lacey, C. M. Baugh, R. G. Bower, and A. J. Benson. On the impact of empirical and theoretical star formation laws on galaxy formation. *Mon. Not. Roy. Astron. Soc.*, 416:1566–1584, September 2011. doi: 10.1111/j.1365-2966.2011.19160.x.

[245] C. d. P. Lagos, E. Bayet, C. M. Baugh, C. G. Lacey, T. A. Bell, N. Fanidakis, and J. E. Geach. Predictions for the CO emission of galaxies from a coupled simulation of galaxy formation and photon-dominated regions. *Mon. Not. Roy. Astron. Soc.*, 426:2142–2165, November 2012. doi: 10.1111/j.1365-2966.2012.21905.x.

[246] G. Popping, R. S. Somerville, and S. C. Trager. Evolution of the atomic and molecular gas content of galaxies. *Mon. Not. Roy. Astron. Soc.*, 442:2398–2418, August 2014. doi: 10.1093/mnras/stu991.

[247] J. P. Pérez-Beaupuits, K. Wada, and M. Spaans. The Structure and Dynamics of An Active Galactic Nucleus Torus: CO Line Predictions for ALMA from Three-dimensional Hydrodynamical Simulations with X-ray-driven Chemistry. *Ap. J.* , 730:48, March 2011. doi: 10.1088/0004-637X/730/1/48.

[248] D. Narayanan and M. R. Krumholz. A physical model for the [C ii]-FIR deficit in luminous galaxies. *Mon. Not. Roy. Astron. Soc.*, 467:50–67, May 2017. doi: 10.1093/mnras/stw3218.

[249] A. Mesinger and S. Furlanetto. Efficient Simulations of Early Structure Formation and Reionization. *Ap. J.* , 669:663–675, November 2007. doi: 10.1086/521806.

[250] M. G. Santos, L. Ferramacho, M. B. Silva, A. Amblard, and A. Cooray. Fast large volume simulations of the 21-cm signal from the reionization and pre-reionization epochs. *Mon. Not. Roy. Astron. Soc.*, 406:2421–2432, August 2010. doi: 10.1111/j.1365-2966.2010.16898.x.

[251] S. Hassan, R. Davé, K. Finlator, and M. G. Santos. Simulating the 21 cm signal from reionization including non-linear ionizations and inhomogeneous recombinations. *Mon. Not. Roy. Astron. Soc.*, 457:1550–1567, April 2016. doi: 10.1093/mnras/stv3001.

[252] D. Narayanan, C. E. Groppi, C. A. Kulesa, and C. K. Walker. Warm, Dense Molecular Gas in the ISM of Starbursts, LIRGs, and ULIRGs. *Ap. J.* , 630:269–279, September 2005. doi: 10.1086/431171.

[253] S. Juneau, D. T. Narayanan, J. Moustakas, Y. L. Shirley, R. S. Bussmann, R. C. Kennicutt, Jr., and P. A. Vanden Bout. Enhanced Dense Gas Fraction in Ultraluminous Infrared Galaxies. *Ap. J.* , 707: 1217-1232, December 2009. doi: 10.1088/0004-637X/707/2/1217.

[254] U. Lisenfeld, D. Espada, L. Verdes-Montenegro, N. Kuno, S. Leon, J. Sabater, N. Sato, J. Sulentic, S. Verley, and M. S. Yun. The AMIGA sample of isolated galaxies. IX. Molecular gas properties. *A & A* , 534:A102, October 2011. doi: 10.1051/0004-6361/201117056.

[255] P. P. Papadopoulos, P. P. van der Werf, E. M. Xilouris, K. G. Isaak, Y. Gao, and S. Mühle. The molecular gas in luminous infrared galaxies - I. CO lines, extreme physical conditions and their drivers. *Mon. Not. Roy. Astron. Soc.*, 426:2601–2629, November 2012. doi: 10.1111/j.1365-2966.2012.21001.x.

[256] D. Liu, Y. Gao, K. Isaak, E. Daddi, C. Yang, N. Lu, and P. van der Werf. High-J CO versus Far-infrared Relations in Normal and Starburst Galaxies. *Ap. J. Lett.*, 810:L14, September 2015. doi: 10.1088/2041-8205/810/2/L14.

[257] M. J. F. Rosenberg, P. P. van der Werf, S. Aalto, L. Armus, V. Charmandaris, T. Díaz-Santos, A. S. Evans, J. Fischer, Y. Gao, E. González-Alfonso, T. R. Greve, A. I. Harris, C. Henkel, F. P. Israel, K. G. Isaak, C. Kramer, R. Meijerink, D. A. Naylor, D. B. Sanders, H. A. Smith, M. Spaans, L. Spinoglio, G. J. Stacey, I. Veenendaal, S. Veilleux, F. Walter, A. Weiß, M. C. Wiedner, M. H. D. van der Wiel, and E. M. Xilouris. The Herschel Comprehensive (U)LIRG Emission Survey (HERCULES): CO Ladders, Fine Structure Lines, and Neutral Gas Cooling. *Ap. J.* , 801:72, March 2015. doi: 10.1088/0004-637X/801/2/72.

[258] J. Kamenetzky, N. Rangwala, J. Glenn, P. R. Maloney, and A. Conley. L'CO/LFIR Relations with CO Rotational Ladders of Galaxies Across the Herschel SPIRE Archive. *Ap. J.* , 829:93, October 2016. doi: 10.3847/0004-637X/829/2/93.

[259] A. Pallottini, A. Ferrara, S. Bovino, L. Vallini, S. Gallerani, R. Maiolino, and S. Salvadori. The impact of chemistry on the structure of high-z galaxies. *ArXiv e-prints*, July 2017.

[260] M. R. Krumholz, A. K. Leroy, and C. F. McKee. Which Phase of the Interstellar Medium Correlates with the Star Formation Rate? *Ap. J.* , 731:25, April 2011. doi: 10.1088/0004-637X/731/1/25.

[261] D. Narayanan, M. R. Krumholz, E. C. Ostriker, and L. Hernquist. A general model for the CO-H_2 conversion factor in galaxies with applications to the star formation law. *Mon. Not. Roy. Astron. Soc.*, 421:3127–3146, April 2012. doi: 10.1111/j.1365-2966.2012.20536.x.

[262] P. C. Breysse and M. Rahman. Feeding cosmic star formation: Exploring high-redshift molecular gas with CO intensity mapping. *ArXiv e-prints*, June 2016.

[263] L. Wolz, C. Tonini, C. Blake, and J. S. B. Wyithe. Intensity Mapping Cross-Correlations: Connecting the Largest Scales to Galaxy Evolution. *Mon. Not. Roy. Astron. Soc.*, 458(3):3399–3410, 2016. doi: 10.1093/mnras/stw535.

[264] Claudia del P Lagos, Robert A Crain, Joop Schaye, Michelle Furlong, Carlos S Frenk, Richard G Bower, Matthieu Schaller, Tom Theuns, James W Trayford, Yannick M Bahe, and Claudio Dalla Vecchia. Molecular hydrogen abundances of galaxies in the EAGLE simulations. *arXiv.org*, March 2015.

[265] Robert A Crain, Yannick M Bahe, Claudia del P Lagos, Alireza Rahmati, Joop Schaye, Ian G McCarthy, Antonino Marasco, Richard G Bower, Matthieu Schaller, Tom Theuns, and Thijs van der Hulst. The EAGLE simulations: atomic hydrogen associated with galaxies. *arXiv.org*, (4):4204–4226, April 2016.

[266] Steven Furlanetto and Adam Lidz. The Cross-Correlation of High-Redshift 21 cm and Galaxy Surveys. *Astrophys. J.*, 660:1030, 2007. doi: 10.1086/513009.

[267] Adam Lidz, Oliver Zahn, Steven Furlanetto, Matthew McQuinn, Lars Hernquist, and Matias Zaldarriaga. Probing Reionization with the 21 cm-Galaxy Cross Power Spectrum. *Astrophys. J.*, 690:252–266, 2009. doi: 10.1088/0004-637X/690/1/252.

[268] Yan Gong, Asantha Cooray, Marta B. Silva, Mario G. Santos, and Phillip Lubin. Probing Reionization with Intensity Mapping of Molecular and Fine Structure Lines. *Astrophys. J.*, 728:L46, 2011. doi: 10.1088/2041-8205/728/2/L46.

[269] Brant E. Robertson, Richard S. Ellis, Steven R. Furlanetto, and James S. Dunlop. Cosmic Reionization and Early Star-forming Galaxies: a Joint Analysis of new Constraints From Planck and the Hubble Space Telescope. *Astrophys. J.*, 802(2):L19, 2015. doi: 10.1088/2041-8205/802/2/L19.

[270] J. R. Bond and S. T. Myers. The Hierarchical peak patch picture of cosmic catalogs. 1. Algorithms. *Astrophys. J. Suppl.*, 103:1, 1996. doi: 10.1086/192267.

[271] Patrick C. Breysse, Ely D. Kovetz, Peter S. Behroozi, Liang Dai, and Marc Kamionkowski. Insights from probability distribution functions of intensity maps. *Mon. Not. Roy. Astron. Soc.*, 467:2996, 2017. doi: 10.1093/mnras/stx203.

[272] Patrick McDonald and Uros Seljak. How to measure redshift-space distortions without sample variance. *JCAP*, 0910:007, 2009. doi: 10.1088/1475-7516/2009/10/007.

[273] Lloyd Knox. Cosmic microwave background anisotropy observing strategy assessment. *Astrophys. J.*, 480:72, 1997. doi: 10.1086/303959.

[274] P. A. G. Scheuer. A statistical method for analysing observations of faint radio stars. *Proceedings of the Cambridge Philosophical Society*, 53:764–773, 1957. doi: 10.1017/S0305004100032825.

[275] X. Barcons, G. B. Raymont, R. S. Warwick, A. C. Fabian, K. O. Mason, I. McHardy, and M. Rowan-Robinson. Deep X-Ray Source Counts from a Fluctuation Analysis of ROSAT PSPC Images. *Mon. Not. Roy. Astron. Soc.*, 268:833, June 1994. doi: 10.1093/mnras/268.4.833.

[276] D. Windridge and S. Phillipps. A fluctuation analysis for optical cluster galaxies - I. Theory. *Mon. Not. Roy. Astron. Soc.*, 319:591–605, December 2000. doi: 10.1046/j.1365-8711.2000.03908.x.

[277] Samuel K. Lee, Shin'ichiro Ando, and Marc Kamionkowski. The Gamma-Ray-Flux Probability Distribution Function from Galactic Halo Substructure. *JCAP*, 0907:007, 2009. doi: 10.1088/1475-7516/2009/07/007.

[278] Guillaume Patanchon et al. Submillimeter Number Counts From Statistical Analysis of BLAST Maps. *Astrophys. J.*, 707:1750–1765, 2009. doi: 10.1088/0004-637X/707/2/1750.

[279] G. Sun, L. Moncelsi, M. P. Viero, J. Bock, C. M. Bradford, T.-C. Chang, Y.-T. Cheng, A. Cooray, A. Crites, S. Hailey-Dunsheath, J. Hunacek, M. B. Silva, B. Uzgil, and M. Zemcov. A Foreground Removal Strategy for Future [CII] Intensity Mapping Experiments Using Galaxies Selected by Stellar Mass and Redshift. *ArXiv e-prints*, October 2016.

[280] Yun-Ting Cheng, Tzu-Ching Chang, James Bock, C. Matt Bradford, and Asantha Cooray. Spectral Line De-confusion in an Intensity Mapping Survey. *Astrophys. J.*, 832(2):165, 2016. doi: 10.3847/0004-637X/832/2/165.

[281] C. Alcock and B. Paczynski. An evolution free test for non-zero cosmological constant. *Nature*, 281: 358–359, 1979. doi: 10.1038/281358a0.

[282] Dongwoo T. Chung, Tony Y. Li, Marco P. Viero, Sarah E. Church, and Risa H. Wechsler. On estimation of contamination from hydrogen cyanide in carbon monoxide line intensity mapping. 2017.